ROD-SHAPED PLASMONIC SENSORS

Synthesis and Single Particle Spectroscopy

Dissertation
zur Erlangung des Grades
"Doktor der Naturwissenschaften"
im Promotionsfach Chemie

am Fachbereich Chemie, Pharmazie und Geowissenschaften
der Johannes Gutenberg-Universität Mainz

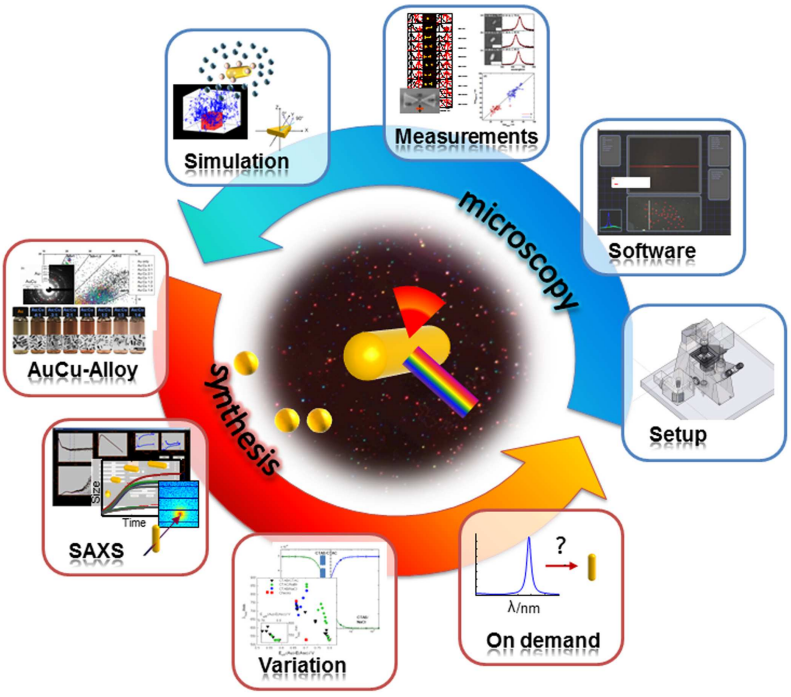

ANDREAS HENKEL, GEB. KURZ
geboren in Frankfurt am Main

Mainz, Dezember 2012

Dekan:	[Namen aus
1. Berichterstatter:	datenschutzrechtlichen Gründen
2. Berichterstatter:	entfernt]
Tag der mündlichen Prüfung:	13.12.2012

Andreas Henkel: *Rod-shaped Plasmonic Sensors* , Synthesis and Single Particle Spectroscopy, © Dezember 2012[1]

1 D 77

Imagination is more important than knowledge.
For knowledge is limited.

— Albert Einstein

Dedicated to
my beloved wife and my lovely daughters.

ABSTRACT

Plasmonic nanoparticles exhibit strong light scattering efficiency due to the oscillations of their conductive electrons (plasmon), which are excited by light. For rod-shaped nanoparticles, the resonance position is highly tunable by the aspect ratio (length/width) and the sensitivity to changes in the refractive index in the local environment depends on their diameter, hence, their volume. Therefore, rod-shaped nanoparticles are highly suitable as plasmonic sensors.

Within this thesis, I study the formation of gold nanorods and nanorods from a gold-copper alloy using a combination of small-angle X-ray scattering and optical extinction spectroscopy. The latter represents one of the first metal alloy nanoparticle synthesis protocols for producing rod-shaped single crystalline gold-copper ($Au_xCu_{(1-x)}$) alloyed nanoparticles. I find that both length and width independently follow an exponential growth behavior with different time-constants, which intrinsically leads to a switch between positive and negative aspect ratio growth during the course of the synthesis. In a parameter study, I find linear relations for the rate constants as a function of $[HAuCl_4]$/[CTAB] ratio and $[HAuCl_4]$/[seed] ratio. Furthermore, I find a correlation of final aspect ratio and ratio of rate constants for length and width growth rate for different $[AgNO_3]/[HAuCl_4]$ ratios. I identify ascorbic acid as the yield limiting species in the reaction by the use of spectroscopic monitoring and TEM. Finally, I present the use of plasmonic nanorods that absorb light at 1064 nm as contrast agents for photoacoustic imaging (BMBF project Polysound).

In the physics part, I present my automated dark-field microscope that is capable of collecting spectra in the range of 450 nm to 1750 nm. I show the characteristics of that setup for the spectra acquisition in the UV-VIS range and how I use this information to simulate measurements. I show the major noise sources of the measurements and ways to reduce the noise and how the combination of setup characteristics and simulations of sensitivity and sensing volume can be used to select appropriate gold rods for single unlabeled protein detection. Using my setup, I show how to estimate the size of gold nano-rods directly from the plasmon linewidth measured from optical single particle spectra. Then, I use this information to reduce the distribution (between particles) of the measured plasmonic sensitivity S by 30% by correcting for the systematic error introduced from the variation in particle size. I investigate the single particle scattering of bowtie structures — structures consisting of two (mostly) equilateral triangles pointing one tip at each other. I simulate the spectra of the structures considering the oblique illumination angle in my setup, which leads to additional plasmon modes in the spectra. The simulations agree well with the measurements form a qualitative point of view.

PUBLICATIONS

Some ideas and figures have appeared previously in the following publications:

ARTICLES IN PEER-REVIEWED JOURNALS

"*Size Variation Accounts for One Third of Interparticle Variation in Plasmonic Sensitivity of Gold Nanorods*"
Henkel, A.; Khalavka, Y.; Neiser, A.; Rosman, C.; Schmachtel, S.; Sönnichsen, C.
In preparation — manuscript finished

"*Single Unlabeled Protein Detection on Individual Plasmonic Nanoparticles*"
Ament, I.; Prasad, J.; **Henkel, A.**; Schmachtel, S.; Sönnichsen, C.
Nano Letters 2012, 12, 2, 1092
doi:10.1021/nl204496g

"*Growth Kinetic of a Rod-Shaped Metal Nanocrystal*"
Henkel, A.; Schubert, O.; Plech, A.; Sönnichsen, C.
J.Phys.Chem.C 2009, 113, 24, 10390
doi:10.1021/jp810979r

"*Tuning Plasmonic Properties by Alloying Copper into Gold Nanorods*"
Henkel, A.; Jakab, A.; Brunklaus, G.; Sönnichsen, C.
J.Phys.Chem.C 2009, 113, 6, 2200
doi:10.1021/jp810433e

CONFERENCE ARTICLES

"*Evaluation of Nanoparticles as Contrast Agent for Photoacoustic Imaging in Living Cells*"
Kohl, Y.; Thielecke, H.; Bost, W.; Lemor, R.; Stracke, F.; Kaiser, C.; Schroeter, M.; Kratz, K.; **Henkel, A.**; Sönnichsen, C.
Nanostructured Materials and Nanotechnology IV 2010
doi:10.1002/9780470944042.ch1

Publications not shown in this thesis:

ARTICLES IN PEER-REVIEWED JOURNALS

"*Multiplexed plasmon sensor for rapid label-free analyte detection*"
Rosman, C.; Prasad, J.; Neiser, A.; **Henkel, A.**; Sönnichsen, C.
Nano Lett., 13(7), 3243
doi:10.1021/nl401354f

"*A New Approach to Assess Gold Nanoparticle Uptake by Mammalian Cells: Combining Optical Dark-Field and Transmission Electron Microscopy*"
Rosman, C.; Pierrat, S.; **Henkel, A.**; Tarantola, M.; Schneider, D.; Sunnick, E. ; Janshoff, A.; Sönnichsen, C.
Small 2012
doi:10.1002/smll.201200853

"*Microfluidic continuous flow synthesis of rod-shaped gold and silver nanocrystals*"
Boleiniger, J.; **Kurz, A.**; Reuss, V.; Sönnichsen, C.
Physical Chemistry Chemical Physics 2006, 8, 3824
doi:10.1039/B604666E

CONFERENCE ARTICLES

"*En-Face differential absorption optical coherence tomography with gold nanorods as the contrast agent*"
Leitner, M.; **Henkel, A.**; Sönnichsen, C.; Rosa, C.C.; Podoleanu, A.G.
Proc. SPIE 7139
doi:10.1117/12.814624

CONTENTS

LIST OF FIGURES

LIST OF TABLES

1

INTRODUCTION

NANOSCIENCE seems to be a fairly young research field but acutally, it dates back at least about 150 years when Michael Faraday[1] synthesized gold nanoparticles and investigated their optical properties. In the following years, James C. Maxwell[2] developed the theory about electromagnetism and Lord Rayleigh,[3] Gustav Mie,[4] and Richard Gans[5] derived solutions for the optical properties of spherical and spheroidal nanoparticles using the Maxwell-equations. Today, numerical solutions for any kind of shape can calculated even with a standard personal computer available. In the beginning of the 20th century, Henry Siedentopf and Richard Zsigmondy developed the first dark-field optical microscope,[6] which allowed for the investigation of the scattering of nanoscopic objects — the predecessor of our dark-field microscopes today. And in the mid 20th century, electron microscopes became commercially available and 1959 Richard Feynman gave another stimulus to the nanoscience field with his famous speech „There's plenty of roomat the bottom".[7]

Today, nanoparticles and especially plasmonic nanoparticles can be more or less easily produced either in the top-down or the bottom-up approach. Plasmonic nanoparticles exhibit high light scattering efficiencies due to the collective oscillations of their conduction electrons (called plasmon), which can be excited with visible or infrared light for example in the case of the noble metals gold and silver. The most interesting property of plasmons is their sensitivity to changes in the local refractive index. One way for investigating plasmonic nanoparticles and their sensitivity is to use a dark-field microscope.

Just a decade ago, spectra of single particles were acquired by manually positioning the particle on a pin-hole and exposure times were in the range of tens of seconds. In the past 2 years, I have built a dark-field setup for the acquisition of single particle spectra with automated position and focus refinement. Utilizing automization and image correlation, I could improve speed and precision at the same time. My setup has been replicated 3 times by now and has become the state of the art measurment platform enabling the group to go for challenging projects. Using my setup, I established a method to directly estimate the absolute dimension of nanorods just from the single particle spectra, which will be an important tool for on-line optimal sensor selection during an experiment. Furthermore, during my thesis, I studied the synthesis of gold nanrods and could derive a practical guideline

I divided the thesis into three parts: theory, synthesis and microscopy. In the first part, I briefly explain a plasmon and how the resonance position and sensitivity of gold nanrods is influenced by their dimensions in simulations (Chapter 2).

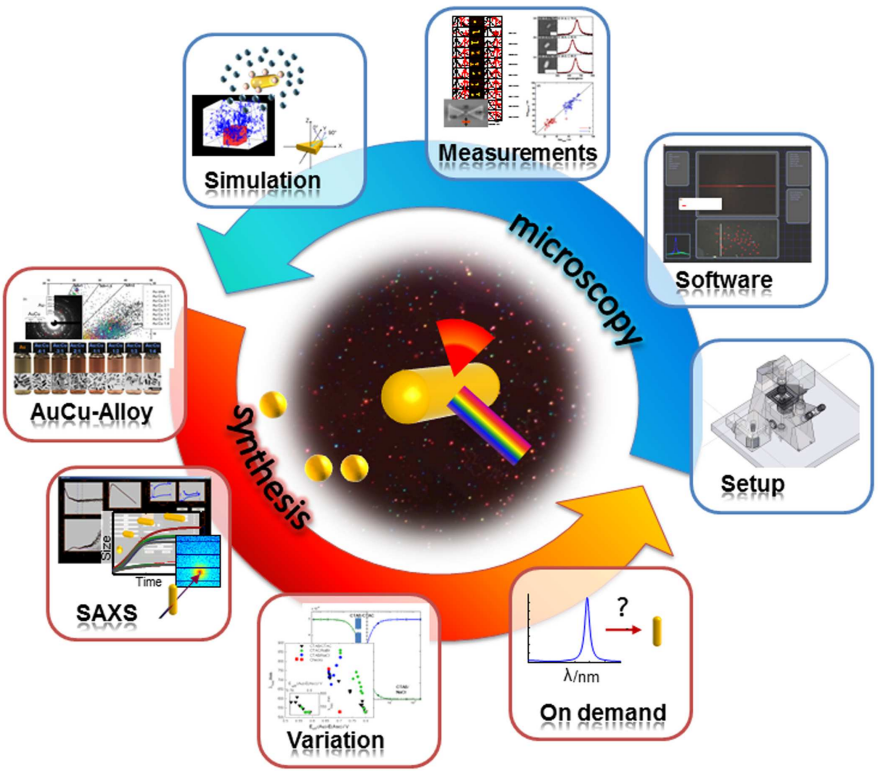

Figure 1.1: Scope of this thesis. Starting with studying the synthesis of Au and AuCu nanorods, I moved on to build a dark-field setup and performed measurments those particles. The two arrows show that one can't be without the other. When it comes to sensing experiments, you need to consider both the particles' sensitivity and their performance in a dark-field microscope to choose the optimal particle in every respect.

The second part consists of studies on the growth of gold and gold-copper nanorods. In Chapter 3, I elaborate how the plasmon resonance of rod-shaped nanoparticles can be changed by alloying gold an copper. In Chapter 4, the ratio of ascorbic acid to gold is verified as the yield determining aspect in the gold nanoparticle synthesis by monitoring spectroscopically the subsequent addition of ascorbic acid aliquots to a rod solution. Chapter 5, and Chapter 6 show kinetic studies on the growth of gold nanorods using small-angle x-ray scattering spectroscopic monitoring at the Swiss-Light Source (SLS) of the Paul-Scherre-Institute in Switzerland. In Chapter 5, I elaborate the switch in growth mode from 1D- to 3D-growth to follow naturally from the different decay in growth rate of the long and short axis growth. And in Chapter 6, I show results from a second session where I investigated the influence each entity in the growth solution on the kinetics of the gold nanorod growth. Chapter 7 presents the research project "nanopolymeric contrast agents for photoacoustic imaging" (short title: POLYSOUND) — a joint project of the Fraunhofer Institute for Biomedical Engineering (IBMT), the Centre for Biomaterial Development (GKSS, part of Helmholtz-Zentrum Geesthacht Centre for Materials and Coastal Research), and our group. For this project, I worked on the synthesis of particles with a resonance wavelength of 1064 nm. At last (Chapter 8), I summarize my experiences on the synthesis of

gold nanords in a flow chart as guideline to choosing the right composition for different resonance positions and sizes.

In the third part, I present my setup together with measurements and simulations for an optimal (rod-shaped) sensor selection. I characterized the important components of my setup and used those information to develop a simulation of the spectra acquistion identifying the major noise sources in the determination of the resonance position of a particle spectra (Chapter 9). In the following Chapter 10, utilizing BEM simulations and SEM image correlation, I present how the size distribution of gold nanorods accounts for about one third of the distribution broadening in sensitivity measurements and that one can easily determine the absolute dimensions of gold nanorods from single particle spectra only. Chapter 11 shows results on the single particle study of Bowtie structures produced by the group of Prof. Gießen. Finally, in Chapter 12 and Chapter 13, I demonstrate how simulations of the optical spectra of gold nanorods and the knowledge of the characteristics of a setup can be used to select an appropriate or optimal sensor and measure the single unlabeled protein adsorption on a gold nanorod.

Part I

THEORY

2

PLASMONS - A PRIMER

In 1856[1] at Hampton Court Palace in the Greater London borough of Richmond upon Thames[8] a well-known scientist noted:

> "A quick and ready mode of producing the ruby fluid, is to put a quart of the weak solution of gold [...] into a clean bottle, to add a little solution of phosphorus in ether, and then to shake it well for a few moments: a beautiful ruby or amethystine fluid is immediately produced, which will increase in depth of tint by a little time."[9]

Furthermore he observed:

> "A certain fluid in a bottle or glass, looked at from the front, i.e. the illuminated side by general daylight may appear hazy and amethystine, whilst in bright sunlight it will appear light brown and almost opake. From behind, the same fluid may appear of a pure blue in both lights, whilst from the side it may appear amethystine or ruby. These differences result from the mixture of reflected and transmitted lights, both derived from the particles, the former appearing in greatest abundance from the front or side, and the latter from behind."[9]

Although the striking colours of glass stained by gold was known since ancient times, yet Michael Faraday was one of the first, if not the first modern scientist who examined the synthesis and the optical and physical properties of colloidal gold particles systematically. Furthermore, at about the same time his studies about electricity, magnetism and light inspired a young physicist named James Clerk Maxwell to combine all known electric and magnetic effects into a simple comprehensive mathematical form now known as electromagnetism or electrodynamics.

Today, in the 21st century, there are many theoretical publications about optical properties of nanoparticles. Often the different ways to simulate the optical response of noble metal nanoparticles found in literature may appear confusing - especially to new people in the field. But in principle, most of the methods used are either analytical or numerical solutions of the Maxwell-equations. Within these solutions there are approaches that use electrostatics - also called quasi static approximation (QSA) - or electrodynamics like the discrete dipol approximation (DDA), the boundary element method (BEM) or the finite difference time domain method (FDTD) to describe the response of a metal interacting with a electromagnetic wave. Recently, antenna theory has been used to describe optical antennas, which nanoparticles in principles are. As usual for simulations, there is a trade-off between accuracy and computational expense, i.e. the electrostatic calculations

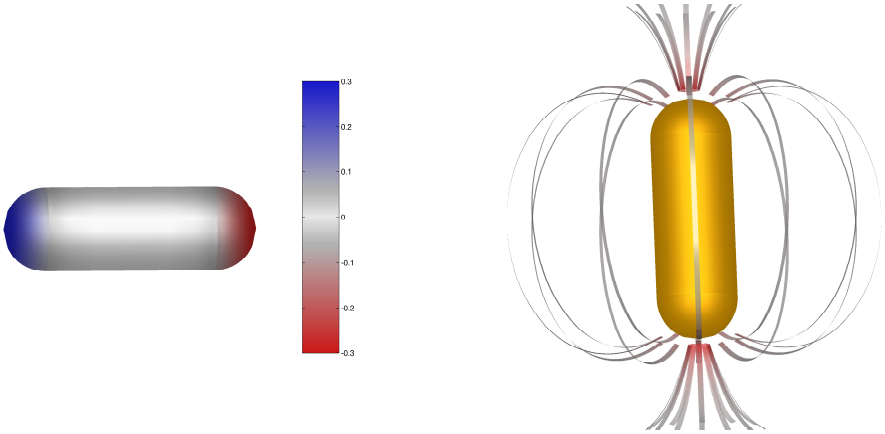

Figure 2.1: (a) Charge density of a rod excited at resonance wavelength of the dipole oscillation. The charges are separated to both tips. (b) The electric field outside the particle. The equipotentials follow the expected dipole field.

are very fast and the accuracy is fair or good and the numerical electrodynamic calculations can be rather slow because they depend on discretization of space, volume, surface, or time but the accuracy can be very high. For all electrostatic or electrodynamic calculations — no matter what exact method is used — the dielectric function must be known because this defines the interaction of a material with an incident electromagnetic field. In the case of gold, usually the tabulated values of Johnson and Christy are used.[10]

In the following section, I will briefly explain a plasmon and its calculation using the quasistatic approximation (QSA) and using the boundary element method (BEM). After that, I will focus on results from simulations of gold nanorods, which are partly used in Chapter 10 to obtain rod dimensions from scattering spectra only.

2.1 PLASMON

In general, a plasmon is a collective oscillation of the free electron gas - it is described as a quasiparticle just like phonons for instance. Especially for conductors like the noble metals gold and silver, the plasmon plays an important role in their optical properties. There are different types of plasmons: surface plasmons, volume plasmons, and particle or localized plasmons. As for this work, the relevant plasmon type is the particle plasmon since optical properties of plasmonic nanoparticles have to be discussed. In general, the plasmon depends on the material (i. e. the materials dielectric function) and the refractive index of the surrounding no matter whether it is surface, volume or particle plasmon.

In principle, when a plasmonic nanoparticle is exposed to an electromagnetic wave, the free charges inside the particle - for example a rod - follow the electromagnetic field of that incoming light. This leads to an oscillating charge separation and the particle forms a dipole oscillation when excited at its resonance frequency (the in-

duced fields are depicted in Figure 2.1). Lord Rayleigh proposed a simple model that can describe the response of plasmonic particles, which is based on an electrostatic approach. Assuming a constant electromagnetic phase over the whole particle, this model is valid for particles much smaller than the wavelength of light (usually < 40 nm). Since only electrostatics are involved in this approach, the following analytical solutions for the scattering and absorption cross-section (Equation 2.1) are obtained,[11]

$$C_{\text{sca}} = \frac{k^4}{6\pi\epsilon_0^2}|\alpha|^2 \tag{2.1}$$

$$C_{\text{abs}} = \frac{k}{\epsilon_0}\operatorname{Im}(\alpha), \tag{2.2}$$

and the computational expense is low. The polarizability α needed for the calculation of the cross-sections can be derived for a sphere or introducing a geometrical factor L_i more general for a spheroid[5] or ellipsoid.

$$\alpha_i = V\epsilon_0\frac{\epsilon_r - 1}{1 + L_i(\epsilon_r - 1)} \tag{2.3}$$

L_i denotes a geometrical factor that relates to one axis. Appropriate geometrical factors for the calculation of the polarizability of nanorods with different end cap structures have been obtained,[12] which describe the shape of synthesized nanorods better than a spheroid model.

The disadvantage of QSA is that this model doesn't take any retardation effects into account and therefore, it doesn't explain the changes in linewidth and resonance wavelength when the particle volume is increased. Using the boundary element method (BEM), a solution of the Green's function can be numerically estimated. Briefly, this numerical method discretizes the surface of a particle in surface elements and solves for the surface charges and currents that are induced by an incident electromagnetic wave at the interface of the particle to the outer dielectric environment. The whole method is described in great detail by the developers of this approach[13] and the developers of the MNPBEM Matlab toolbox[14].

2.2 DEPENDENCIES

In this section, I want to present some results of simulations done with BEM. First, I will discuss the general trends of resonance position and linewidth as function of aspect ratio and volume or diameter. Then, I will discuss the damping of the plasmon resonance and some interesting deviation of the expected behavior of the radiation damping. After that, I will focus on the sensitivities of different rods and how a rod should be selected for specific sensing applications. Finally, I briefly show the influence of temperature changes on the resonance position.

RESONANCE POSITION AND LINEWIDTH. Here, I show the change of the resonance energy as function of *AR* and the linewidth

as function of Volume as obtained by simulations using BEM. In these simulations I varied the diameters D from 15 nm to 50 nm in steps of 1 nm and aspect ratios $AR = L/D$ from 1.5 to 4 in steps of 0.1. The trends of E_{res} as function of AR is close to the linear relation observed in simulations using QSA [12] although the additional shift in resonance energy broadens the range of possible aspect ratios per resonance energy. The linewidth as function of volume is more complicated but for aspect ratios greater 2 a nearly linear relationship for constant AR can be observed. When both of these functions are combined into bijective functions of $AR(E_{\text{res}},\Gamma)$ and $D(E_{\text{res}},\Gamma)$, E_{res} and Γ of measured single particle spectra can be used to directly calculate AR and D without the need for an electron microscope as elaborated in Chapter 10.

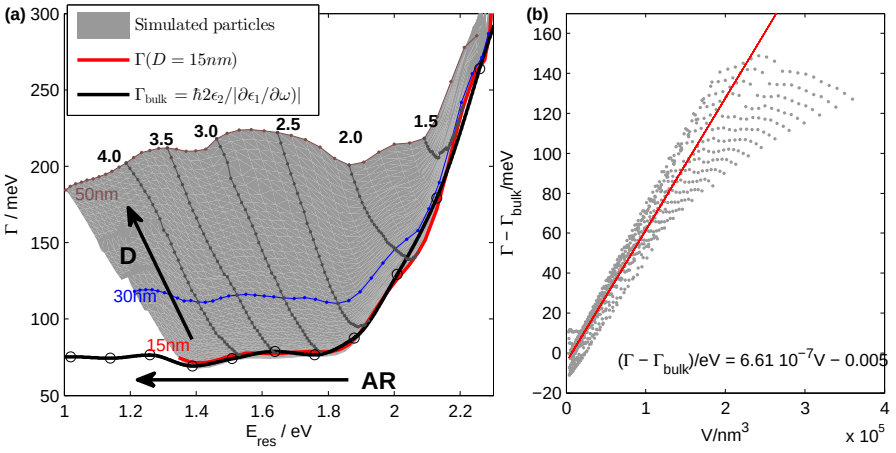

Figure 2.2: (a) Γ as function of E_{res}. For further details see text. (b) $\Gamma - \Gamma_{bulk}$ as function of particle volume. A mostly linear relationship with a slope of $6.61 \times 10^{-7}\,\text{eV}\,\text{nm}^{-1}$ is observed. Accordingly, the damping constant $\kappa = 6.61 \times 10^{-7}\,\text{eV}\,\text{nm}^{-3}/h = 1.60 \times 10^{-7}\,\text{fs}^{-1}\,\text{nm}^3$ is obtained.

In Figure 2.2a, Γ is shown as function of E_{res} for all simulated rods. Here, some general features of the linewidth, hence, the damping can be seen. First, there is a lower limit for the linewidth, which is purely determined by the dielectric function (black line). Furthermore, for energies smaller 1.8 eV this lower limit is approximately constant - here, the Drude-model of a free-electron gas could be applied. This lowest possible linewidth, hence, longest lifetime of the plasmon (Equation 2.4) arises from electron-impurity or electron-phonon scattering (note that QSA always show spectra with linewidths determined purely by the dielectric function because radiation damping is neglected). These electron scattering events can be seen as the nonradiative damping

$$\Gamma_{\text{nonrad}} \approx \hbar \frac{2\epsilon_2}{\left|\partial\epsilon_1/\partial\omega\right|}. \tag{2.4}$$

Furthermore, the increase of damping with increasing volume can be seen once more, which is due to the radiation damping Γ_{rad}.[15] The radiation damping is volume-dependent and described by

$$\Gamma_{rad} = \frac{\hbar\kappa V}{2}\,[16] \quad \text{or} \quad \Gamma_{rad} = \frac{h\kappa V}{\pi}.\,[17] \tag{2.5}$$

Now, I can evaluate the simulations with respect to the radiation damping. Therefore, I calculate Γ_{bulk} as function of energy and substract it from the simulated linewidths. The resulting linewidth is plotted as function of volume in Figure 2.2b. A linear fit has been performed and from the slope I obtain $\kappa = 1.60 \times 10^{-7}\,\mathrm{fs}^{-1}\,\mathrm{nm}^3$. This is in good agreement with the reported values in literature of $\kappa = 1.75 \times 10^{-7}\,\mathrm{fs}^{-1}\,\mathrm{nm}^3$,[16] $\kappa = 0.5 \times 10^{-7}\,\mathrm{fs}^{-1}\,\mathrm{nm}^3$,[17] and $\kappa = 4 \times 10^{-7}\,\mathrm{fs}^{-1}\,\mathrm{nm}^3$.[15] Interestingly, for high volumes and at high aspect ratios the linewidth deviates strongly from the otherwise linear relation. This starts approximately at particles with diameters larger 40 nm and aspect ratios larger 3.5. Unfortunately, these kind of particles are not accessible by our synthetic means. Either the diameter can be increased to 40 nm or even 50 nm but then the AR stays smaller 2.5 or the aspect ratio can be tuned large with a decrease of diameter. This prevents an experimental validation of this apparent effect.

SENSITIVITY AND SENSOR SELECTION. The sensitivity to the local environment is one of the most valuable features of plasmonic nanoparticles. The bulk sensitivity is defined as

$$S_\lambda = \frac{\Delta\lambda}{\Delta n}, \tag{2.6}$$

where $\Delta\lambda$ denotes the shift in resonance position and Δn the change in refractive index of the surrounding medium. Since this is highly important for any application, I simulated the spectra of gold nanorods in two refractive index of the surrounding medium of $n_1 = 1.33$ (water) and $n_2 = 1.40$ and the simulation was carried out for the same range as mentioned above, but in steps of 5 nm for D and steps of 0.25 for R. The resulting sensitivities are shown in Figure 2.3a. The sensitivity increases almost linearly with increasing aspect ratio and it increases for increasing volume, too.

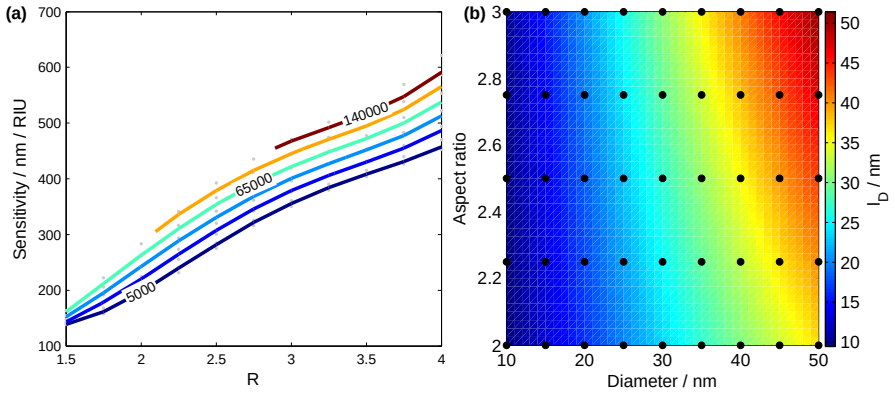

Figure 2.3: (a) Showing sensitivity as a function of aspect ratio AR. The lines are sensitivities at constant volume in nm^3. (b) Decay length (sensing distance) as function of AR and D.

At this point, considering Figure 2.3a, the selection of the biggest particle as the best sensor seems obvious. But this holds true only for measuring the exchange of the whole surrounding medium. The actual strength of the particles lies in their locality, providing the possi-

Table 2.1: Table containing the obtained coefficients for the function $l_D(AR, D)$ as denoted in Equation 2.10.

coefficients	l_D
a_{00}	-25.7
a_{01}	20.19
a_{02}	-3.717
a_{10}	2.306
a_{11}	-1.15
a_{12}	0.2283
a_{20}	-0.01408
a_{21}	0.005964
a_{30}	-2.113×10^{-5}

bility to investigate binding events to or at the particle. So, there is not only the sensitiviy but also the depth that a plasmon field penetrates into the surrounding medium. This decay length l_d defines the sensing volume V_s of a particle[18] — the volume within a particle shows a shift upon changes in the refractive index. The whole decay of sensitivity can also be approximated by an exponential function[18]

$$\Delta\lambda(r) = S\Delta n e^{-r/l_d}. \tag{2.7}$$

The sensing volume is needed whenever not the whole surrounding medium is exchanged but rather a change in the adsorption layer of a particle shall be investigated. If a molecule with volume V_p binds to the particle and therefore penetrates into the sensing volume the change in refractive index inside the sensing volume, hence, the shift per molecule can be estimated by

$$\Delta\lambda_m = S_\lambda \Delta n N \frac{V_p}{V_s} \quad (N = 1), \tag{2.8}$$

with N being the number of molecules and

$$V_s = (\pi(r + l_D)^2(L + 2l_D) - \frac{2}{3}\pi(r + l_D)^3) - (\pi r^2 L - \frac{2}{3}\pi r^3), \tag{2.9}$$

the sensing volume.

Compared to bulk sensitivity, for the selection of a best sensor for the detection of a certain molecule it gets more complicated, considering the parameters V_s and V_p, and information about of the particles V_s is needed. For this, I extended the simulations for the sensitivities of the rods to estimate V_s. In simulation, I was searching for a layer of thickness d with $n = 1.40$ on the particle surface that produces $1/e$ of the shift when the particle is completedly embedded in $n = 1.40$. Additionally, since the search for this shift resulted in some points of shifts as function of layer thickness, I used Equation 2.7 and obtained decay lengths for all the simulations (Figure 2.3b). This way, I

could obtain an estimate of the sensing distance and sensing volume for those rods.

l_D as function of AR and D can be interpolated by a surface fit using a 3^{rd} order polynomial,

$$l_D = \sum_{m+n\leq 3} a^D_{mn} AR^m D^n . \tag{2.10}$$

The coefficients are given in Table 2.1.

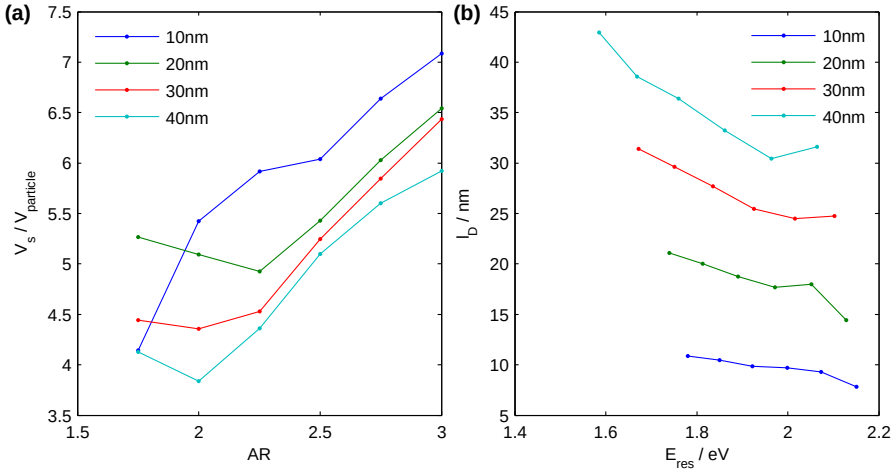

Figure 2.4: (a) V_s/V_{particle} as function of aspect ratio AR. (b) Decay length (sensing distance) as function of E_{res}.

Adding to the data in Figure 2.3b, I plotted the decay length l_D as function E_{res} for 4 different diameters in (Figure 2.4b). It can be seen that the decay length or sensing distance scales with the particles diameter and the aspect ratio has only little influence. Using l_D, I also calculated the sensing volume for all simulations and investigate V_s/V_{particle} as function of AR (Figure 2.4a). Here, the trend is slightly different. The ratio V_s/V_{particle} does not change significantly as function of the particle diameter whereas it increases slightly with the aspect ratio. Overall the change is small and as a rule of thumb the $V_s \approx 5.5 V_{\text{particle}}$.

For experiments, Equation 2.9 can be used to estimate the number of molecules within the sensing volume, too. Note that this approach considers a constant sensitivity throughout the sensing volume. Actually, the sensitivity will be the highest at the surface of a particle and then decay until it reaches zero at a certain distance.[18] But, as shown in Chapter 12 the approximation of a constant sensitivity can explain measurements of single protein adsorption reasonably well.

For predictions on a certain experiment, one has to consider the noise of the measurements, too. Because the best sensor in terms of sensitivity and size may provide the largest shift per molecule but an insufficient signal to be measured at a certain setup. This will be dicussed further in Chapter 13 using the information about my setup in Chapter 9.

Part II

CHEMISTRY

3

TUNING PLASMONIC PROPERTIES BY ALLOYING COPPER INTO GOLD NANORODS

3.1 INTRODUCTION

TUNING the plasmon properties (resonance frequency and linewidth) for the desired application is achieved through the nanoparticles' shape or material composition. Rod-shaped particles are the most useful plasmonic structures as their polarizability is strongly enhanced compared with more spherical shapes and their resonance frequency is dependent on the aspect ratio.[19,20] The material for plasmonic nanorods is almost exclusively gold because of its chemical stability and the availability of robust protocols for their high yield synthesis. Nanorods with a silver coating[21] or a silver-gold alloy[22] have also been reported and shown improved plasmonic properties.[23] Gold-copper particles have only been synthesized without shape control.[24,25,26] In general, synthesizing alloyed nanocrystals is complicated by the tendency for self-purification.[27,28]

Here, I report a protocol for producing rod-shaped single crystalline gold-copper ($Au_xCu_{(1-x)}$) alloyed nanoparticles. I characterize them with various direct and indirect optical and electron microscopy techniques in order to verify the presence of copper in the particles. Pure spherical copper particles show no plasmon resonance because of the degeneracy with interband excitations of d-band electrons - AuCu nanorods are therefore the only plasmonic particles with high copper content. Changing the copper content allows me to vary the plasmon resonance frequency and linewidth. Electron diffraction and optical single particle plasmon-linewidth observations suggest an ordered AuCu lattice in the particles (at least after mild tempering) leading to reduced plasmon damping at specific stoichiometric copper contents.

3.2 RESULTS AND DISCUSSION

I need to establish first that copper ions present in the growth solution are indeed incorporated into the particles during growth. The most direct evidence for copper in or around the particles comes from EDS analysis and solid state NMR - both methods show a clear copper signal coming from the samples of nanorods grown in the presence of copper (Figure 3.1). Indirect evidence comes from optical spectra compared to TEM size analysis: the presence of copper changes the plasmon resonance position in a way incompatible with the shape variations observed by TEM (Figure 3.2). Explaining the trends in the optical spectra requires a dielectric function modified by the presence of copper (Figure 3.3). My collegue Arpad J. investigated the optical properties of the particles more carefully on a single particle level and

found evidence for reduced plasmon damping at specific Au:Cu ratios in the growth solution. Electron diffraction patterns of such samples show the emergence of a regular Au:Cu lattice after mild tempering, which may be responsible for the reduced plasmon damping (Figure 3.7).

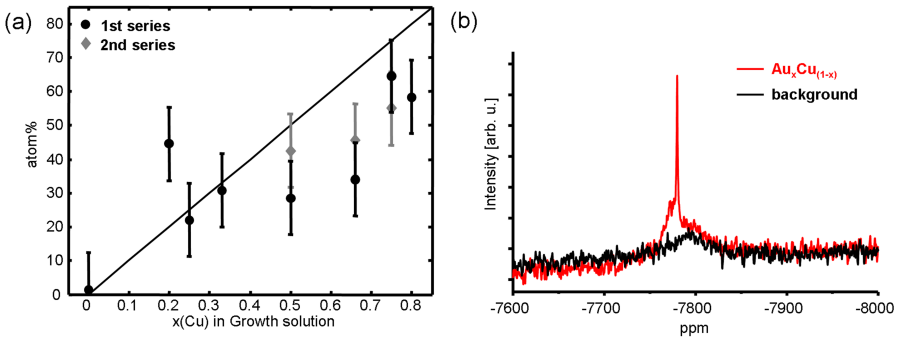

Figure 3.1: (a) Atomic composition of $Au_xCu_{(1-x)}$ particles with different copper amounts (x(Cu)) in the growth solution as determined by EDS on groups of particles. The values show a trend towards higher Cu content in particles produced from growth solutions containing more Cu. The measurement error (indicated by the error bars) is estimated by repeated experiments to be about 10%. A background value of 5% has been subtracted from the Cu content. Black dots: series shown in Figure 3.3. Grey diamonds: different series. (b) Static ^{63}Cu spectra of a $Au_xCu_{(1-x)}$ sample compared to the background. A sharp singularity at −7780 ppm and a broad featureless hump is observed, which clearly reveals the presence of Cu within the nanoparticles.

To quantify the amount of copper in the particles, I performed EDS (energy dispersive X-ray spectroscopy) analysis of the particles. Unfortunately, some Cu signals can be found in all EDS measurements (even when using Ni grids), because Cu is present in parts of the electron microscope. To account for this background Cu signal, I subtract a value of 5% from the measured Cu content - a value typically found on empty grids and on areas not containing particles. The mean values averaged over the course of at least 3 measurements show a trend towards higher Cu content in particles produced from growth solutions with higher Cu contents (Figure 3.1a). Generally, the copper content in the particles seems to be lower than its content in the growth solution. Interestingly, there is a good agreement with the expected amount at the Au:Cu ratios 1 : 3 and 3 : 1, which are known AuCu alloys with defined crystal structure.[29] However, the amount of copper I find in different parts of one TEM grid varies strongly (see error-bars). Therefore, the presence of Cu was verified by solid-state ^{63}Cu-NMR for a sample with a low amount of Cu in the growth solution. The NMR clearly showed a Cu signal at −7780 ppm above background, confirming the presence of copper in the particles (Figure 3.1b).

The plasmon resonance wavelength is a function of material composition, aspect ratio and end cap geometry.[30] I therefore carefully analyzed the particle sizes of samples with Au:Cu ratios of 4 : 1 to 1 : 4 by measuring the length and width of one thousand particles per sample on TEM images (Figure 3.2). The mean aspect ratio is about 3 except for very high copper contents (Au:Cu 1 : 3 or 1 : 4), where the aspect

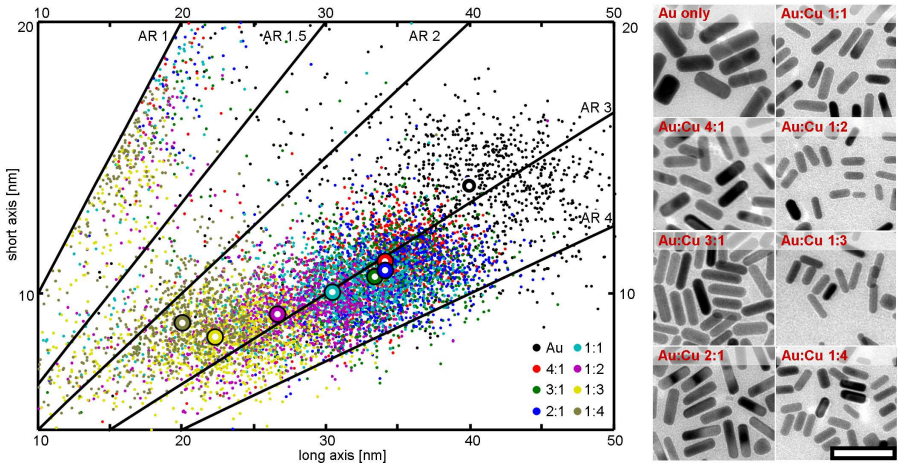

Figure 3.2: Size distribution and exemplary TEM images of copper-gold-rods synthesized with different metal salt ratios in the growth solution. The thick circles mark the mean of the distribution and the lines indicate different aspect ratios. The aspect ratio (AR) of the rods stays close to an AR of 3 for all different compositions (compare TEM images), while the length and the width are decreasing with an increasing Au:Cu ratio. The differences in sizes can be clearly seen when the images of Au only and Au:Cu 1:4 are compared. Scalebar 60 nm.

ratio decreases to about 2. I find a small fraction (<10%) of "spherical" particles with aspect ratios smaller than 1.5, which I excluded from the calculations of the means.

The overall length and width of the particles (i.e. the volume) decreases continuously with increasing copper content, which points towards a less than stochiometric inclusion of copper into the particles. The polydispersity of the long axis is approximately 5% lower for the AuCu samples (15% instead of 20%) compared to a pure Au sample, while the polydispersity of the short axis stays the same. The curvature of the end caps increases with an increasing Cu amount. Increasing the content of Cu in the growth solution leads to a strong red shift of the maximum value in the extinction spectra (about 100 nm with respect to the pure gold sample) until a ratio of 1 : 1 is reached. Further increasing the amount of Cu shifts the spectra back to the blue (Figure 3.3). When I increase the copper content, the gold concentration is reduced correspondingly to keep the total metal ion concentration fixed. To exclude the possibility that the reduction of Au concentration itself is causing the observed spectral changes, we repeated the experiment leaving out the copper (adjusting the amount of ascorbic acid and $AgNO_3$ to the now reduced amount of metal ions). The extinction spectra for these samples show a constant resonance wavelength down to gold concentrations comparable to the Au:Cu 1 : 1 synthesis. At lower gold concentrations, the resonance wavelength shifts to the blue and a pronounced decrease of the total extinction is observable. Additionally, I checked the influence of the small amount of $AgNO_3$ present in the growth solution. I found opposite trends for particles with and without copper ions present in the growth solution: for pure gold rods, the plasmon resonance shifts to the red with increasing sil-

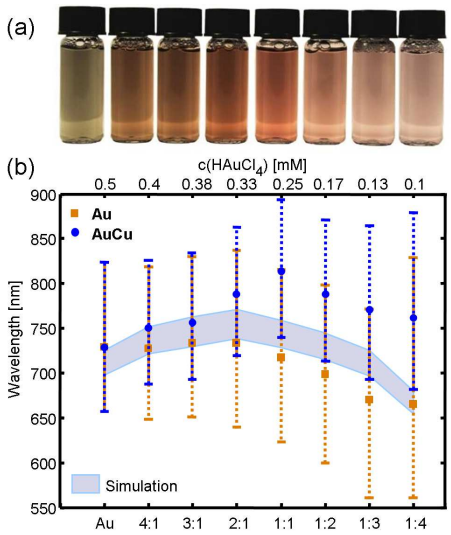

Figure 3.3: (a) Real color images of the gold copper samples (the order is equal to the x-axis labels on the bottom). (b) Plasmon resonance wavelengths for ($Au_xCu_{(1-x)}$)) samples with increasing Cu content. Increasing the Cu amount leads to a red shift of the longitudinal plasmon resonance with the strongest shift at a gold-to-copper ratio of 1:1 (blue dots, error bars show ensemble linewidth). Further increasing the Cu content decreases the red shift. Both the alloy composition and particle size are shifting the plasmon resonance. Pure Au samples (orange squares) with different Au concentrations show a constant resonance wavelength or a blue shift compared to the original synthesis (for c($HAuCl_4$) smaller 0.25 mM) under the same synthesis conditions. The shaded area shows the plasmon resonance range expected from simulations for pure gold nanorods with different end cap geometry using the size distributions of the ($Au_xCu_{(1-x)}$) samples as obtained by TEM analysis. The copper-gold nanorods are clearly outside this range.

ver concentration, whereas in the presence of copper ions, the resonance shifts to the blue (Figure 3.4).

The general trend of the influence of $AgNO_3$ on the spectral position for the pure Au and Au:Cu 1:1 case is therefore just the opposite. Interestingly, the slope of the spectral shift as a function of silver concentration is exactly half as high (and of opposite sign) for the Au:Cu particles compared to the pure Au particles. It has been proposed that $AgNO_3$ adsorbs to different crystal facets with different affinity and in this way contributes to the anisotropic growth of Au nanorods. It is unclear how this mechanism would lead to a completely opposite behavior for $Au_xCu_{(1-x)}$ particles.

The optical response of plasmonic nanoparticles can be simulated using the size parameters obtained from TEM (see above) and bulk dielectric functions with the Mie-Gans theory. Unfortunately, there are several conflicting dielectric functions reported for AuCu alloys, often only up to 800 nm (Figure 3.5). I therefore simulated spectra with the dielectric function of pure gold, which was successfully used to predict the spectral response of gold nanoparticles in earlier studies.[32] Here, we used both spherical and flat end caps to obtain a prediction band for the resonance wavelengths of pure gold particles (Figure 3.3). I find a significant mismatch of the resonance wavelengths of AuCu

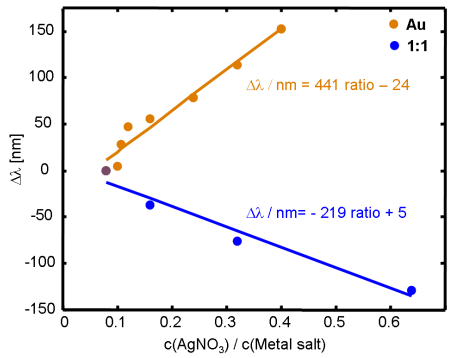

Figure 3.4: Shift of the resonance wavelength as a function of $AgNO_3$ to metal salt ratio. Syntheses with increasing $AgNO_3$ to metal salt ratio show a red shift of the resonance wavelength for Au nanorods (orange dots) while a blue shift is observed in the case of Au_1Cu_1 nanorods (blue dots). The influence of $AgNO_3$ on the resonance wavelength is approximately linear in both cases.

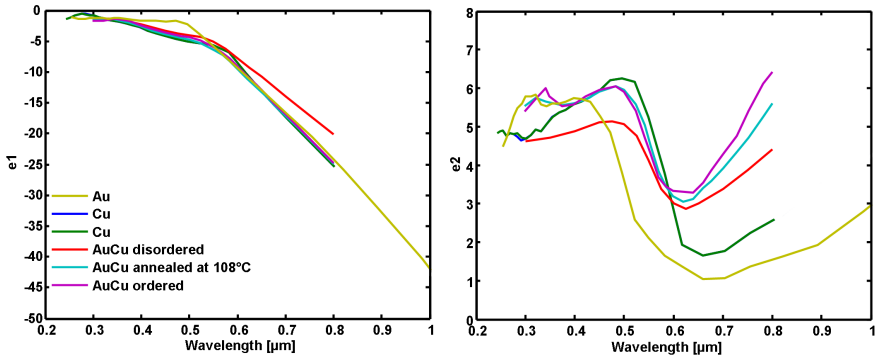

Figure 3.5: Dielectric functions reported for different materials and different modifications. Clearly, the dielectric function of AuCu is strongly affected by the crystallinity. The spread in reported values is too high to get reliable results from electrodynamic calculations of the plasmon resonance of gold-copper particles. The values of the dielectric functions were published by either Johnson [10] or Köster. [31]

particles compared to the predicted wavelengths for Au nanorods, especially for Au:Cu ratios above 2 : 1. This mismatch and the difference with the results from syntheses without copper indicate a difference in the dielectric function of the produced particles to pure gold particles, hence the presence of Cu in the particles.

We looked for evidence of an ordered AuCu lattice using electron diffraction. At first, the sample we studied showed the diffraction pattern expected for cubic (fcc) gold with a lattice constant of 0.403 nm (Figure 3.7 a). However, after some moderate tempering (heating to 200 °C, leaving it constant for 20 min, then raising the temperature in 50 °C steps for 20 min until 400 °C), we observed clear evidence for an ordered AuCu phase. While heated, the shape of the particle was mainly preserved. First, additional diffraction spots (lattice constant 0.37 nm) were visible at 350 °C (Figure 3.6). At 400 °C, more spots appeared, which were distinct from those belonging to the 0.403 nm fcc Au lattice. Those new spots belong to an ordered AuCu phase with a lattice constant of 0.38 nm. That means that either parts of the parti-

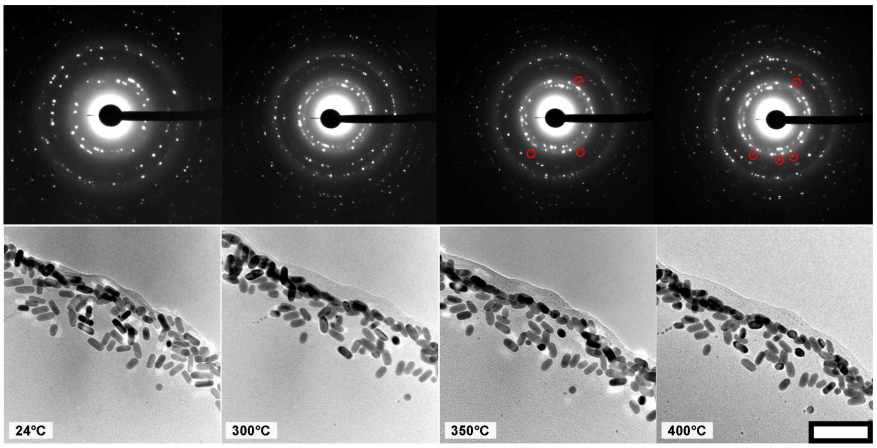

Figure 3.6: Au_1Cu_1 particles show a transition from an Au lattice to an AuCu lattice when they are heated by in situ TEM. The red circles in the electron diffraction patterns (top) emphasize some low index reflections (210) which start to appear at 350 °C. At 400 °C, an AuCu phase c an be found. The images (bottom) show that the shape of the particles is mostly preserved (scalebar 100 nm).

cles or some of the particles that contained the right ratio of Au:Cu form an ordered AuCu phase.

In order to search for an influence of the varying material composition of the AuCu particles on plasmon damping, my collegue Arpad J. investigated the samples with single particle dark-field spectroscopy. The spectral linewidth (FWHM) determined from single particles (homogeneous linewidth) is directly related to the plasmon damping. For single crystalline nanorods of the sizes found in this study, the main plasmon damping mechanism is through electronic excitations within the conduction band caused by electron-electron collisions (intraband damping).[33] Interband excitations (from the d-band to the conduction band) require a threshold-energy (about 2 eV for gold and copper). It is therefore useful to plot the plasmon linewidth against the resonance energy when comparing samples (Figure 3.7b). Since many processes (imperfections in the crystal, the surface quality, aggregations, strongly bound chemical surface contaminations) lead to additional damping in some particles, I expect a range of linewidths for any given resonance energy. The lower bound of this range - represented by the 90/10 median - is characteristic for the material. We indicate those lower bounds with lines in Figure 3.7b and observe a general increase of damping for higher resonance energies (as expected from increased interband damping). There is a significant difference between the samples. At Au:Cu ratios of 4 : 1, 2 : 1, 1 : 2 and 1 : 4 (referring to the concentrations of the precursors in the growth solution), the linewidth is lower than the linewidth at the ratios of 3 : 1, 1 : 1 and 1 : 3 (Figure 3.7c). For another series of samples, we checked the precise elemental composition with EDS and found a local minimum in linewidth at x(Au) = 0.54 (Figure 3.7c).

Previous experimental[34] and theoretical[35] reports found high DC electrical conductivity for Au:Cu ratios of 1 : 1 (x(Au) = 0.5) and 1 : 3 (x(Au) = 0.25). The intraband plasmon damping is - within the Drude

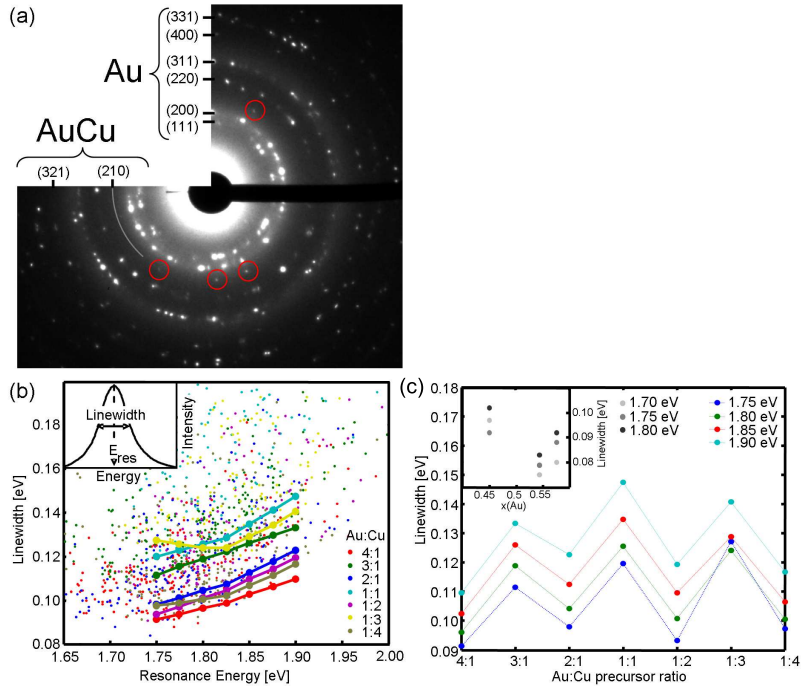

Figure 3.7: (a) Selected area electron diffraction (SAED) pattern of Au_1Cu_1 particles heated by in situ TEM. At 400 °C, an AuCu phase can be found indicating a phase transition. The red circles in the SAED emphasize some low index reflections (210), which start to appear at 350 °C. The shape of the particles is mostly preserved (Figure 3.6). (b) Single particle linewidth (FWHM) versus resonance energy (Eres) determined from spectra in a dark-field microscope (inset) for eight samples with Au:Cu ratios in the growth solution of 4:1, 3:1, 2:1, 1:1, 1:2, 1:3, 1:4 as indicated by the colors. The continuous lines correspond to the minimum linewidth trend lines of the respective sample (90% lines) due to the intrinsic damping of the material. I observe a general increase of linewidth with increasing resonance energy due to stronger interband damping from d-band electrons at higher energies. (c) Comparing the minimum single particle plasmon linewidth at given resonance energies for samples made from different Au:Cu ratios show minima at certain ratios. The inset shows the minimum linewidth as a function of elemental composition for 3 samples. I observe a minimum at $x(Au) = 0.54$.

theory - proportional to the DC conductivity. Even though a direct comparison of DC conductivity and damping at optical frequency is not possible, these previous DC reports on copper-gold alloys make the optical results plausible, if we assume that the strong light fields in the dark-field microscope induced the formation of an ordered stoichiometric gold-copper alloy. The evidence we gathered about the rod-shaped particles formed in a gold-copper mixture conclusively shows the presence of a gold-copper alloy. The particles have unique spectral characteristics, shapes, crystal structures, EDS spectra and plasmon damping strength. The copper content allows me to control the two important plasmon properties: resonance position and linewidth. We find reduced intraband damping at specific copper contents. The successful formation of alloyed nanocrystals from solution with co-precipitation while preserving the shape control will be useful for other metal particle synthesis.

3.3 EXPERIMENTAL SECTION

We prepare $Au_xCu_{(1-x)}$ nanoparticles using a seeded growth technique modified from the procedure for gold nanorods published by Nikoobakht.[36] Preformed gold seeds are added to a growth solution containing gold and copper ions in various ratios together with surfactants (cetyltrimethylammoniumbromide, CTAB) and reducing agents (ascorbic acid, AA). We characterize the resulting monocrystalline rod-shaped nanoparticles using transmission electron microscopy (TEM), energydispersive X-ray spectroscopy (EDS), solid state nuclear magnetic resonance (NMR), optical extinction spectroscopy (UV-Vis), and darkfield single particle spectroscopy (DF-SPS). All chemicals are purchased from Sigma Aldrich and used without purification. Deionized water (>18 kΩ) is obtained from a Millipore system (Milli Q).

SEED SYNTHESIS. 50 µL of 0.1 M tetrachloroauricacid ($HAuCl_4$) is added to 5.0 mL of water and mixed with 5.0 mL of 0.2 M CTAB in water solution. During vigorous shaking, 5.0 mL of ice-cold 0.010 M sodiumborohydride ($NaBH_4$) are added resulting in the formation of a brownish yellow or yellow solution. After 1 h at 35 °C, the solution can be used. Afterwards, the solution is kept at 30 °C and used within one week.

SYNTHESIS OF $AU_XCU_{(1-X)}$ NANOPARTICLES. Keeping the overall metal salt concentration constant at 5×10^{-4} M, we vary the molar ratio between $HAuCl_4$ and copper(II) chloride ($CuCl_2$) between 4 : 1 to 1 : 4. The metal salts are dissolved in 5.0 mL of water and mixed with 5.0 mL of 0.2 M CTAB solution. We add 10 µL of 0.04 M silvernitrate ($AgNO_3$) as in the pure gold rod recipe, which helps in the formation of rod-shaped particles. Then, we add just enough ascorbic acid (AA) to reduce all Au^{3+} and Cu^{2+} ions to their mono-valent ions

$$c_{AA} = c_{AA,x_{Au}} + c_{AA,1/2x_{Cu}}$$

where x is the mole fraction of the element and c_{AA}, the standard AA concentration for gold nanorod synthesis, $c_{AA,} = 0.0788$ M). The reducing agent changes the growth solution from dark yellow to colorless. After the addition of 12 µL of seeds, the solution gradually changes color within 10 min to 20 min, indicating the growth of nanoparticles.

CHARACTERIZATION. Particle suspensions were characterized within one week after synthesis, typically on the same or the next day. For clarity, we named the samples according to the ratio of gold and copper ions present in the growth solution, which does not necessarily match the atomic composition of the final particles.

UV-VIS SPECTROSCOPY. Extinction spectra were measured using an OceanOptics USB2000 Spectrometer equipped with an OceanOptics HL-2000-FHSA halogen lamp with a resolution of 1 nm.

NMR SPECTROSCOPY. Static ^{63}Cu NMR Hahn-Echo spectra were acquired at 184.53 MHz using a Bruker Avance 700 spectrometer and an interpulse delay of 20 µs. 12 µL of an Au_4Cu_1 nanoparticle solution were transferred into a commercial BRUKER 4 mm HR-MAS ZrO_2 rotor, and measured at room temperature. 2048000 scans were accumulated using 200 ms relaxation delay. In addition, a background control spectrum was recorded (empty probe). All spectra were referenced with respect to solid copper(I) bromide at ~ 381 ppm.

TEM. TEM analysis was performed at the Electron Microscopy Center (EMZM) at the University of Mainz, Germany, on a Philips CM12 using an operating voltage of 120 kV. EDS measurements were performed on a FEI Tecnai 30 (300 kV). Typically, EDS data was acquired in imaging mode on a group of particles using an integration time of 90 s. TEM samples were prepared from about 1 ml of nanoparticle solution, centrifuged twice for 10 min at 9870 g (10 000 rpm). The supernatant solution was first replaced by 1 ml and the second time by 300 µL of fresh water. A drop (5 µL) of this concentrated solution was deposited on a 200 mesh formvar-coated copper grid and dried in air at 30 °C. For EDS analysis, Ni-Grids were used to reduce copper background. Statistical size analysis was performed on about 1000 particles for each sample. The particle sizes were measured by hand and - when possible - with the automatic sizing tool of the ImagePro software package. We cross-checked the reliability of the automatic count by hand for every image series and obtained the same sizes.

DARK-FIELD SPECTROSCOPY. Single particle scattering spectra were measured in a self-made high-throughput dark-field microscope setup. We prepared samples by spreading a drop of a diluted particle suspension on a clean glass slide, adding salt to immobilize the particles as well as (after drying) a drop of immersion oil. A computer-controlled scanning piezostage (Physik Instruments) moved the sample in steps in the x direction. On each x position, a spectrum was taken from a narrow strip in the middle of the field of view by an imaging spectrometer (SP2300i, Acton Research) coupled with a cooled CCD camera (Pixis 400 Princeton Instruments). A strip has the dimensions of step-size (=spectrometer entrance slit width = 1 µm) times the y-axis field of view of the microscope (150 µm using a 40x objective (Carl-Zeiss NP-Neofluar)). After scanning the stage in ± 100 µm in the x-direction, we have full spectroscopic information for every point on a 200 µm x 150 µm area of the sample. Particle spectra are identified by setting a threshold on integrated intensity (a typical measurement contains over 200 particles). The raw particle spectra are background corrected and normalized to the spectrum of the illumination light and the spectral characteristics of the detection system. For each spectrum showing a pronounced peak, we determine the maximum and the full width at one-half maximum intensity (FWHM).

4

ASCORBIC ACID DETERMINES YIELD IN SEED-MEDIATED GOLD ROD SYNTHESIS

THIS chapter contains the work concerning the reactant ascorbic acid in the rod synthesis, which is intended to be published either as a communication or as part of a comprehensive article about the growth mechanism of gold nanorods.

4.1 INTRODUCTION

AFTER over one decade of research, the seed-mediated wet-chemical synthesis of gold nanorods remains not fully understood. Many studies have been performed out using spectroscopic monitoring, TEM, SAXS, EXAFS or simply parametric variation and observing the outcome. Although it is well known by now, how to grow rods with certain optical properties — even to grow different shapes of gold particles — it is not completely understood why they grow a specific way. The role of all chemicals in the synthesis — CTAB, silver, ascorbic acid, gold — have been adressed in literature already but very little is known about the reducing agent ascorbic acid. It is well-known that a little excess of ascorbic acid compared to Au^{3+} is needed in the gold rod synthesis to grow rods at all but only a few systematic studies have been done. Since the ascorbic acid is the reducing agent it should be connected with the yield of particles in some way. This study deals with ascorbic acid in seed-mediated rod growth. Ascorbic acid is identified as the yield limiting species in the reaction by the use of spectroscopic monitoring and TEM of a rod solution.

4.2 RESULTS AND DISCUSSION

In literature, there are some hints about the role of ascorbic acid in the synthesis. Using ICP-AES, Orendorff et al.[37] determined a yield of 15% of Au_0 for an excess of ascorbic acid of 10%. Furthermore, it has been published that the supernatant of a particle solution after centrifugation is colorless, that is to say no Au^{3+} is left in solution and heating the supernatant leads to particle growth, which indicates the presence of unreacted Au^{+} and dehydroascorbic acid.

Considering the 1.1-fold excess of ascorbic acid with respect to Au^{3+} used in the synthesis these facts can be combined to the following:

A. All initial Au^{3+} is reduced to Au^{+} and 10% of ascorbic acid is left.

B. The excess of ascorbic acid is enough to reduce 20% of the Au^{+} since it's a 2-electron donor.

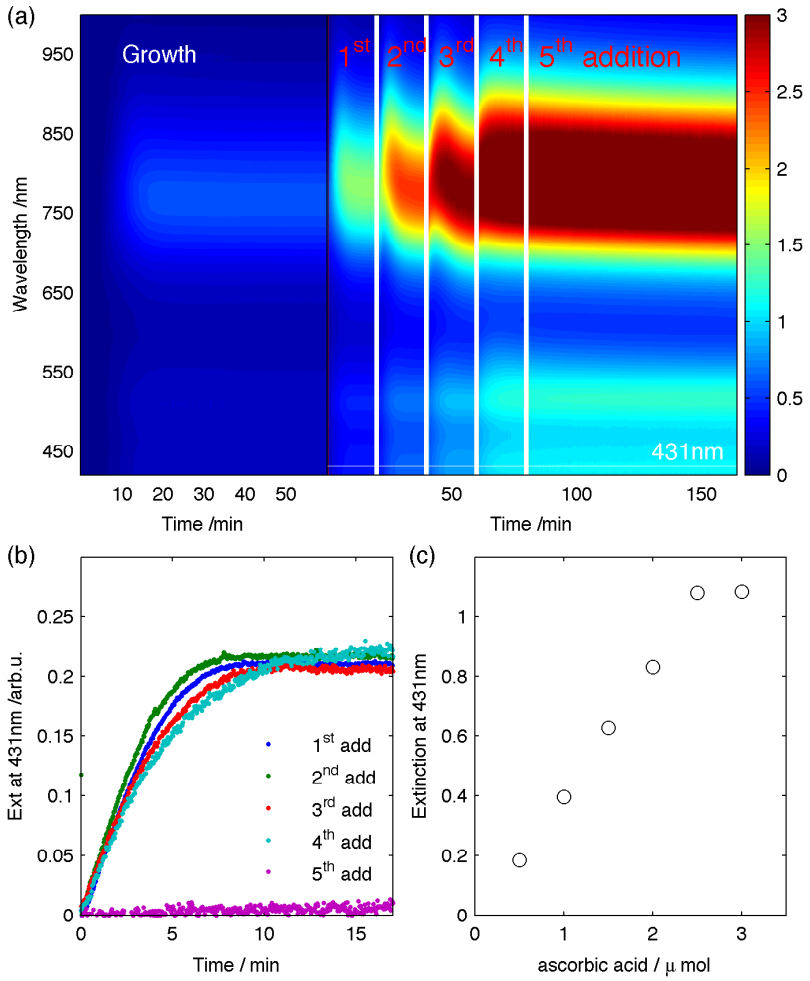

Figure 4.1: a) Spectral evolution of the particle solution upon growth and further ascorbic acid additions. The extinction is color-coded. White lines indicate the times of addition and the dashed line indicates the wavelength used for investigating the intensity. b) Extinction at 431 nm as a function of time. Times were shifted by the time of addition to $t = 0\,\mathrm{s}$ and the extinction shifted by the extinction at the time of addition. Inset shows the first minutes of which the first 1.5 min were approximated by a line to obtain the initial rate. c) Initial rates as number of addition. We observe only little difference in the initial rates - v_i $(0.042 \pm 0.005)\,\mathrm{min}^{-1}$

$$\mathrm{AuBr_4^- + H_2Asc} \rightleftharpoons \mathrm{AuBr_2^- + Asc + 2H^+ + 2Br^-} \quad (4.1)$$

$$\mathrm{2AuBr_2^- + H_2Asc} \overset{Au-surface}{\rightleftharpoons} \mathrm{2Au^0 + Asc + 2H^+ + 4Br^-} \quad (4.2)$$

We can sum up these facts to a hypothesis: The excess of ascorbic acid determines the amount of gold that ends up in the particles, hence an excess of 50% compared to the gold concentration is necessary to reduce all gold-ions in solution.

To prove this hypothesis, I grew nanorods in a standard synthesis as described in the experimental section. The solution contained 5 µmol Au^{3+} and 5.5 µmol ascorbic acid. According to the theoretic yield of 20%, we should be able to add another 4 times 0.5 µmol of ascorbic acid until all the Au^+ is consumed. On the fifth addition no more Au^+

should be in solution and the particles shouldn't grow anymore. As a measure of Au^+ reduction, I used the interband region - in this case extinction at 431 nm - to monitor the amount of Au_0, which resembles the particle volume if the particle number stays constant.

The starting rods were allowed to grow for 60 min until no spectral changes were visible anymore. Then aliquots of 0.5 µmol ascorbic acid were injected stepwise and to record the time of addition the shutter of the light source was closed for a few seconds. Figure 4.1a

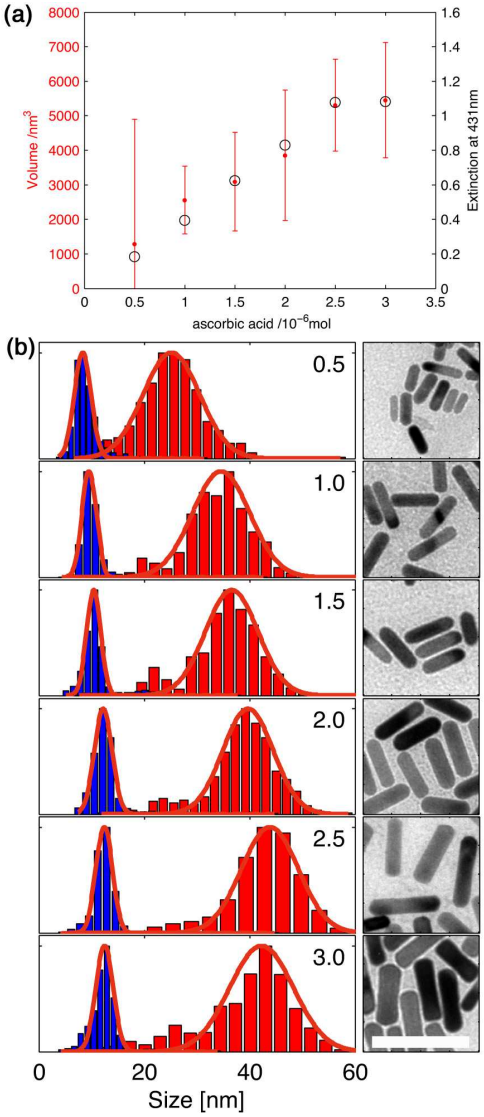

Figure 4.2: a) Particle volume and extinction at 431 nm as function of ascorbic acid added. The behavior is the same for both indicating a volume increase without additional nucleation. b) Length (red bars) and width (blue bars) distribution as obtained by TEM analysis. For each sample an image Is shown. Scalebar 50 nm.

shows the whole course of the experiment. About 30 min after injecting the seeds no changes were visible anymore in the spectra. In the following, aliquots of 0.5 µmol ascorbic acid were injected about every 20 min. The extinction in the maximum of the longitudinal plasmon peak soon reached saturation level of the spectrometer whereas the extinction at 431 nm reaches a value of 1 in the end, which is just within

the Lambert-Beer limit. On every addition of ascorbic acid the extinction at 431 nm increased by ≈ 0.21 (Figure 4.1b) indicating a similar increase of Au_0 in the solution for each addition. The initial rate upon each addition varies only about 10% (Figure 4.1c) showing that the reaction keeps the same for all additions. As predicted, the fifth addition of ascorbic acid produced no change.

To verify the findings, I analyzed each of the states by TEM. Images and size distributions are shown in Figure 4.2b. The trend is similar to the spectroscopic results, that is to say, the mean volume of the particles increases by $\approx 1000\,nm^3$ per aliquot addition (Figure 4.2a). Most important, we observe no change upon the fifth addition of ascorbic acid further proving the hypothesis.

In conclusion, the yield of Au_0 is determined by the amount of ascorbic acid present in the reaction solution. Ascorbic acid is the species delivering the electrons needed for the reduction of Au^+. The amount of reactive gold ions can be calculated by

$$c(Au^+) = 2[c(H_2Asc) - c(Au^{3+})]$$
$$\forall\, c(H_2Asc) > c(Au^{3+}) \quad \text{und} \quad c(H_2Asc) < 1.5c(Au^{3+}) \tag{4.3}$$

5

GROWTH KINETIC OF A ROD-SHAPED METAL NANOCRYSTAL

5.1 INTRODUCTION

Combining SAXS and UV-VIS spectroscopy to investigate particle growth and extract $L(t)$ and $D(t)$

SINCE there is no reliable way to arrest metal nanoparticle growth, most investigations of nanoparticle synthesis focus on the final nanoparticles. Recent in-situ single particle optical spectroscopy of immobilized particles first yielded dynamic results, but the substrate, restricting the accessible surface for further growth, alters the growth dynamics seriously and makes a comparison to batch experiments difficult.[32,38] Small angle x-ray scattering (SAXS) allows for the study of the size and shape of particles in solution and directly yields the growth kinetics, provided a strong x-ray source (synchrotron) makes sufficient time resolution possible. Recently, this in-situ SAXS method has been used to study nucleation and growth of spherical gold nanoparticles prepared by the Turkevich method[39] and to elucidate the influence of a capping agent on the seed formation.[40]

Here, I use a combination of SAXS and optical extinction spectroscopy to investigate the formation of two anisotropic systems: The well-studied and established gold nanorods and nanorods from a gold-copper alloy - a synthesis I only very recently reported.[41] The latter represents one of the first metal alloy nanoparticle synthesis protocols. The optical and SAXS spectra allows me to extract the mean particle width $D(t)$ and the mean length $L(t)$. I find that both length and width independently follow an exponential growth behavior with different time-constants, which intrinsically leads to a switch between positive and negative aspect ratio growth during the course of the synthesis. This switching from "1D" (mainly extension in length) to "3D" (extension in all directions) growth is accomplished without a change in growth mode and limits the aspect ratio of the final products to about 3 (from an aspect ratio of 5, which would theoretically result from a difference in initial growth rates in the two orthogonal directions).

5.2 RESULTS AND DISCUSSION

I prepare growth solutions containing a surfactant (cetyl-trimethyl-ammonium-bromide, CTAB), gold salt and (if applicable) copper ions, a trace of silver nitrate and enough ascorbic acid to reduce the metal ions to their monovalent state (details are described in the methods section). The growth of rod-shaped nanoparticles is initiated by the addition of preformed seeds - small gold particles of about 2 nm to 4 nm. in diameter prepared separately with the reduction of gold ions with sodium borohydride - and completed within 10 min to 20 min. After adding the seeds, a syringe pump draws the solution containing

the growing particles through transparent tubing, first to a self-made flow-through optical spectrometer and then through a thin glass capillary exposed to the x-ray beam. Typical examples of SAXS data and optical extinction spectra are shown in Figure 5.1a and b, respectively. The measurement is started in the moment of seed addition.

The optical spectra contain information about the mean particle volume V and the mean aspect ratio L/D.

The optical spectra contain information about the mean particle volume V and the mean aspect ratio L/D. For the gold nanorods produced here, the long-axis plasmon resonance wavelength depends linearly on the aspect ratio via the relationship[42] $\lambda_{res}/nm = 96L/D + 418$. This experimentally confirmed relationship, reported for gold nanorods, is unknown for other materials, specifically the gold-copper alloy used in some of my experiments. For off-resonance, the extinction cross section is directly proportional to the particle volume and independent of its shape. Since material composition, charges on the particle, the dielectric function of the medium around the particles, and the exact form of the particle surface significantly influence the plasmon resonance wavelength, optical ensemble spectra alone are insufficient to determine particle shapes. This is particularly true for samples composed of different materials, like the gold-copper alloy particles I study here, because the dielectric function for them is unknown.

Using mathematical models or power laws SAXS provides size and shape information

Small-angle x-ray scattering is less sensitive to the above-mentioned factors, complicating particle morphology determination from optical spectra. However, particle size and shape analysis from SAXS is more complex and typically requires fitting mathematical models to the data. The data is often transformed in various ways (e.g. by integration or by multiplication with the scattering-vector q to some power) to highlight certain features in the spectrum. Direct methods are known, which allow for shape fitting in real space[43] while I prefer to fit the scattering curves with known model functions. I used a combination of established methods to extract particle dimensions (length L and diameter D) from the SAXS data, cross-checking the methods against each other and comparing the results with the results from optical spectra (see e.g. Figure 5.2 and Figure 5.6b). I found, in general, good agreement between results from SAXS and optical data.

I extract the particle geometry by fitting all SAXS scattering curves $I(q)$ collected in one experimental run 400 to 800 spectra) with four time dependent parameters:

$$I(q) \propto \int dDdLf(D)f(L)P(q,D,L) \tag{5.1}$$

the average particle length $L(t)$, the average particle width $D(t)$, and its distribution $\sigma_L(t)$ and $\sigma_D(t)$. I assume a cylindrical particle shape:[44]

Modelling with cylindrical form factor and gaussian distributions of particle width and length

$$P(q,D,L) = \int_0^{\pi/2} d\theta \sin\theta \left[\pi \left(\frac{D}{2}\right)^2 L \frac{\sin\left[(qL/2)\cos\theta\right]}{(qL/2)\cos\theta} \frac{2J_1(qD/2\sin\theta)}{qD/2\sin\theta} \right]^2 \tag{5.2}$$

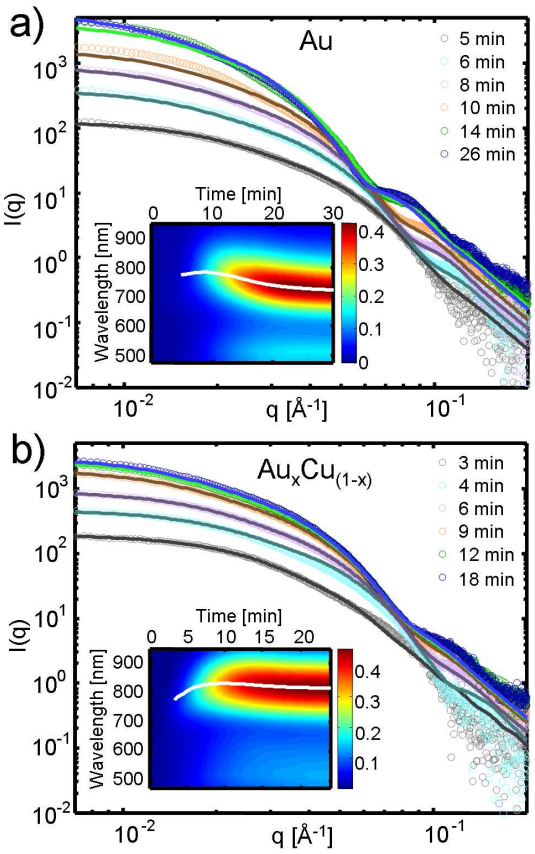

Figure 5.1: Typical SAXS and optical spectra. Experimental small angle x-ray scattering (SAXS) intensities as a function of the scattering vector q for different times after the addition of seeds (colored circles) for a) Au and b) $Au_xCu_{(1-x)}$. The solid lines are fits using a cylindrical form factor. The dip indicated by an arrow becomes more pronounced over time and the intensity increases, indicating an increasingly defined structure and an increase in volume, respectively. The insets show the extinction shown colorcoded as a function of time (color scale as indicated in arbitrary units). A solid white line highlights the longitudinal plasmon resonance.

where $f(L,\sigma_L)$ and $f(D,\sigma_D)$ represent Gaussian distributions of the particle width and particle length, respectively:

$$f(D,\sigma_D) = \frac{e^{-(D-\bar{D})^2/(2\sigma_D^2)}}{(2\pi)^{1/2}\sigma_D}; \tag{5.3}$$

$$f(L,\sigma_L) = \frac{e^{-(L-\bar{L})^2/(2\sigma_L^2)}}{(2\pi)^{1/2}\sigma_L}; \tag{5.4}$$

In the first few minutes, the SAXS data is too noisy to extract reliable information. Details of the data extraction and validation, including the corrections for a sudden x-ray-beam intensity drop in one experiment, are described in Section 5.4.

Another robust value that can be extracted from SAXS data is the so-called invariant

$$\int dq I(q) q^2 \tag{5.5}$$

which is proportional to the volume fraction of solid materials in the solution. Therefore, the invariant is proportional to the mean particle

Invariant is proportional to the mean particle volume at constant particle number

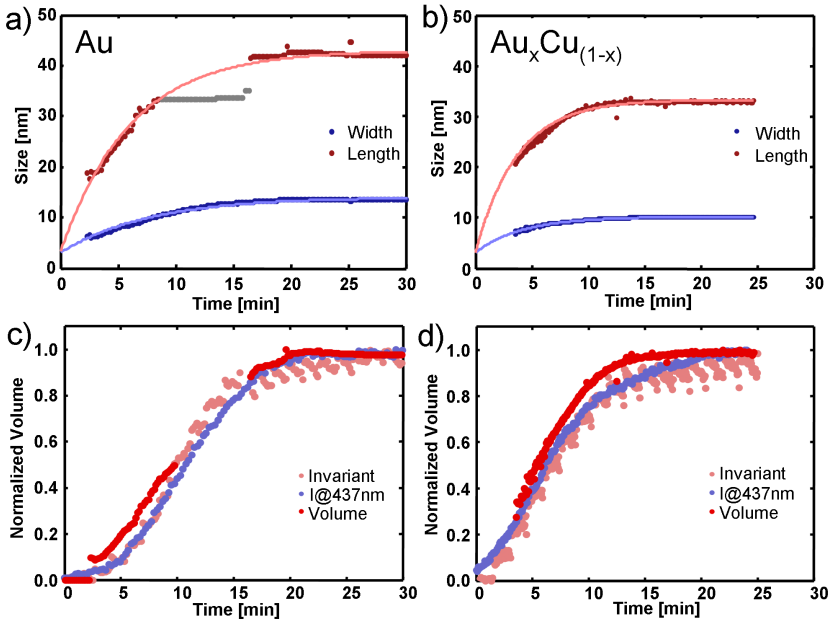

Figure 5.2: Size parameters during particle formation for gold (left) and gold-copper alloy particles (right). (**a**, **b**) evolution of length L and width D over time for gold nanorods and gold-copper alloy nanorods, respectively, during growth. The solid lines are fits of the form $L_\infty(1-e^{-t/T})+D_0$. (**c**, **d**) Normalized "invariant" (total SAXS scattering intensity $I(q)$ integrated as $\int dq I(q)q^2$), normalized optical extinction at $\lambda = 437$ nm and normalized particle volume calculated from length and width data in a, b, respectively. Invariant and optical off-resonance extinction are both proportional to the particle volume in the absence of new nucleation and show the same time evolution as the calculated volume, which shows the consistency of both SAXS and optical results. The gray dots indicate areas where the data points are not reliable (compare Figure 5.6).

volume assuming that the particle number does not change throughout the synthesis.[45] The invariant should follow the same time dependency as the off-resonance optical extinction value, which is indeed the case, for both gold and gold-copper alloy particles (Figure 5.2c, d, respectively).

The increase of particle length L is well described by the function

$$L(t) = L_\infty(1-e^{-t/T_L}) + D_{seeds} \tag{5.6}$$

where D_{seeds} is the initial seed diameter of 3 nm and $L + D_{seeds}$ the final particle length. The decay time T_L and final length parameter L are best understood in terms of the growth rate dL/dt, which shows that L/T_L is the initial growth rate and T_L describes the slowing down of the reaction speed as the reactants are consumed:

$$\dot{L} \equiv dt/dL = (L_\infty/T_L)e^{-t/T_L} \tag{5.7}$$

Hence, the mathematical form of the time-dependency for the particle length (Equation 5.6) and width follows an exponentially decaying growth rate. For pure gold rods, I find decay constants

$$T_L = 6.0\,\text{min} \quad \text{and} \quad T_D = 7.8\,\text{min}$$

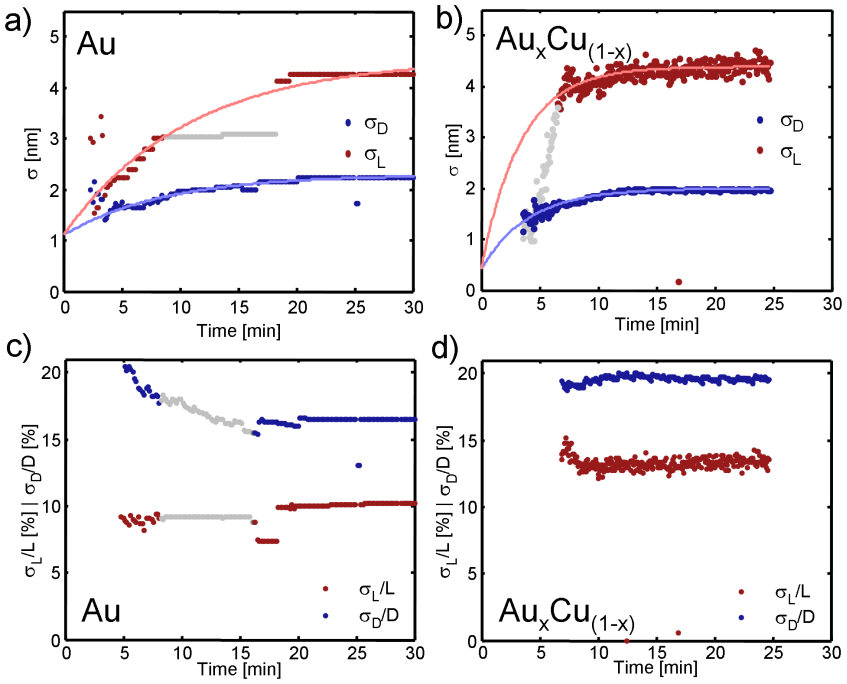

Figure 5.3: a,b σ_L and σ_D as extracted by the formfactor fitting for gold and gold-copper alloy rods, respectively. c,d Relative size distributions over time. For the relative size distributions σ_L/L and σ_D/D I observe a nearly constant value throughout the growth. In other words, the relative size distributions remains preserved.

for the length and width, respectively, and initial growth rates of

$$L_\infty/T_L = 6.7\,\mathrm{nm\,min^{-1}} \quad \text{and} \quad D_\infty/T_D = 1.4\,\mathrm{nm\,min^{-1}}.$$

For gold-copper alloy rods, the growth is faster, with decay constants of

$$T_L = 3.7\,\mathrm{min} \quad \text{and} \quad T_D = 4.2\,\mathrm{min}$$

and initial growth rates of

$$L_\infty/T_L = 8.2\,\mathrm{nm\,min^{-1}} \quad \text{and} \quad D_\infty/T_D = 1.7\,\mathrm{nm\,min^{-1}}.$$

In both cases, the growth-rate decay time is about 10 to 20% shorter in the direction of the long axis compared to the short axis and the initial growth rate in the direction of the long axis is about five times larger than the initial growth rate in the perpendicular direction. During the synthesis, the relative size distributions $\Delta L/L$ and $\Delta D/D$ stay approximately constant. For gold rods, the values are around 16.5% and 10% for the short and long axis, respectively, for the gold-copper alloy rods 19.5% and 14% (compare Figure 5.3). Therefore, the polydispersity of the sample does not increase over time, which indicates a well-controlled growth mode.

The relative size distributions $\Delta L/L$ and $\Delta D/D$ stay approximately constant

To check the consistency of the extracted length and width information with the total particle volume increase extracted from the invariant or the optical off-resonance extinction, I calculate $V(t)$ from $L(t)$ and $D(t)$ assuming cylinder-shaped particles. The agreement I find

(see Figure 5.2c/d) shows the self-consistency of the data. The volume increase rate in the linear part of the curve is about $5\,\mathrm{nm}^3\,\mathrm{s}^{-1}$ in both cases, which is the same as published earlier.[32]

The volume increase rate in the linear part is about $5\,\mathrm{nm}^3\,\mathrm{s}^{-1}$

A key parameter for plasmonic nanorods is their aspect ratio $AR = L/D$, which is the main factor influencing their optical properties, in particular their long-axis plasmon resonance wavelength. Figure 5.4 compares the ensemble resonance wavelength with the aspect ratio calculated from the SAXS spectra. In both cases (Au and AuCu), the general behavior is similar. Within the latter time window, the resonance wavelength is still changing whereas the aspect ratio stays constant, most likely due to intraparticle ripening that changes the nanorod end-cap geometry but not the overall dimensions. A change in the end-cap geometry shifts the plasmon resonance wavelength by as much as 25 nm.[30] This discrepancy between optical and SAXS data highlights the importance of using both methods parallel to one another.

The apparent shift from 1D to 3D growth is caused simply by the mathematics of the system

The extracted time dependency for width and length gives new light to a puzzling phenomenon observed in nanorod growth: particles first grow longer (1D growth) but at some point in time, the particles "become fat" (3D growth), i.e. the aspect ratio decreases. It was often speculated that there is a shift in the growth mode at this point in time, for example because of the depletion of reactants or accumulated strain in the nanocrystal lattice.[46,38] Similar effects (1D-growth, followed by 3D-growth and 1D/2D ripening) have been reported on CdSe nanorods and qualitatively explained in terms of reaction kinetics and size-dependent chemical potential.[47,48,49] Now, I can explain the apparent shift from 1D to 3D growth simply by the mathematics of the system without a change in growth mechanism, using experimentally confirmed growth parameters

At the time the maximum aspect ratio is reached: $\frac{\dot{L}}{\dot{D}} = \frac{L}{D} \equiv AR$

The aspect ratio $AR = L/D$ reaches its maximum at

$$\frac{d}{dt}\left(\frac{L}{D}\right) \stackrel{!}{=} 0 \Rightarrow \frac{\dot{L}}{L} = \frac{\dot{D}}{D} \Leftrightarrow \frac{\dot{L}}{\dot{D}} = \frac{L}{D} \equiv AR \tag{5.8}$$

where $\dot{L}$ denotes the time derivative of L. This means that, at the time the maximum aspect ratio is reached, the relative length increase dL/L per time dt equals the relative width increase dD/D per time dt. If the relative length increase is larger than the relative width increase, the aspect ratio grows:

$$\frac{\dot{L}}{L} > \frac{\dot{D}}{D} \Leftrightarrow \frac{\dot{L}}{\dot{D}} > AR. \tag{5.9}$$

Accordingly, the aspect ratio decreases when

$$\frac{\dot{L}}{\dot{D}} < AR. \tag{5.10}$$

Note that the intuitive relations Equation 5.9 and Equation 5.10 also mathematically follow from the time derivative of AR without any prior assumptions regarding the growth model or particle shape.

I have extracted dL/dt and dD/dt from $L(t)$ and $D(t)$ described by the exponential growth model (Equation 5.6). Indeed, I observe a

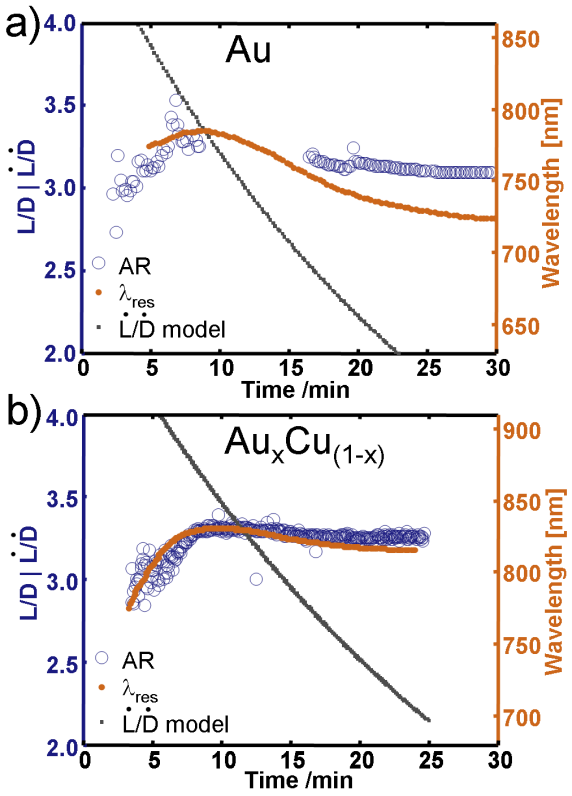

Figure 5.4: Evolution of the aspect ratio during synthesis for gold (top) and gold-copper alloy (bottom) nanoparticles. a), b), comparison of measured plasmon resonance wavelength and aspect ratio (AR) determined by SAXS for gold and gold-copper alloy nanorods, respectively. Both show generally the same trend. I calculate the ratio of dL/dt to dD/dt from the L and D data shown in Figure 5.2 fitted by the exponential model (gray dots).There is a crossover with $AR = (dL/dt)/(dD/dt)$ at t =8 min and t =12 min, respectively. The discontinuity in the SAXS data for the aspect ratio of gold nanorods is an artifact due to the x-ray-beam intensity drop, leading to inadequate background correction. I indicated the unreliable data after the intensity drop in light blue.

crossover from $(dL/dT)/(dD/dt) > AR$ to $(dL/dt)/(dD/dt) < AR$ at 8 min to 12 min after the reaction starts, which is approximately the same time after which the maximum aspect ratio is reached (Figure 5.4a/b). The maximum aspect ratio and the change from 1D to 3D growth is therefore a consequence of the exponential growth behavior with two different growth-rate decay times in length (T_L) and width (T_D). If the growth rate stayed constant at their initial values, the aspect ratio of the particles would asymptotically approach the ratio of these initial growth rates, i.e. reaching an aspect ratio of about AR = 5.

The question is of course what causes the exponential decrease in the growth rate and the five-fold difference in the initial growth rates in the two directions along and perpendicular to the rod's long axis. Possible factors for the slowing down of the reaction speed include: depletion of a reactant, blocking of the particles surface,[50] or a critical surface to volume ratio because of strain in the crystal.[51] In my case, depletion of a reactant seems likely since multi-step synthesis protocols lead to larger particles.[52] I believe there is a surface reac-

tion of metal ions reduced by ascorbic acid on the nanoparticle surface. The amount of ascorbic acid in the growth solution is enough to reduce 20% of the Au(I) or Cu(I) ions after reducing Au(III) to Au(I). Therefore, the saturation behavior can be explained as a depletion of ascorbic acid (see Chapter 4).

In crystals like CdSe, the different free energies of the Cd- and Se-terminated crystal facets are responsible for the anisotropic growth.[48] The mechanism for anisotropic growth speed for mono-atomic fcc crystals like gold is less obvious and might involve effects of electric fields in addition to the varying reactivity of the crystal faces in the [100] and [111] directions.[53,50,54] Further studies of the initial growth rates under various chemical conditions should shed light on this question. The fact that I have observed different growth-rate decay times T_L and T_D suggests different chemical potentials for metal reduction at the two surfaces, which limits the reaction at different precursor concentrations. The different adsorption affinity of CTAB for the two surfaces as proposed by Murphy et al.[50] could be a reason for the difference in growth-rates as well.

The reaction rate in both directions is relatively slow if compared to the value calculated for purely diffusion-limited growth. The smallest CTAB micelles are 5 nm in diameter[55], which yields a diffusion coefficient $D = 7.6 \times 10^{-11}\,\mathrm{m^2\,s^{-1}}$. A CTAB micelle consists of about 100 molecules,[55] which gives a CTAB micelle a concentration of around 1×10^{-4} M in my solution or approximately 5 gold ions per CTAB micelle. To form a rod with a length of 40 nm and width of 14 nm, it would take less than a second in a purely diffusion limited regime. There is therefore an unknown rate-limiting step in the metal ion reduction process on the nanoparticle surface, which is both unusually slow and occurs with different speeds along the two crystal directions, along and perpendicular to the long nanorod axis. Diffusion through a CTAB surface layer may be the reason for this slow step. Earlier, I observed a reduction in nanoparticle aspect ratio at higher growth temperatures,which is another hint for activation-controlled growths.[49]

In conclusion, the time evolution of nanorod formation extracted in parallel with SAXS and optical spectroscopy shows a simple exponentially decreasing growth rate. The initial growth rate in the long nanorod direction is five times larger than in the short axis direction. Both rates decrease exponentially with a slightly faster time-constant for the long axis, which leads to a switch from 1D to 3D growth after about 8 min to 12 min and reduces the aspect ratio of the final products to about three. The experimentally determined time constants and growth models discussed here will aid the development of more detailed molecular simulations for gold nanorod growth.

5.3 EXPERIMENTAL SECTION

SEED SYNTHESIS. 50 µL of 0.1 M tetrachloroauric acid ($HAuCl_4$) are added to 5.0 mL Milli Q water and mixed with 5.0 mL of 0.2 M cetyltrimethylammoniumbromide (CTAB) solution. During vigorous

shaking, 0.60 µL of ice-cold 0.010 M sodiumborohydrid ($NaBH_4$) is added resulting in the formation of a brownish-yellow or yellow suspension of seeds. The seed suspension is kept at 30 °C and used within one day.

SYNTHESIS OF AU-NANOPARTICLES. A growth solution containing 5.0×10^{-4} M $HAuCl_4$, 0.10 M CTAB, 4.0×10^{-5} M silvernitrate ($AgNO_3$) and 5.5×10^{-4} M ascorbic acid (AA) is prepared. AA changes the growth solution from dark yellow to colorless. After the addition of 12 µL of seeds, the solution changes color to blue or grayish-red within 10 min to 20 min.

SYNTHESIS OF AUCU-NANOPARTICLES. 25 µL of 0.1 M $HAuCl_4$ and 25 µL of 0.1 M copper (II) chloride ($CuCl_2$) are added to 5.0 mL Milli Q water and mixed with 5.0 mL of 0.2 M CTAB solution. 10 µL of 0.04 M $AgNO_3$ and 52.5 µL of 0.0788 M ascorbic acid are added. The reducing agent changes the growth solution from dark yellow to colorless. After the addition of 12 µL of seeds, the solution gradually changes color within 10 min to 20 min.

SETUP. I prepared 10 mL of growth solution in a beaker and injected the seeds. The solution containing the growing nanoparticles was drawn with a syringe pump (Harvard Instruments) through a polyvinylchloride (PVC) tubing (inner diameter 1 mm) to the measuring points separated by approximately 0.2 m of tubing. The flow rates were 3000 µL min^{-1} for the first 60 s, then 100 µL min^{-1} for the rest of the experiment. The optical spectra were acquired before the solution went through the capillary (mark capillary 100 µm), where the SAXS pattern was measured.

SAXS. The experiments were performed at the X12SA beamline at the Swiss Light Source, Paul Scherrer Institut, Villigen, Switzerland. An energy of 9.6 keV was used with an energy resolution of $\Delta E/E < 0.02$. The flight tube was 2.1 m in length. Two-dimensional SAXS patterns were acquired with the PILATUS 2M detector and azimuthally integrated to yield the SAXS intensity $I(q)$.

BACKGROUND CORRECTIONS. To account for the background signal, the tubing was pre-flushed with 0.1 M CTAB solution and measured before each synthesis. The first 10 to 20 scattering spectra therefore contain the scattering pattern of the CTAB micelles, the capillary itself, and all other background signals. The background spectra were averaged and subtracted from the measured spectra afterwards. In the case of the gold rod synthesis, I had to correct the data additionally because of a sudden drop in intensity during the measurement (see Figure 5.5). Since the intensity change due to the loss was much faster than the change of the growing nanoparticles, I took the average of 10 frames before and 10 frames after the intensity loss (for each q separately) and corrected the data with the difference of the averages. This correction helped to extract reasonably smooth data.

OPTICAL SPECTROSCOPY. Spectra were acquired directly through the tubing using an OceanOptics USB4000 Spectrometer equipped with an OceanOptics HL-2000-FHSA halogen lamp. The reference spectrum was measured with pure 0.1 M CTAB solution.

5.4 DATA EXTRACTION AND VERIFICATION

DATA ANALYSIS. Small-angle x-ray scattering spectra contain information about the particle radius of gyration, the volume, and the length/width of the particles assuming a priori a particular particle form (i.e. a 'formfactor'). These parameters are extracted by either evaluating slopes of the q-weighted or logarithmic scattering cross section $I(q)$, i.e. $\log(Iq)$ vs. q^2 (Guinier) or by integrating $\int dqI(q)q^2$ (the 'invariant'). I have used all of these methods, and comparing the results among each other's and with the results from the optical spectra.

LENGTH AND WIDTH I calculated the particle length and width using formfactor fitting with a normal distribution (Equation 5.2, Equation 5.3, Equation 5.11, Equation 5.12). The formfactor P(q,D,L) I use is that of a cylinder (Equation 5.2).

$$I(q) = (\Delta\rho)^2 n \int dDdLV(D,L)^2 f(D) f(L) P(q,D,L) \tag{5.11}$$

represents the electron density difference between the particles and the solvent (matrix) and n the particle number density. I combine those two parameters (which do not change over time) with the particle volume V during the fitting procedure. The distribution $f(L)$ is assumed to follow a Gaussian function with mean $\bar{L}$, distribution σ_L (Equation 5.3). The same applies for the particle width D. The particle volume V is given by :

$$V(D,L) = \pi\left(\frac{D}{2}\right)^2 L \tag{5.12}$$

The formfactor P of a cylinder is given by Equation 5.2. J_1 represents the first order Bessel function of the first kind. The free parameters V,D, L, σ_D and σ_L were adjusted by least-squares fitting or manual when the features in the scattering curve were not pronounced enough for automatic fitting.

BACKGROUND CORRECTION. Before the experiment, I flushed the capillary with CTAB-solution, which enabled me to use the first 10 frames as background (scattering due to CTAB). The mean of these first 10 frames was subtracted from all subsequent frames (see Figure 5.5).

DATA ADJUSTMENT FOR MEASUREMENT ARTIFACTS. For the gold sample, there was a sudden drop of intensity after about 400 frames (see Figure 5.5, b-d). Because the optical extinction did not change significantly during this time interval, I consider this sudden

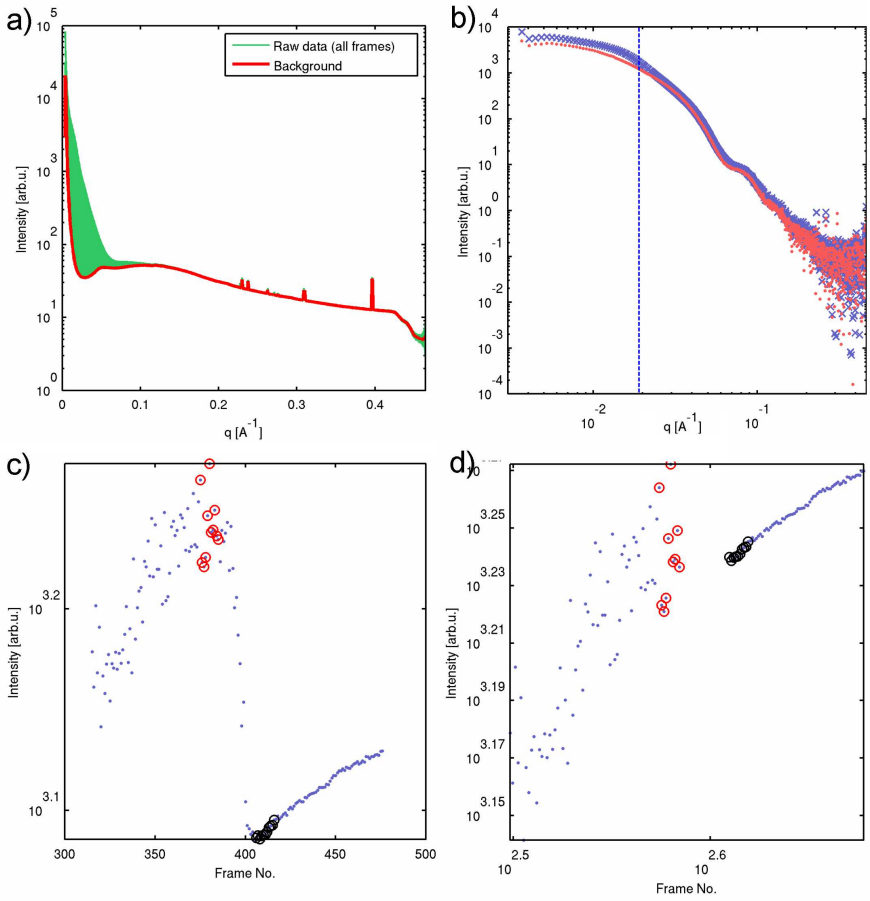

Figure 5.5: (a) Background correction: the mean of the first ten frames (red line) is subtracted from all subsequent data (green). (b) Scattering curve before (blue crosses, frame 385) and after (red dots, frame 406) the intensity drop. The scattering intensity at $q = 0.02\,\text{Å}^{-1}$ (dashed blue line) as a function of time is shown in (c) and (d) with and without the correction (respectively).

intensity drop in the SAXS data as a measurement artifact caused by X-ray beam instability or a deposit in the capillary. I corrected my SAXS data by calculating (for each q) the mean intensity of the ten frames directly before and after the intensity drop and added the difference to the intensity after the drop. Figure 5.5 (c) and (d) show the intensity for $q = 0.02\,\text{Å}^{-1}$ (blue line in panel b) as a function of time (frame number). However, the above mentioned data correction does not allow to extract reliable values for particle length and its length distribution because the scattering curve shows an additional oscillation at low q. This low q feature cannot be described by a cylindrical form-factor alone. A bimodal fit (cylinders + spheres) describes the curve better than a pure cylinder fit in the low q region (Figure S2), which might indicate the presence of additional small particles in the solution for times between 8 and 16 minutes. Whether those spheres are gold-nanospheres or crystallites of precipitating CTAB is unclear. I exclude the length information for the named time interval for further analysis. The linear part ($q^2 \approx 0.001\,\text{Å}^{-2}$ to $0.003\,\text{Å}^{-2}$) of the curve is described by the cylinder fit nearly as good as the bimodal fit, which means I can still extract particle width information.

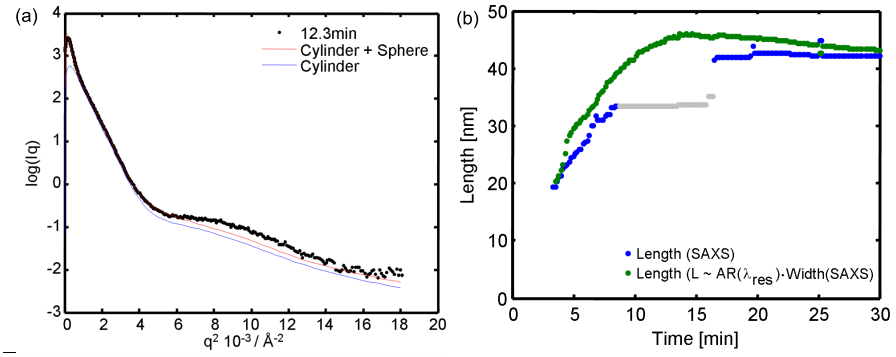

Figure 5.6: (a) Scattering curve at 12.3 min in a $\log(Iq)$ vs. q^2 plot. The bimodal fit (cylinders + spheres) can describe the curve better than the cylinder fit, especially in the low q region. (b) Cross-checking the length extracted by SAXS with length using the resonance-wavelength. The evolution of both curves is similar and the deviation is in the range of 10%. The difference after 20 min is probably due to changes in the end-cap geometry.

CROSS-SECTIONAL RADIUS OF GYRATION. I calculated the particle width also using the Guinier approximation:

$$I_c q = I_c q(0) e^{-q^2 R_x^2/2} \tag{5.13}$$

Within this approximation, the slope in the logarithmic scattering intensity $\log(I(q)q)$ vs. q^2 gives $R_x^2/2$ (Figure 5.7a/b). From R_x, it is possible to calculate the width of elongated particles.

$$R^2 = 2R_x^2 \tag{5.14}$$

I compared the particle width obtained by the Guinier approximation with the width from the formfactor fitting (Figure 5.7c/d). Both agree within less than 5%.

COMPARISON OF OPTICAL AND X-RAY DATA. The particle length extracted from optical and x-ray data are consistent with each other within a few % (Figure 5.6b).

SAMPLE POLYDISPERSITY. The time-dependency for the distribution in length and width can be described by the same function as the length and width itself (see Figure 5.3). For pure gold rods, I find decay constants $T_{\sigma_L} = 10.9$ min and $T_{\sigma_D} = 8.7$ min and for gold-copper alloy rods decay constants $T_{\sigma_L} = 3.4$ min and $T_{\sigma_D} = 4.1$ min. The decay constants are in the same range as for the length and width itself. The relative size distributions $\Delta L/L$ and $\Delta L/D$ give approximately constant values around 16.5% and 10% for the short and the long axis for gold rods and 19.5% and 14% for the short and the long axis for gold-copper alloy rods. Therefore, the polydispersity of the short and the long axis does not increase in the accessible time interval of 5 min to the end of growth.

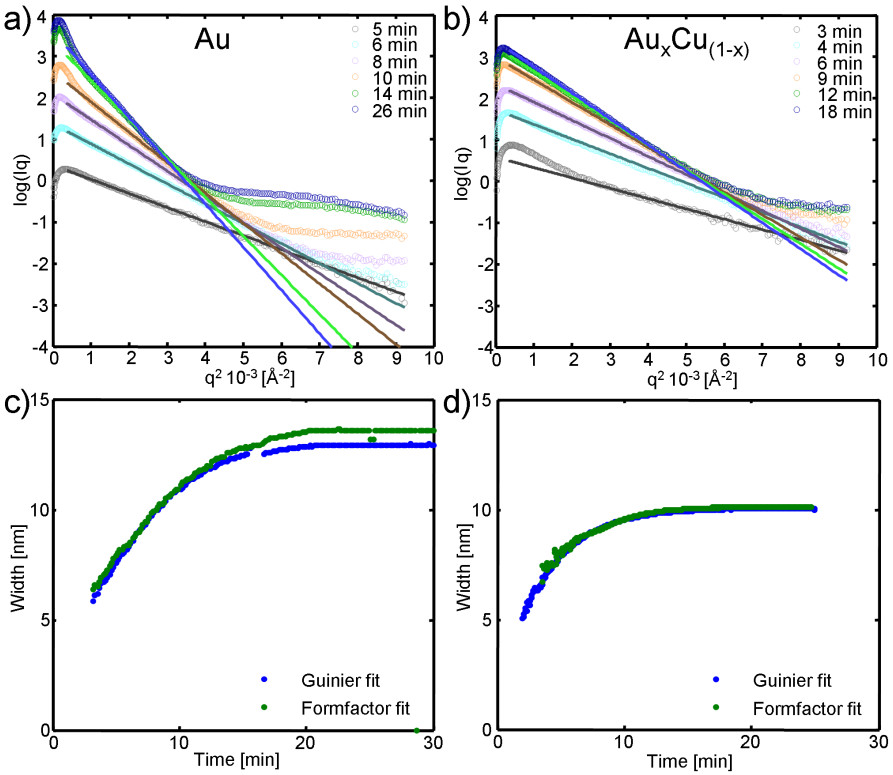

Figure 5.7: (a),(b) Scattering curves plotted as $\log(Iq)$ vs. q^2 for some time points. Between 8 min to 16 min, I observe a oscillation in the low q region, which strongly deviates from the behaviour expected for a cylinder. This oscillation is due to spherical particles as explained in Figure 5.6 a. The linear part can be used to extract the short axis using the Guinier-law. (c),(d) Comparison of the width extracted using the guinier law and the formfactor fit. In general both curves agree very well. In the case of Au, I observe a deviation of ≈0.5 nm for later times, that is to say a deviation of ≈ 3.5%.

6

GROWTH KINETICS OF ROD-SHAPED METAL NANOCRYSTALS REVISITED

6.1 INTRODUCTION

ALTHOUGH the growth kinetics of gold nanorods has been studied by optical spectroscopy or more thoroughly using SAXS, some aspects of the growth remain puzzling.[56] Among them, the reduction pathway, the role of CTAB and the role of silver. The whole course of growth has been resolved by SAXS in a ten-fold concentrated solution by Hubert et al.[57] and the influence of ascorbic acid has been studied more closely but a complete comprehensive study of the influence of each single component in the growth solution is still missing. Until now, the role of ascorbic acid as electron donor seems to be widely accepted in the community although the exact pathway of reaction either directly reducing Au^{+} on the surface of the growing rod or recovering Au^{+} from Au^{3+} generated by a disproportionation reaction[58] is not clear. About the influence of CTAB concentration there is only little work in the literature. It is assumed that CTAB blocks the sides of the rods allowing it to elongate and a soft-template mechansim has also been proposed. A complex of silver-ions and CTAB has been revealed.[59] Hence, one might imagine a similar complex with Au^{+}. The role of silver itself remains puzzling although different possibilities have been discussed for example the underpotential deposition of elemental silver[60] or the adsorption of AgBr.[61]

A complete comprehensive study of the influence of each single component in the growth solution is still missing

Here, I study the influence of each entity in the growth solution on the kinetics of the growth except ascorbic acid using simultaneous SAXS and UV-VIS spectroscopy. Differently to my work shown in Chapter 5, I extract the apparent rate constants for length and width growth using a Boltzman function (Equation 6.1). Each component in the growth solution is varied keeping the others constant. Only the ratio of ascorbic acid to initial gold salt is always kept constant. I find a linear relation of the rate constants as a function of $[HAuCl_4]/[CTAB]$ ratio as well as the rate per seed as function of $[HAuCl_4]/[seed]$ ratio. Furthermore, I see a correlation of final aspect ratio and ratio of rate constants for length and width growth rate for different silver to Au ratios. On very high silver concentrations only spheres are obtained as expected from earlier work.

I varied each component ($AgNO_3$, Seeds, CTAB) in the growth solution individually, keeping the others constant (only $Au^{3+}/Asc = const$ always)

6.2 RESULTS AND DISCUSSION

I planned several series of experiments, varying one component only in each series. Varying one component influences the ratios to the other components in growth solutions. Since the ratios between the components have been discussed in literature to influence the growth

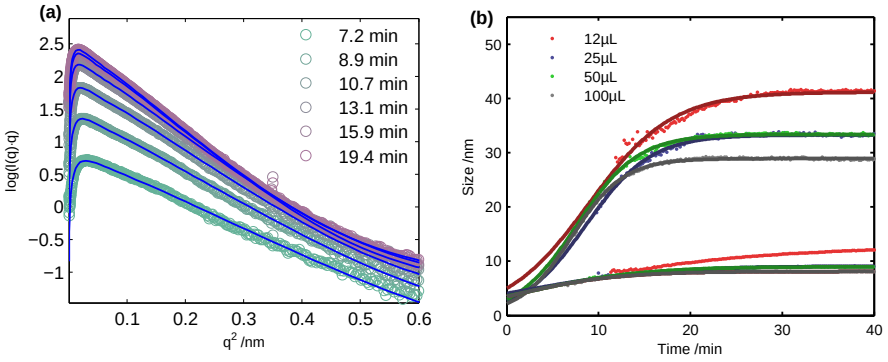

Figure 6.1: (a) Scattering curves with their fits at different times during the growth for one experiment. (b) Example for the evolution of the average length and diameter as extracted from the SAXS curves together with the corresponding fits using the Boltzman function (Equation 6.1). This series corresponds to the variation of seed added to the growth solution containing 0.25 mM $HAuCl_4$, 0.1 M CTAB, and 0.04 mM $AgNO_3$.

of the particles, these are the dimensions we use to investigate the changes in the rate constants. The preparation of the growth solutions and the experiments were done as described in Chapter 5. This time, I used a longer flight tube to gain more information at smaller q-vectors, hence larger sizes. A typical set of scattering curves with corresponding fits for one experiment and the extracted sizes L and D for a series of experiments are shown in Figure 6.1.

Again, for the extraction of L, D, σ_L, and σ_D, I used the formfactor of a cylinder. For some experiments, I used the formfactor of a sphere to extract the diameter D and σ_D, since neither the scattering curves exhibit the features of a cylinder nor the TEM images showed a significant amount of rods. This was the case for growth solutions having a large $AgNO_3/HAuCl_4$ ratio. Typically, scattering curves could be fitted starting from 4 min to 8 min after injection of the seeds to the end of the growth. The curves were too noisy in the first few minutes to extract reliable information except the invariant - the measure of the volume fraction of the particles.

Using mathematical models or power laws SAXS provides size and shape information

In Chapter 5, I used an exponential function to describe the growth of the particles, but in the new measurements, I found that the increase of particle length is better described by a Boltzman function

$$L(t) = \frac{L_i}{(1 - L_i/L_\infty)e^{-k_L t} + L_i/L_\infty}, \tag{6.1}$$

where L_i is the initial seed diameter of 2 nm to 4 nm[60] and L_∞ the final particle length. The rate constant is then given by k_L. The same applies to the increase of particle width with D_i, D_∞, and k_D. The mathematical form of the time-dependency for the particle length (Equation 6.1) and width follows an exponentially growth with a limiting resource, i.e. the available reactive gold-ions. In the following, I will discuss the influence of each chemical, i.e. $AgNO_3$, Seeds, CTAB, individually. If not stated differently, all SAXS curves were evaluated using the same

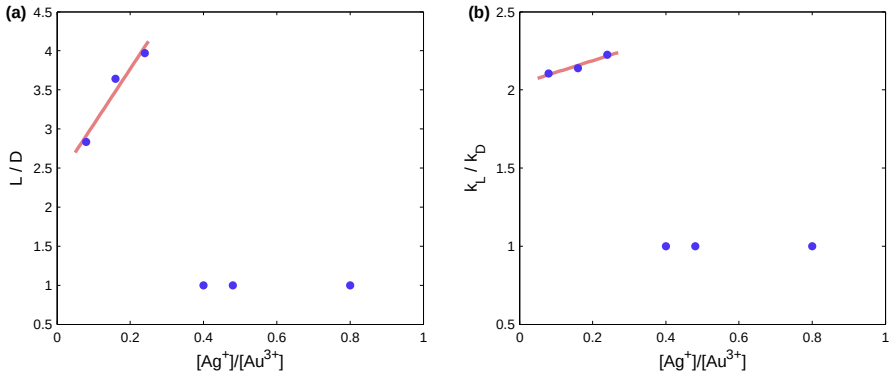

Figure 6.2: Variation of Ag to Au ratio.

procedure as described in the experimental section and the resulting traces of $L(t)$ and $D(t)$ were fitted using Equation 6.1.

INFLUENCE OF SILVERNITRATE. Up to now, the influence of $AgNO_3$ has been studied most in a static way, i.e. varying the silver to gold ratio and looking at the final particles either spectrally or using TEM. In only a few publications, continuous spectroscopy was used to investigate the course of the synthesis for different silver concentrations.[46] The role of silver in the gold rod synthesis has been subject to intense speculation. Various options have been proposed, for example, the underpotential deposition of elemental silver[60] or the adsorption of AgBr.[61] Although the exact mechanism remains hidden, the effect of varying the silver to gold ratio is well-known — increasing this ratio leads to a red-shift of the plasmon resonance by formation of long rods and overdoing it produces spheres or at least sphere-like structures.

I used the silver concentrations of 0.04 mM, 0.12 mM and 0.2 mM for gold concentrations of 0.25 mM and 0.5 mM, hence, I was sampling silver to gold ratios of 0.08, 0.16, 0.24, 0.4, 0.48 and 0.8. For the experiments with silver to gold ratios bigger 0.24, the SAXS curves didn't exhibit features of cylindrical particles but rather features of a sphere and therefore, the formfactor of a sphere was used for evaluation. The apparent rate constants and final sizes were extracted and are shown in Figure 6.2.

First, as shown in Figure 6.2a, I found the well-known trend of an roughly linear increase in aspect ratio upon an increase in silver to gold ratio until it is too high ($\gtrsim 0.3$) and only — or at least mostly — spherical particles are formed (in the TEM images a few percent of the particles are slightly rod shaped). Additionally, I found this trend again in the ratio of the rate constants (Figure 6.2b). Therefore, our measurements show a correlation of the ratio of the rate constants and the aspect ratio of the particles. Furthermore, I found an overall decrease in the rate constants with increasing silver to gold ratios, which points towards a retarding effect of silver on the depostion of gold on the growing rods, which has also been observed by Bullen et al.[56]

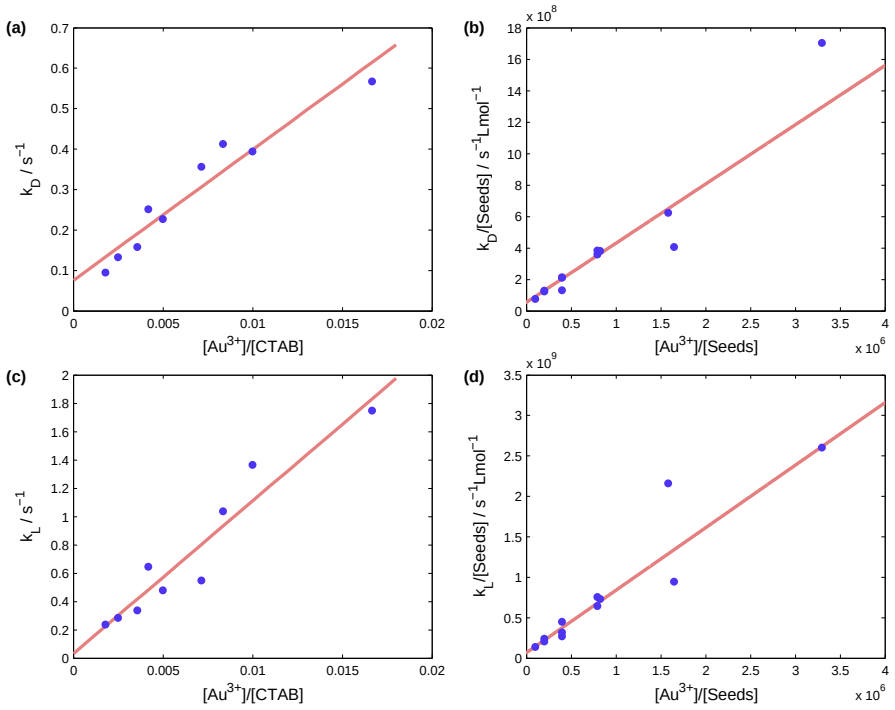

Figure 6.3: Variation of Au to CTAB ratio and Au to Seed ratio.

INFLUENCE OF CTAB From the theoretic point of view the speed of the reaction should be influenced by the concentration of CTAB because of its micellar properties. Changing the concentration leads to a change in micelle size (and even micelle shape for extreme concentrations). With micelle size, the diffusion speed will change and assuming that the gold-ions are adsorbed to the micelles, this should influence the rate of monomer consumption. Even more obvious, the amount of gold-ions per micelle will change by the size and amount of micelles in solution. On the other hand, changing the gold concentration will change this loading, too. Therefore, I expected a change in the rate constant as function of gold to CTAB ratio.

To study the influence of CTAB, I used 0.06 M, 0.1 M and 0.14 M for gold concentrations of 0.25 mM, 0.5 mM and 1 mM, hence, I was sampling gold to CTAB ratios of 1.8×10^{-3}, 2.5×10^{-3}, 3.6×10^{-3}, 4.2×10^{-3}, 5×10^{-3} and 8.3×10^{-3}. For each experiment, the background was measured with the appropriate CTAB-concentration. The apparent rate constants and final sizes were extracted and are shown in Figure 6.3a and c.

I found a linear relationship of the rate constant as function of gold to CTAB ratios. This can be explained by the facts mentioned above. Small gold to CTAB ratios can be achieved at high CTAB concentrations and/or low gold concentrations. Increasing the CTAB concentration will lead to larger and slower diffusing micelles and to lower amount of gold-ions per micelle. A low gold concentration in turn would also give a small loading of the micelles. In the experiment, I actually find the slowest rates exactly for these cases. Whereas for large gold to CTAB ratios the CTAB concentration is small and the gold concentration is high, hence, the micelles are smaller and dif-

fusing faster carrying more gold-ions making the reaction faster. The measurements seem to be consistent with this view of micelles carrying gold-ions and different micelle sizes. Additionally, changing the micelle size could lead to a change in steric interaction at the surface of the nanoparticles.

INFLUENCE OF SEEDS I used different amounts of the seed solution (12 µl, 25 µl, 50 µl and 100 µl), hence, I varied the concentration of seeds[1] (0.030×10^{-8} M, 0.063×10^{-8} M, 0.127×10^{-8} M and 0.253×10^{-8} M) for gold concentrations of 0.25 mM, 0.5 mM and 1 mM. Therefore, I was sampling the gold to seed ratios of 0.099×10^{6}, 0.198×10^{6}, 0.395×10^{6}, 0.791×10^{6}, 0.824×10^{6}, 1.582×10^{6}, 1.648×10^{6} and 3.395×10^{6}. Results are shown in Figure 6.3b and d.

For this series, I found an almost linear relationship of the rate constants per seed as function of gold-ions per seed. This follows the intuitive aspect that providing more seeds will lead to a slower consumption per seed. Interestingly, the relation stays linear also for high gold to seed ratios although I did expect a saturation effect somewhere. At some point there should be a ratio at which the rate per seed can't get higher since the reaction should be limited by the surface area.

In conclusion, the apparent rate constants with SAXS show linear behaviour as function of gold to CTAB, gold to seed, and silver to gold ratio. From the simple relationship of rate constants to gold/CTAB ratio, I conclude that the picture of gold-ion loaded CTAB micelles is in deed very likely. Interestingly, I find an increase of per seed growth rate when less seeds or more gold ions are present. The experimentally determined time constants discussed here will aid the development of more detailed molecular simulations for gold nanorod growth.

6.3 EXPERIMENTAL SECTION

SEED SYNTHESIS. 50 µL of 0.1 M tetrachloroauric acid ($HAuCl_4$) are added to 5.0 mL Milli Q water and mixed with 5.0 mL of 0.2 M cetyltrimethylammoniumbromide (CTAB) solution. During vigorous shaking, 0.60 µL of ice-cold 0.010 M sodiumborohydrid ($NaBH_4$) is added resulting in the formation of a brownish-yellow or yellow suspension of seeds. The seed suspension is kept at 30 °C and used within one day.

SYNTHESIS OF AU-NANOPARTICLES. A growth solution containing 0.25 mM, 0.5 mM and 1 mM $HAuCl_4$, 0.06 M, 0.1 M and 0.14 M CTAB, 0.04 mM, 0.12 mM and 0.2 mM silvernitrate ($AgNO_3$) and 10% excess ascorbic acid (AA) with respect to the gold concentration is prepared. AA changes the growth solution from dark yellow to colorless. After the addition of 12 µl, 25 µl, 50 µl and 100 µl of seeds, the solution changes color to blue or grayish-red within 10 min to 50 min.

1 The seed concentration was calculated assuming an average diameter of 3 nm for the seeds and assuming 100% yield in the preparation of the seed solution.

SETUP. I prepared 10 mL of growth solution in a beaker and injected the seeds. The solution containing the growing nanoparticles was drawn with a syringe pump (Harvard Instruments) through a polyvinylchloride (PVC) tubing (inner diameter 1 mm) to the measuring points separated by approximately 0.2 m of tubing. The flow rates were 3000 µL min^{-1} for the first 60 s, then 100 µL min^{-1} for the rest of the experiment. The optical spectra were acquired before the solution went through the capillary (mark capillary 100 µm), where the SAXS pattern was measured.

SAXS. The experiments were performed at the X12SA beamline at the Swiss Light Source, Paul Scherrer Institut, Villigen, Switzerland. An energy of 11.5 keV was used with an energy resolution of $\Delta E/E < 0.02$. The flight tube was 7 m in length. Two-dimensional SAXS patterns were acquired with the PILATUS 2M detector and azimuthally integrated to yield the SAXS intensity $I(q)$.

BACKGROUND CORRECTIONS. To account for the background signal, the tubing was pre-flushed with 0.1 M CTAB solution and measured before each synthesis. The first 10 to 20 scattering spectra therefore contain the scattering pattern of the CTAB micelles, the capillary itself, and all other background signals. The background spectra were averaged and subtracted from the measured intensities afterwards.

For several measurements, I observed a change in the background signal in the SAXS data during the growth. This change manifested at larger q-values (small features) and was included in the modeling of the SAXS curves using the debye function for gaussian coils (REF eq:Debye equation for gaussian coil

$$F(q) = \frac{2e^{-R_g^2 q^2} + R_g^2 q^2 - 1}{(R_g^2 q^2)^2}. \tag{6.2}$$

If necessary, this polymeric background was substracted before the particle sizes were modelled either with a formfactor for cylinders or spheres. Interestingly, the R_g increased over time and might point to some changes in the CTAB layer at the nanoparticles surface. This could be investigated systematically in more detail in another measurement session.

OPTICAL SPECTROSCOPY. Spectra were acquired directly through the tubing using an OceanOptics USB4000 Spectrometer equipped with an OceanOptics HL-2000-FHSA halogen lamp. The reference spectrum was measured with pure 0.06 M, 0.1 M, and 0.14 M CTAB solution.

7

BMBF - NANOPOLYMERIC CONTRAST AGENTS FOR PHOTOACOUSTIC IMAGING

THE research project “nanopolymeric contrast agents for photoacoustic imaging" (short title: POLYSOUND) was a joint project of the Fraunhofer Institute for Biomedical Engineering (IBMT), the Centre for Biomaterial Development (GKSS, part of Helmholtz-Zentrum Geesthacht Centre for Materials and Coastal Research), and our group from 2007-2010. This project was funded by the German Federal Ministry of Education and Research BMBF (contract number 0312029). In the following two paragraphs, I will state the aim of the project as outlined in the proposal and our final results. An overview is of the overall outcome is shown in Section 7.1.

AIM OF THE PROJECT The aim of the proposed feasability study was a proof of principle of the concept of photoacoustic imaging in biomaterials comparing NIR-absorbing nanoparticle polymers (which will degrade and be egested by natural matabolism) and gold nanorods (with plasmon resonance that can be tuned to meet application requirements). During the project run time, the establishement of a three-dimensional resolving, photoacoustic microscopy setup and the synthetic pathway to new biodegradable organic semiconductors, which work as constrast agent for photoacoustics were pursued. The technical evaluation with respect to clinical usability as well as the biomedical evaluation with respect to the biocompatibility and biodegradation shall be used to predict applicability. In case of positive outcome the usability of the technical concept can be investigated for concrete diagnostic problems in follow-up studies. The technical evaluation shall be done using the gold nanorods that are ideal in terms of the photoacoustic properties but whos toxicity in biological systems is not answered yet. The procedure offers the potential of an minimal-invasive, low-cost, and easy to use diagnostic with scalable observation depths from micrometer to centimeter range. At the University Mainz, the established nanorod synthesis shall be extended to provide nanorods that absorb light at 1064 nm since powerful commercial laser systems are available at this wavelength.

OUR RESULTS The final results are summarized in the next Section 7.1, which is a reprint of a conference paper presented at the 34th International Conference and Exposition on Advance Ceramics and Composites. Since my part in the project was the synthesis of nanorods with appropriate spectral properties, understanding the growth of rods was the major topic for me. The results that I obtained investigating the latter were shown in chapters 3 to 6.

Since I couldn’t find a reliable way of preparing nanorods with an absorption at 1064 nm and a reasonable yield, I changed the surfac-

tant in the synthesis as proposed in literature.[62,63] For this, I synthesized the surfactants cetyltri**ethyl**-ammonium bromide (CTEAB) and cetyltri**propyl**-ammonium bromide (CTPAB) by reacting 1-bromohexadecane and the appropriate trialkylamine in acetonitrile. After heating to reflux for 24 h, the product crystallized at room temperature. Recrystallizing in ethyl acetate, washing with diethylether and drying in vaccum at 50 °C yielded the clean product according to NMR. MALDI-TOF showed a molar mass[1] of $m/z = 360\,\mathrm{g\,mol^{-1}}$ and $m/z = 405\,\mathrm{g\,mol^{-1}}$ for CTEAB and CTPAB, respectively, and verifyied a clean product.

Using CTPAB I obtained nanorods with a broad absorption peak around 1100 nm (Figure 7.2). Size analysis of the samples with TEM showed (39.4 ± 9.2) nm in length and (6.4 ± 1.0) nm in width and a huge fraction ($\approx 50\%$) of spheres. These particles were used for the biomedical and technical evaluationof our project partners either as synthesized or with a PEG-functionalization. Although they show the right absorption wavelength they lack in absorption crosssection since the volume of the particles is quite small. To improve this, I investigated the synthesis of gold nanorods in surfactant mixtures in the last months of the project run time. Adding CTEAB or CTPAB to a growth solution containing 0.1 M CTAB, the plasmon resonance is red-shifted compared to synthesis with CTAB only. Upon an addition of up to 30% CTEAB or CTPAB the plasmon resonance shifts to longer wavelength; the red-shift being more pronounced in the case of CTPAB. Although this synthesis yields a high yield of rods ($\approx 50\%$) and bigger sized particles ((47.4 ± 5.0) nm in length and (9.0 ± 1.3) nm in width), the plasmon resonance can't be shifted beyond 1000 nm.

7.1 EVALUATION OF NANOPARTICLES AS CONTRAST AGENT FOR PHOTOACOUSTIC IMAGING IN LIVING CELLS

7.1.1 *Introduction*

Due to the intrinsic properties of nanostructured materials, like biological barrier transfer, nanoparticles are explored to be used in the medical field.[64,65] At the current state of art nanoparticles are planned to be used as drug delivery -, controlled release - and cell tracking systems, for example in stem cell research. Beside these applications nanoparticulate material, especially metal nanostructures work as contrast agent for medical diagnosis.[66,67] Due to their strong signal per molecular recognition site nanoparticles are of great interest, especially as contrast agents for diagnostic molecular imaging. Particulate contrast agents are currently approved for ultrasound imaging and magnetic resonance imaging.

Beside ultrasound imaging, photoacoustic imaging represents a more sensitive method to be used for diagnosis. Photoacoustic imaging is an emerging non invasive radiation free imaging technique combining beneficial features from optical and ultrasound tech-

1 Molar mass without the bromide ion.

niques.[68,69] In this modality, ultrasound signals are generated by absorption of pulsed laser radiation according to their elastic effect. This modality allows acoustical imaging of biological structures with optical contrasts and supports the use of nanoscaled contrast agents with strong optical absorption in the context of molecular imaging. Several biocompatible particle systems with encapsulated Indocyanine green (ICG) have been developed for bio imaging and therapy.[70] Their maximum optical absorption is located at 750 nm wavelength. In this spectral range only cost-intensive and technically complex laser systems can be used for photoacoustic signal generation. In contrast to the cost-intensive OPO laser systems, Nd:YAG lasers emitting 1064 nm light are widely used in scientific, medical and industrial routine and combine cost-efficiency with technically relevant features such as stability and easy handling. Accordingly, the optical absorption properties of photoacoustic contrast agents have to be tuned so that their spectral maximum corresponds to the wavelength of the laser used for signal generation. The spectral absorption of gold nanoparticles depends highly on their size and aspect ratio. Due to the high resonant surface plasmon oscillation gold nanoparticles are used for several applications. In the medical field gold nanoparticles attracted much attention as photothermal agent in hypothermia, as drug-delivery agents and biosensors.[71] Due to its biocompatibility and biodegradability poly(D,Llactide- co-glycolide) (PLGA) is one of the most utilized materials in the biomedical field and used as scaffolds in bio engineering, implants and as particulate drug delivery systems.[72] Nanoincapsulation of near infrared dyes in a Food and Drug Administration (FDA) accredited material like PLGA is a new approach in particle preparation. The perchlorate IR5 exhibits such absorption maximum, however no information about cytotoxicity and metabolism is yet known. The approach of this study involves the development of two different groups of nanoparticles with an absorption maximum at the relevant laser wavelength of 1064 nm which is widely accessible in common laser systems. With regard to future in vivo applications the cytotoxic effects of the particle systems were determined.

7.1.2 *Results and discussion*

NANOPARTICLE CHARACTERIZATION. Polyethylenglycol (PEG)-modified gold nanorods were prepared by mixing CTPAB-stabilized gold nanorods with PEG, which reduces their rate for clearance. PEG-modified gold nanorods with an aspect ratio of 5:1 resulting in an absorption maximum in the NIR at 1064 nm were synthesized. Analyzing the TEM images of the PEG-modified gold nanorods (Figure 7.1A) the size distribution of the nanorods with an absorption maximum at 1064 nm (Figure 7.1B) revealed a mean size between of (39.4 ± 9.2) nm in length and (6.4 ± 1.0) nm in width. The zeta potential of the gold nanorods, without PEG-modification and after PEG-functionalisation, were determined. Gold nanorods stabilized in CTPAB have a cationic surface. Their zeta potential conducts 31.0 mV. This was due to ab-

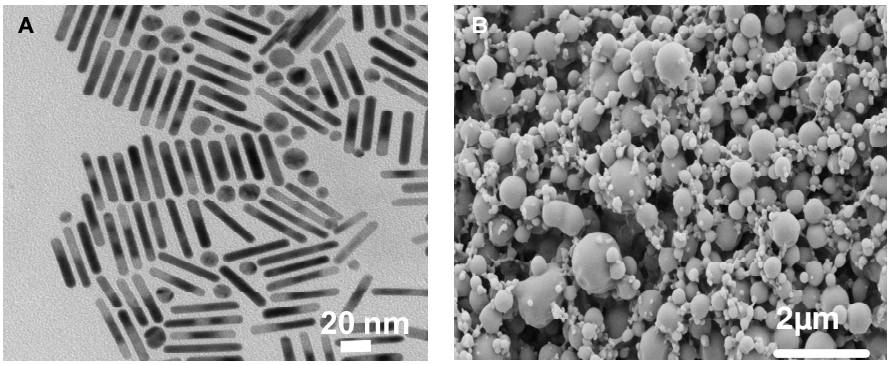

Figure 7.1: Characterization of the synthesized gold nanoparticles. Transmission electron microscopic images of gold nanorods with a mean size of 40 nm in length and 11 nm in width (A). Scanning electronic microscopic images of IR5-loaded PLGA particles with a diameter in the range of 100 nm to 600 nm(B).

sorbed CTPAB that has amine as hydrophilic head. PEG-modified gold nanorods showed also a cationic surface (18.3 mV).

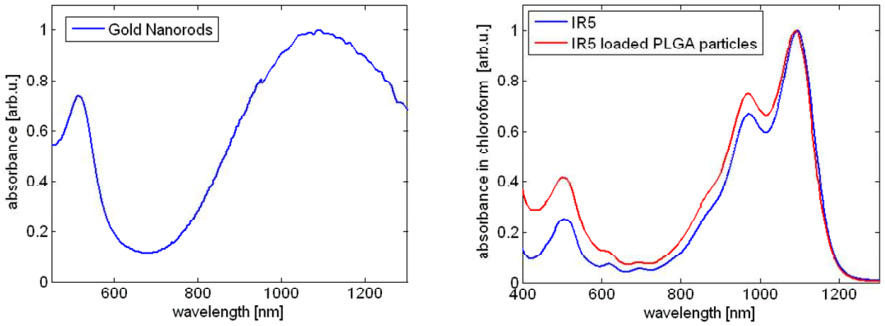

Figure 7.2: Absorption spectra of the synthesized gold nanoparticles (left), the IR5-loaded PLGA particles and the pure dye IR5 (right). Both nanoparticle systems possess an absorption maximum in the range of 1100 nm.

By spray drying IR5-loaded PLGA particles were synthesized (Figure 7.1B). IR5, with unknown cytotoxic potential, was encapsulated in the PLGA particles by spray drying. The size distribution of the IR5-loaded PLGA particles revealed a mean diameter of 324 nm. The absorption spectra of the pure IR5 dye and the dye-loaded PLGA particles prepared in chloroform was measured (Figure 7.2). IR5-loaded PLGA particles show a specific absorbance in the NIR at 1100 nm, which is comparable to that of the pure dye. The zeta potential of the dye-free PLGA particles has a value of (-13.25 ± 0.35) mV and decreases by IR5-loaded particle preparation ((-24.05 ± 0.31) mV). This fact could be caused by the IR dye molecules which are located also on the surface of the particles.

CYTOTOXICTY EXPERIMENTS. The cytotoxicity of PEG-modified gold nanorods and IR5-loaded PLGA nanoparticles in human hepatocellular cells (HepG2) was evaluated. HepG2 cells were derived from the human liver, one of the major organs of metabolism and biotransformation and assumed as location of nanoparticle clearance and pos-

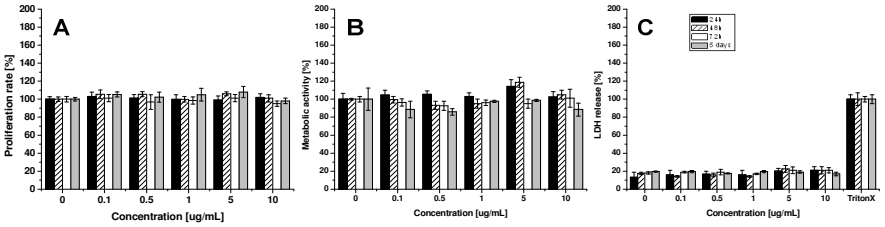

Figure 7.3: Effect of PEG-functionalized gold nanorods with an absorption maximum at 1064 nm on the viability of HepG2 cells. Cells were treated with different concentrations (0 µg mL^{-1} to 10 µg mL^{-1}) of PEGmodified gold nanorods with an absorbance maximum at 1064 nm. After 24 h, 48 h, 72 h and five days of exposure the effect on cell proliferation (A), metabolic activity (B) and membrane integrity (C) was quantified. Data are expressed as mean ± SD (n = 3). Control cells without gold nanorods treatment are 100%.

sible accumulation. Due to these facts, to study the biotransformation and to simulate the metabolism of the nanoparticles in the human body, HepG2 cells were used as in vitro cell culture test system. The

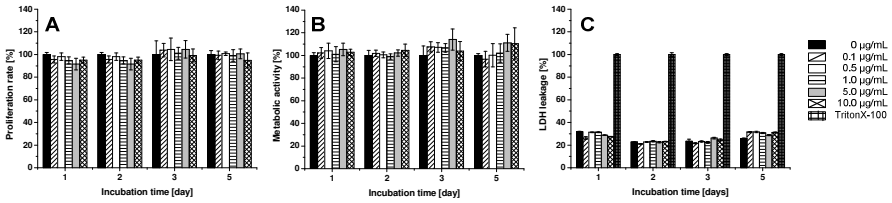

Figure 7.4: Effect of IR5-loaded PLGA nanoparticles with an absorption maximum at 1100 nm on the viability of HepG2 cells. Cells were treated with different concentrations (0 µg mL^{-1} to 10 µg mL^{-1}) of PEGmodified gold nanorods with an absorbance maximum at 1064 nm. After 24 h, 48 h, 72 h and five days of exposure the effect on cell proliferation (A), metabolic activity (B) and membrane integrity (C) was quantified. Data are expressed as mean ± SD (n = 3). Control cells without gold nanorods treatment are 100%.

cytotoxic potential of the synthesized nanoparticles in a concentration range of 0.1 µg mL^{-1} to 10 µg mL^{-1} were investigated. The metabolic activity was determined using the WST-1 assay. Following four different exposure times (24 h, 48 h, 72 h and five days), quantitative analyses of cell viability was carried out. The gold nanorods with PEG surface modifiers did not appear to be cytotoxic in HepG2 cells at concentrations up to 10 µg ml^{-1}. Even after five days of chronically exposure no decrease in metabolic activity was induced (Figure 7.3A). Also the IR5-loaded nanoparticles are biocompatible up to 10 µg ml^{-1} using the WST-1 assay (Figure 7.4A).

Via BrdU assay the PEG-modified gold nanorods induced no significant decrease in proliferation rate of the HepG2 cells after 24 h, 48 h, and 72 h at the concentration of 10 µg ml^{-1}, even after 5 days of exposure the proliferation rate remained constant at the level of the control (100%) (Figure 7.3B). Also the IR5- loaded nanoparticles are biocompatible up to 10 µg mL^{-1} using the BrdU assay (Figure 7.4B). Dye-free PLGA particles also appear to be non-toxic in HepG2 cells at concentrations up to 10 µg mL^{-1}, even after 5 days of chronically exposure

(data not shown). Membrane integrity after exposure to the prepared nanoparticles was investigated by the LDH assay. These results give evidence on cellnanoparticle interaction. Compared to the nanorod-free control no LDH (lactate dehydrogenase) leakage was induced by any of the PEG-modified gold nanorods (Figure 7.3C) and IR5-loaded PLGA nanoparticles (Figure 7.4C). The exposed nanoparticles induce a LDH leakage of 20%, which correlates to the noise level of the system. The results of the cytotoxicity studies indicate biocompatibility of the nanoscaled materials prepared within this study.

PHOTOACOUSTIC IMAGING. This ultra sensitive detection platform allows high resolution imaging of infrared absorbing structures

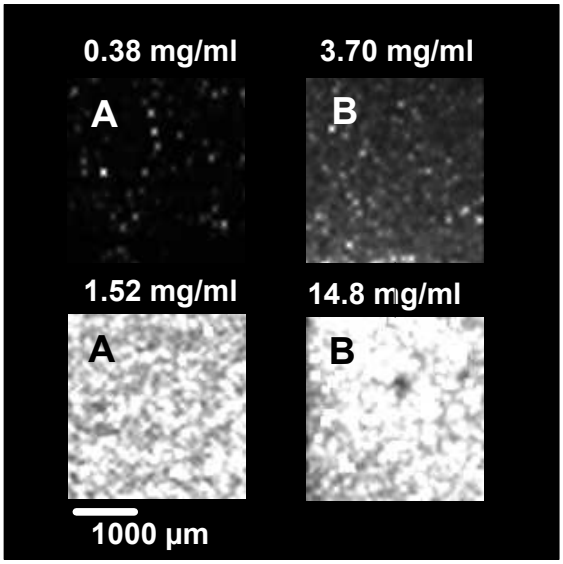

Figure 7.5: Concentration-dependent photoacoustic imaging of PEG-functionalized gold nanorods (A) and IR5- PLGA nanoparticles (B) embedded in agarose.

and can especially be used for nanoparticle detection. After embedding different concentrations of the new developed nanoparticles in an agarose matrix photoacoustic images were taken by using the maximum amplitude protection (Figure 7.5).

The signal amplitudes of the two nanoparticle concentrations were displayed (Figure 7.6). In both cases the detected signal amplitude correlates to the particle concentration. An increasing amount of nanoparticles results in an increase of the signal-to-noise ratio (Figure 7.6). With the background of the biocompatibility experiments the prepared PEG-functionalized gold nanorods and IR5-loaded PLGA particles seem suitable for photoacoustic diagnostic purpose up to $10\,\mu g\,mL^{-1}$. Comparing the signal generation of the highest concentrations of both synthesized nanoparticle systems demonstrates the high photoacoustic signal and indicates the bases for the next step on the way to a new class of contrast agents for photoacoustic imaging.

CONCLUSION. Using nanoparticulate contrast agents with an absorption maximum located in the range of 750 nm limits their

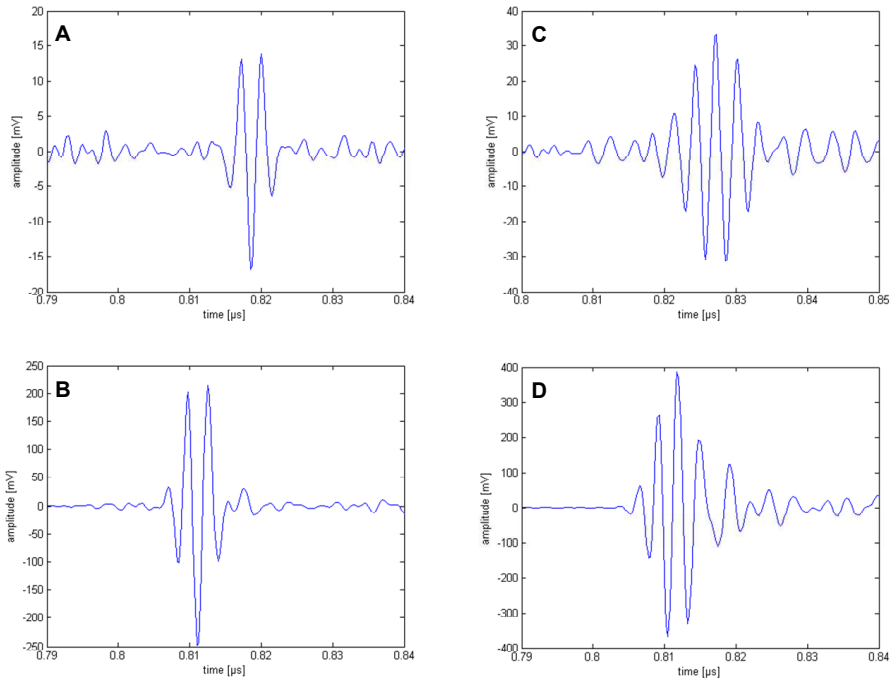

Figure 7.6: Signal amplitudes of PEG-functionalized gold nanorods (A) and IR5-loaded PLGAnanoparticles (B) embedded in agarose. The signal amplitudes were calculated based on the photoacoustic images.

widespread clinical use, because in that spectral range only cost-intensive and technically complex OPO laser systems are available for optoacoustic signal generation. Nd:YAG lasers emitting 1064 nm light. Due to the fact that the synthesized PEG-functionalized gold nanorods and the NIR dye IR5 show an absorbance maximum in the range of 1100 nm, the dyeloaded particles represent a particle system which could be used as photoacoustic contrast agent, in combination with a cost-efficient photoacoustic hardware platform.

The current results of the performed in vitro experiments indicate no cytotoxic potential of both synthesized particle systems. The results of the performed experiments characterise the PEGfunctionalized gold nanorods and the IR5-loaded PLGA particles as a biocompatible nanoparticulate systems for the planned application as contrast agent for photoacoustic imaging. The high optical absorption of the particle systems results in excellent photoacoustical signals comparable to commercially available contrast agents. We have demonstrated for the first time that IR5-loaded PLGA particles present a new class of biocompatible contrast agents for photoacoustic imaging, with absorption in a wavelength regime that allows for higher tissue penetration depth than particle systems proposed by others.

7.1.3 *Experimental section*

PREPARATION OF PEG-FUNCTIONALIZED GOLD NANORODS. Gold nanorods with an absorption maximum at 1064 nm were prepared as described in literature.[62,63] The particles are grown by a seed-mediated synthesis at room temperature. Typically, a growth solution

containing 5.0×10^{-4} M $HAuCl_4$, 0.01 M cetyltripropyl-ammonimum bromide (CTPAB), 4×10^{-5} M $AgNO_3$ and 7×10^{-4} M ascorbic acids prepared. The particle growth starts upon the addition of seed particles - small preformed gold particles (diameter 2 nm to 4 nm) - that are produced separately by reduction of $HAuCl_4$ with $NaBH_4$ in a 0.1 M CTPAB solution. CTPAB, a cationic detergent, is used as stabilizing agent during preparation of gold nanorods. The nanorods were modified with polyethylene glycol (PEG) to optimize the biocompatibility.

PREPARATION OF IR5-LOADED PLGA NANOPARTICLES. The particles are prepared by spray drying. A solution of Poly (D,L-lactide-co-glycolide) PLGA (Reso281, 50:50) and IR5 (8-[[3-[(6,7-dihydro-2,4-diphenyl-5H-1-benzopyran-8-yl)methylene]-1- cyclohexen-1-yl]-methylene]-5,6,7,8-tetrahydro-2,4-diphenyl-1-benzopyrylium perchlorate) suspended in methylene chloride were mixed in a ratio 1:100 and spray dried under inert conditions using the mini spray dryer B-290 (Buchi, Switzerland). The nitrogen spray flow and aspirator rate were kept constant at eight bar. The particles were dissolved in 1% polyvinyl alcohol (PVA) solution. By centrifugation nanoparticle fractions of different size ranges were obtained.

NANOPARTICLE CHARACTERIZATION. The morphology of the nanostructures was investigated by scanning electron microscopy (SEM) (SUPRATM 40 VP). Samples were mounted on an aluminium stub, coated with Pt/Pd and analyzed using a electron voltage of 3 kV. The morphology of the gold nanorods was determined determined by transmission electron Microscopy (TEM) using a FEI Tecnai F30 electron microscope operating at 300 kV. UV-visible absorption spectra were taken on a two-beam UV/VIS spectrometer (Lambda 950, Perkin Elmer, USA). Before absorption measurements the IR5-loaded PLGA nanoparticles, as well as the pure dye IR5, were diluted in chloroform. The UV-visible absorption spectra, recorded at room temperature, ranges from 300 nm to 1400 nm. Zeta potential measurements were performed using a Malvern Instruments Zetasizer Nano (Malvern Instruments Ltd.), operating with a He-Ne laser at 632 nm. Measurements were taken in zeta cells (DTS 1060C).

CYTOTOXICITY EXPERIMENTS. Cytotoxicity studies were performed, using HepG2 cells (ATCC, LGC Promochem, Germany), derived from a human hepatocarcinoma. The cell line is cultured in RPMI 1640 without Lglutamine, supplemented with penicillin/streptomycin, sodium pyruvate, glucose and 10% foetal calf serum (FCS). To monitor the cytotoxic effect of the synthesized nanostructures 10^4 cells/well were seeded in a 96well micro titre plate. At day 2, the adherent cell were washed with PBS and exposed to different nanoparticle-concentrations in the range of 0 µg mL^{-1} to 10 µg mL^{-1} for one, two, three and five days. To achieve these final concentrations the prepared nanorods were diluted in cell culture medium. Each experiment included a positive control, which was TritonX-100 1%.

The mitochondrial function of the cells exposed to the gold nanorods was analyzed using the WST- 1 assay (Roche Diagnostics). This assay is based on the cleavage of stable tetrazolium salt WST-1 by metabolically active cells to an orange formazan dye. WST-1 assay was performed after 24 h, 48 h, 72 h and five days according to manufacturer's instructions, with appropriate controls. After exposure to nanorods the cells were incubated with the WST-1 reagent for four hours. Thereafter the absorbance was quantified at 650 nm using scanning multi-well spectrophotometer reader (Tecan Deutschland). The measured absorbance directly correlates to the number of viable cells.

The detection of the proliferation rate of the cells exposed to nanorods was performed using the BrdU assay kit (Roche Diagnostics). This colorimetric immunoassay is based on the measurement of BrdU (5-bromo-2'-deoxyuridine) incorporation during DNA synthesis. The reaction product is quantified by measuring the absorbance using a scanning multi-well spectrophotometer. To detect the membrane integrity of the cells exposed to the gold nanorods, lactate dehydrogenase (LDH) release is monitored. During the LDH assay (Roche Diagnostics), LDH released from damaged cells oxidizes lactate to pyruvate, which promotes conversion of tetrazolium salt to formazan, a water-soluble molecule with absorbance at 490 nm. 24 h, 48 h, 72 h and five days after nanorod exposition the supernatant of the cells was transferred in a new 96well micro titre plate and mixed with the corresponding volume of LDH reagent. The formazan dye was quantified using scanning multi-well spectrophotometer reader. The amount of LDH released is proportional to the number of necrotic cells.

All experiments were replicated three independent times and the data are presented as mean SD (Standard error of mean). For the in vitro studies, each stock solution was diluted serially to yield the different concentrations (0 µg mL^{-1} to 10 µg mL^{-1}). Each experimental value was compared to the corresponding control value for each time point. Statistical significance versus control (cell culture medium) was established as $p < 0.005$. Statistical tests were performed by one-way ANOVA.

MICROSCOPIC PHOTOACOUSTIC IMAGING. Suitability of gold and IR5-loaded nanoparticles for photoacoustic imaging was investigated using a custom designed photoacoustic microscope with spatial resolution in the µm range. The photoacoustic imaging system (SASAM OPTO) consists of the acoustic microscopy platform (SASAM 1000, kibero GmbH, Germany) (Figure 7.7A).[73,74,75]

The platform is developed on an Olympus IX81 optical microscope with a rotating column that has an optical condenser for transmission optical microscopy and an acoustic module (Figure 7.7B) for the acoustic microscopy. The adapted optoacoustic module consists of a Q-switched Nd:YAG solidstate- laser (Teem Photonics, France) generating sub-nanosecond pulses at kilohertz repetition rates. The solid state laser is coupled to the photoacoustic instrument via single mode fiber (core diameter 5 µm) and is focused on the sample using the microscope optics. Each pulse used in this experiment had a pulse energy

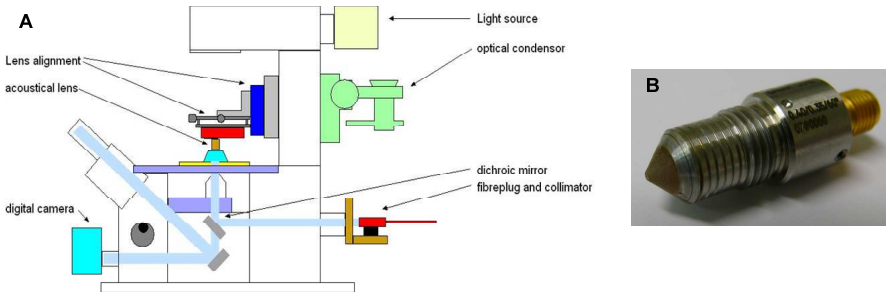

Figure 7.7: Schematic setup of the photoacoustic microscope based on an inverted microscope. Video or/and visual inspection of the sample is possible. To reflect the excitation light to the objective a short pass dichroic mirror with a cut-off wavelength of 700 nm is integrated. Additionally to the photoacoustic imaging mode, all common optical imaging modalities and pure acoustic microscopy are implemented.

of 350 nJ and a duration of 700 ps. The confocal arrangement allowed high signal to noise ratio photoacoustic signals (>30 dB) to be detected at approximately 400 MHz. In imaging mode, the full width at half maximum value (FWHM) was measured to be 3.6 µm for the 400 MHz transducer. The photoacoustic microscope scans point-by-point along the sample surface and converts the received time resolved signals into a two dimensional image by using the maximum amplitude projection (MAP) or into a three dimensional image by using the acoustic wave time of flight. With this newly developed photoacoustic microscope it is possible to evaluate the photoacoustic suitability of different kind of absorbing particles.

Different concentrations of the synthesized nanoparticles were embedded in agarose to perform concentration-dependent measurements using the developed photoacoustic microscope. The photoacoustic signal of gold nanoparticles in the range of 0.38 mg mL^{-1} and 1.52 mg mL^{-1}, and IR5-loaded PLGA nanoparticles in the range of 3.7 mg mL^{-1} and 14.8 mg mL^{-1} were measured. Afterwards the recorded signal amplitudes of each individual samples were compared.

8

HOW TO GET CERTAIN NANORODS

In this chapter, I want to briefly collect some of the trends I have seen in the past years while I was synthesizing a lot of different gold rods. This is less of a scientific summary but more of telling the inside story from a practical point of view.

The seeded growth procedure described by Nikoobakht et al.[36] is widely used now. There, a seed solution is prepared by reduction of $HAuCl_4$ with $NaBH_4$ in the presence of CTAB. In the next step, different amounts of seeds are injected into a growth solution containing $HAuCl_4$, CTAB, ascorbic acid and varying amounts of $AgNO_3$. Varying $AgNO_3$ changes the final aspect ratio of the rods, hence, their resonance wavelength. Often onyl the amount of $AgNO_3$ is changed — sometimes the amount of seeds, too. Besides the variation of the composition of the growth solution, some general — practical — things have to be considered to successfully grow rods at all.

Often I was asked the question „how to make a good seed solution“or „what do I have to do to get rods with a specific resonance wavelength“. Since there are quite some parameters to vary in the synthesis and the mechansim is not fully understood yet, I thought of a diagram where one could select parameters depending on the wavelength range and particle dimension. Furthermore, the knowledge of how to make specific rods is mandatory when experiments are simulated and an optimal particle has been selected. Knowing the optimal sensor doesn't mean anything as long as you can actually synthesize the particles needed. In Table 8.1, I show sets of parameters for 3 different wavelength ranges. Additionally, the need for a specific resonance wavelength rarely comes without the need for a specific dimension of the rods, which makes it of course more difficult. That is why I added the row about the particle volume as a representative for the particle dimension one can expect.

In the following sections, I collect some advices that should help in the preparation of a good seed solution and specific rods with respect to resonance wavelength and rod dimensions.

8.1 SEED PREPARATION

Although the preparation of the seed solution consists only of a few steps, producing good seeds seems to be difficult. A 10 mL solution of 0.5×10^{-3} M $HAuCl_4$ in 0.1 M CTAB is prepared and 600 µL of 0.2 M $NaBH_4$ is added. It is crucial to use really ice-cold water for the preparation of the $NaBH_4$ solution since $NaBH_4$ degrades in water. Furthermore, the shorter the time between dissolution of $NaBH_4$ and the addition to the $HAuCl_4$-CTAB solution the better the seeds (usually the time should be SI3osecond. I use 0.2 M $NaBH_4$ instead of 0.1 M $NaBH_4$ as reported by Nikoobakht et al.[36] to gain more time and to overcome

the problem that $NaBH_4$ degrades in air over time once the bottle was opened.

8.2 ROD PREPARATION

In general, the series of addition when making the growth solution plays a role for the outcome. Especially $AgNO_3$ should be added just emphbefore ascorbic acid otherwise the synthesis tends to be irreproduceible or no rods are formed at all. If the pH is adjusted, for example using HCl, it should be added after $AgNO_3$ and before ascorbic acid.

Another fact is, if the wrong batch of CTAB is used, the seeds will be not as good and it is hard to obtain rods at all. The variation in CTAB batches from different or even the same manufacturer has been adressed[76,77] and it is proposed that varying amounts of trace iodide will change the particle shape produced.[78] This is hard to control expecially when the synthesis shall be established in a new lab. The only work around is to order several different batches, have a try and once a working batch is found, reorder it to have a big stock.

To show how to possibly use Table 8.1, I want to discuss three cases, one from each wavelength range.

		λ_{res} / nm	
Chemicals	600 to 800	700 to 850	700 to 1200
$HAuCl_4$ /M		$5 \cdot 10^{-4}$	
CTAB /M	0.06 to 0.14	0.06 to 0.14	0.09 to 0
CTEAB or CTPAB /M	-	-	0.01 to 0.1
$AgNO_3/HAuCl_4$		0.08 to 0.25	
HCl /M	0 to 0.02	-	-
$H_2Asc/HAuCl_4$	1.1 to 1.3	1.1	1.1
Seeds /µl		0.6 to 100	
Particle volume	medium-big	medium	small

Table 8.1: Concentrations or ranges of concentrations for possible compositions of growth solutions for rod growth. For volumes smaller 10 µL, the seed solution was ten-fold diluted to prevent pipetting errors.

HOW TO MAKE (THIN) HIGH AR RODS? High aspect ratio rods (Figure 8.1a) will be very thin and have resonances in the infrared. High volume particles are not available in this area, at least in the wet-chemical approach. In principle, you need to change the surfactant from CTAB to CTEAB or CTPAB and otherwise stay in the midrange of the given concentration ranges otherwise as a starting point. If the right resonance wavelength is missed, change the $AgNO_3/HAuCl_4$ ratio or the amount of seeds. When only CTEAB is used the resonance wavelength of the rods will be beyond 1000 nm and 50% of the particles will be spheres. Separation of spheres and rods is hardly possible since the particle volume of the sheres and the rods is very similar.

The average particle volume is around 1000 nm^3. If a higher particle volume is needed, binary mixtures of CTAB and CTEAB or CTAB and CTPAB have to be used, with maximal 0.05 M CTEAB or CTPAB in the growth solution. The diameter increases and the particle volume will be around 3000 nm^3. No matter what composition is used in this case, the particle dimensions will be small, i. e. rod diameters up to 10 nm and lengths up to 50 nm.

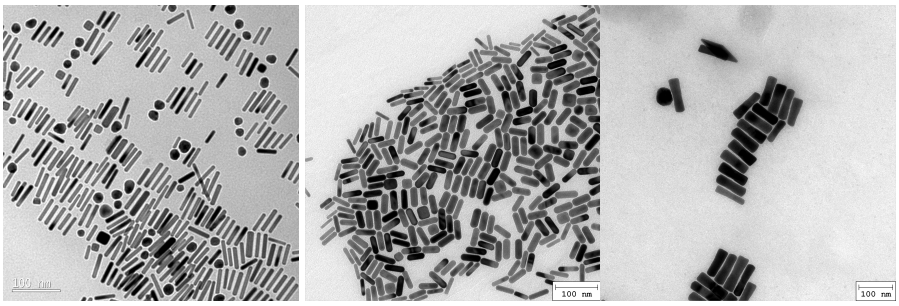

(a) High AR rods **(b)** Medium sized rods **(c)** High volume rods

Figure 8.1: TEM-images of 3 different rod samples

HOW TO MAKE RODS WITH RESONANCE 700 nm TO 800 nm? For these rods (Figure 8.1b), it is a good start to stick with the procedure by Nikoobakht et al.[36]. The growth solution would consist of 0.5×10^{-3} M $HAuCl_4$, 0.1 M CTAB, $AgNO_3/HAuCl_4$ ratio of 0.8 to 1.2, $H_2Asc/HAuCl_4$ ratio of 1.1, and about 25 µL of Seeds. In the range of 0.08 to 0.14 the resonance wavelength scales approximately linear with the $AgNO_3/HAuCl_4$ ratio. This offers the possibilitiy to prepare particles with both $AgNO_3/HAuCl_4$ ratio of 0.08 and 0.12 and to interpolate linearly between the measured resonance wavelengths to find the right $AgNO_3/HAuCl_4$ ratio for the a specifically needed resonance wavelength. These particles will have diameters in the range of 10 nm to 20 nm and lengths of up to 50 nm or 60 nm. Note that the dimensions and especially the diameter is reduced when increasing $AgNO_3/HAuCl_4$ ratio.

HOW TO MAKE FAT RODS? Rods with large diameters (Figure 8.1c) can have their resonances in the range of 600 nm to 800 nm. To achieve large volumes, there are two options. The first one is to increase the $H_2Asc/HAuCl_4$ ratio to 1.2 or 1.3 and to lower the amount of seeds. From there, the precise resonance position can be tuned by the $AgNO_3/HAuCl_4$ ratio again as explained the previous paragraph. This will yield particles with diameters between 20 nm and 30 nm.The second option would be to lower the pH by adding HCl and using a very low amount of seeds. Then the $AgNO_3/HAuCl_4$ ratio can also be increased up to ≈ 0.3 if needed. The particles will have large diameters of up to 50 nm and lengths of up to 100 nm.

Part III

PHYSICS

9

BUILDING THE SETUP

DARK-FIELD microscopy has become a popular tool for investigating nanoparticles and is the most important technique in our group. In constrast to a bright-field microscope, it directs the light under an oblique angle to the sample plane using a dark-field condensor. No light is collected by the objective if there is nothing in the sample plane that scatters light. This produces inverted “colours" in the image compared to a bright-field microscope — a black or dark background with bright objects.

The plasmonic particles we use for single particle experiments are very small (<100 nm, hence, smaller than the diffraction limit) and can not be easily observed in a bright-field-microscope — the change in transmitted light is too small to be detectable without sophisticated detection methods.[79] The dark-field configuration is a well-suited technique for observing the scattered light of single plasmonic particles expecially since good dark-field condensors provide a very high contrast. Like in observing the stars in the sky, a problem is the dynamic range. If you have big dust particles that scatter light strongly it is hard to see the nanoparticles in this area. Even finding smaller particles in a sample with bigger ones can be very challenging.

Besides the imaging, there is the possibilty to do dark-field spectroscopy. Classically this is simply done by moving the image of a particle to a pinhole that directs the scattered light to a spectrometer. Usually, this is a very time consuming procedure if you want to obtain a representative ensemble of particles of a sample. Additionally, to measure repeatedly the same particles after changing the environment is impractical. Therefore a more automized spectra acquisition is desirable. There are several possibilities to obtain spectra of many particles on a given sample and some have been realized in our group already. Jan Becker used a two-dimensional array of shutters in the image plane to collect spectra of many spots separated in the vertical dimension (simultaneously).[32] This method is superior in taking simultaneous time traces of particles but due to the use of an liquid crystal device as electronical shutter, the upper wavelength range is limited to 700 nm. Furthermore, the time resolution is only in the range of several seconds.

Arpad Jakab built a setup that uses a variant of the spectral imaging method. Spectra are collected along a one dimensional line (the entrance slit of an imaging spectrometer) and the sample is moved relative to this line.[80] His setup could measure up to 900 nm. However, since he was scanning the whole sample in small steps, the acquisition was very time consuming. Furthermore, the position relative to the entrance slit was not controlled neither was the focus. A third method, which was not used on our setups so far, is to collect spectra of a central point on the optical axis and to scan the sample either manually or

computer controlled.[15] Finally, another variant of the spectral imaging could be used to acquire spectra. One could take monochromatic images of the whole sample and scan the excitation or collection wavelength.[81]

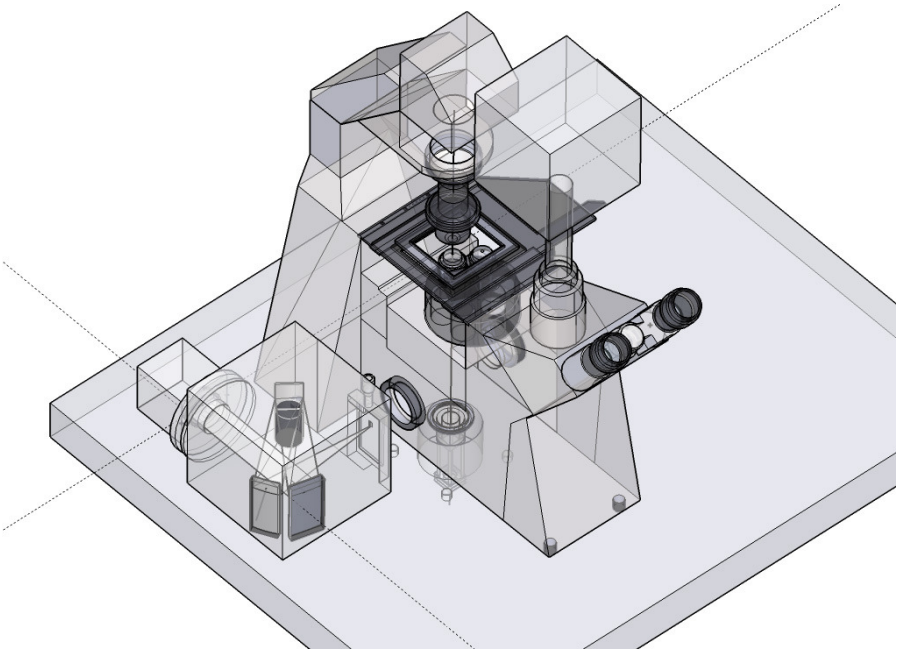

Figure 9.1: 3D-model of my microscope and its major components that I made using SketchUp 8. The beam path in the spectrograph is just examplatory, the true beam path might look different.

All the previous setups in the group were upright microscopes. I introduced an inverted microscope as a new generation of setup to our group (until now there are 3 clones of my setup). The measurement principle is the collection of spectra along a one dimensional line. But compared to Arpad's method, I use the image information and move directly to the recognized particles, refine the position in the slit as well as the focus before I acquire a spectrum. This pushed both the speed and the precision of our measurements. Now, we can acquire about 10 to 20 particles/minute and have an approximately 5 times smaller standard deviation in repeated measurements. Therefore, my method for acquisiton of UV-VIS-spectra is at the moment state-of-the-art in our group. Besides this, I built an IR-spectrometer with polarization filter at my setup as well that allows us to investigate particles in the wavelength range of 900 nm to 1700 nm including polarization dependency.

In the following sections, I elaborate the design of my setup for the UV-VIS to NIR region as well as the IR region. I present the characteristics of the components that I used, like the EM-CCD, the piezostage, etc. Additionally, I show simulations of the measurements that can be used to predict the noise level of these setups or whether the detection of an event will be possible for certain parameters at all.

FUNCTION NAME	CALLS	TOTAL TIME / S
ScanParticles	1	307
RefinePosition	80	156

Table 9.1: Speed test of the function *ScanParticles()* using the MATLAB -profiler. 80 particles were scanned with an exposure time of 0.1 s and 3 averages. On average 307 s / 80 ≈ 3.8 s are needed to refine the particle position and to acquire and save a spectrum.

9.1 VIS TO NIR (450 nm TO 900 nm)

9.1.1 *System Design*

As already mentioned, the setup was planned to increase speed as well as precision of the acquisition of single particle spectra using a scanning routine. For this, I equipped a Zeiss Axio Observer D1 inverted microscope with a PI542 XY-piezo stage (200 µmx200 µm, closed-loop) and a PI721 Z-piezo (100 µm, closed-loop). Furthermore, for VIS-NIR-spectroscopy, I added an Imspector V10E transmissive imaging spectrograph with an Andor iXon888 EM-CCD. The true color images are taken with a Canon EOS 5D Mark II (IR-filter has been removed). For the aquisition and analysis of single particle spectra, I wrote a software package using MATLAB that I called the "Nanocenter". It provides an easy to use interface to control the microscope components like camera or stage and has routines for automated measurements. Since the particle positions are saved, the spectra can be acquired repeatably, which is the basic requirement for experiments where the surrounding of the particles is altered. Furthermore, particles that have a corrupt spectrum or are simply lost due to the exchange of solutions can be sorted out, which speeds up the subsequent measurements. In principle a measurement consists of 3 steps:

1. Acquisiton of a true color image.
2. Recognition of the bright spots in the image.
3. Acquisition of spectra of each bright spot including automated position refinement in X-position and Z-position (autofocus).

The conversion of positions in the true color image into stage to slit movements is done internally and is based on an affine transformation routine readily provided in the image processing toolbox of MATLAB . The refinement typically consists of 7 sampling points for X-position- and 11 sampling points for Z-position-refinement. I measured the speed of the core scanning routine *ScanParticles()* using the MATLAB profiler and the results are shown in Table 9.1 — roughly 3.8 s are needed to refine the particle position and acquire and save a spectrum in case of 0.1 s exposure time, 3 averages and a reasonable set of refinement parameters. For a further understanding of the performance of my setup the characteristics of the major components (Figure 9.2) — the piezos and the EM-CCD — have to be discussed.

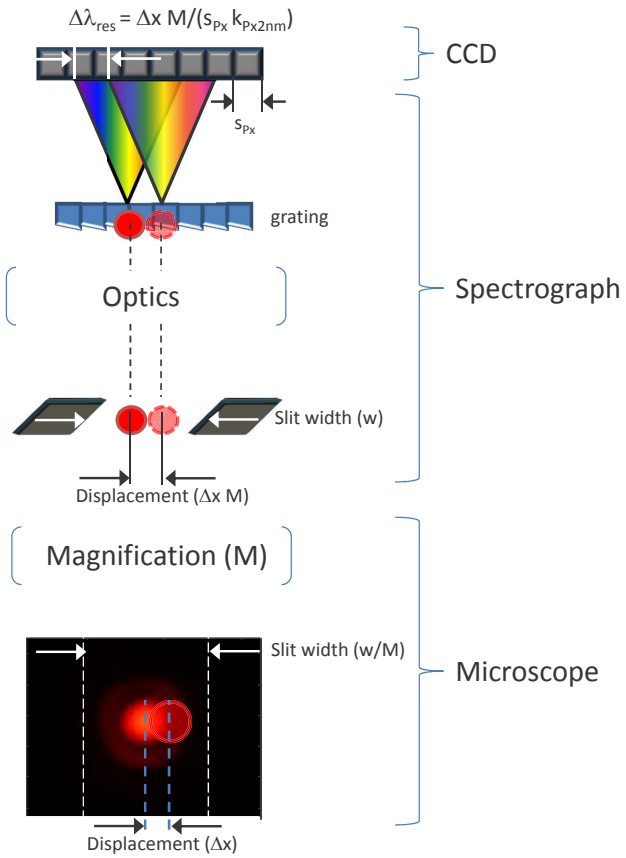

Figure 9.2: Scheme of the spectra acquisition and problems that introduce variations in the spectral information. A displacement of an object by Δx from the optimal position produces an apparent spectral shift $\Delta\lambda$ depending on the magnitude of the displacement Δx, the magnification M as well as the size of the pixels s_{px} on the CCD and the spectral resolution k_{px2nm}. Not shown in the scheme but varying the focus also varies the measured spectra of the particle depending on the magnitude of the displacement Δz due to chromaticity.

PIEZOS. For the characterization of the piezos, I performed 500 repeated movements of 1.5 µm of the XY-stage since this is a typical step size after the refinement and read out the position of the internal position sensor of the stage. The same, I did for the Z-piezo where the typical step size is 0.5 µm. The results are shown in Figure 9.3. The standard deviation for the positioning is 2 nm for both X- and Z-piezos. The accuracy of the stage is important since it directly influences the wavelength scale of the spectra as depicted in Figure 9.2. Since the camera and the spectrograph are static a displacement Δx parallel to the dispersion direction of the grating will result in a spectral shift $\Delta\lambda$. The magnitude of $\Delta\lambda$ is determined by the magnitude of Δx, the magnification M as well as the size of the pixels s_{px} of the CCD and the spectral dispersion k_{px2nm},

$$\Delta\lambda_{\text{res}} = \frac{\Delta x M}{s_{\text{px}} k_{\text{px2nm}}}. \tag{9.1}$$

A similar reasoning holds for a displacement in z, i. e. a malfocus. Here, a theoretic description is difficult since the chromatic effects that lead to a spectral shift as function of focus are dependent on the objective that is used. Therefore, I measured the effect of displacement Δz on the resonance wavelength directly. For my objective (Zeiss Plan-Apochromat 100x oil iris) this dependency can be described as a 2^{nd} order polynomial 1.2 µm around the local minimum of optimal focus (Figure 9.3c).

Using $\Delta x = 2\,\text{nm}$, $M = 100$, $s_{\text{px}} = 13\,\mu\text{m}$, and $k_{\text{px2nm}} = 1.2\,\text{nm}$, I obtain $\Delta\lambda_{\text{res}} = 0.13\,\text{nm}$ for my setup — neglecting noise contributed by the displacement Δz or the EM-CCD. The noise contributed by the displacement Δx could be reduced using a smaller magnification, a larger pixel size or a grating with larger spectral dispersion. For $M = 40$, $\Delta\lambda_{\text{res}}$ would already reduce to 0.06 nm. To reduce $\Delta\lambda_{\text{res}}$ down to 0.01 nm, M would have to be reduced further to 20, s_{px} would have to be increased to 16 µm, and k_{px2nm} would have to be increased to 2.4 nm for example.

EM-CCD. The second part is the EM-CCD. An EM-CCD is an electron multiplying CCD, i. e. there are several registers that act as gain registers to amplify the signal. As usual for cameras, the signal is presented as ADU, which can be converted to electron flux $e\,\text{s}^{-1}$ or photon flux Φ_{p} using the system gain of the camera and the quantum efficiency, respectively. The amplification of the signal depends on the actual electron multiplier gain and the number of gain registers (Equation 9.5). The dynamic range (DR) of EM-CCDs is influenced by the applied EM-gain and the readout speed and the DR decreases when the EM-gain is chosen too high. We use our cameras at the fastest readout speeds and low to medium EM-gain levels. Therefore, the noise performance is the important information to be discussed in greater detail, i. e. the dark noise, the read noise, and the shot noise. [1]

The **dark noise** n_{dark} is thought to be neglectable for cooled CCD-cameras. To be certain about this, I measured the dark noise for temperatures from −80 °C to 20 °C. The data is shown in Figure A.2 and Figure A.1 both in Appendix A. Below −20 °C, the noise level is smaller than 1 e/(px s) already. Furthermore, my camera is cooled to −80 °C and the exposure times are smaller 1 s — usually around 0.1 s. Therefore, dark noise can be indeed neglected.

The **read noise** n_{read} is typically very small for an EM-CCD but it is gain-dependent. Hence, I measured the read noise for gains between 0 and 200 (Figure 9.4a), which is the standard deviation of the signal per pixel. In ADU as function of EM-gain M, a 2^{nd} order polynomial fit results

$$n_{\text{read}}(M) = 2.456 \cdot 10^{-5} M^2 + 1.014 \cdot 10^{-3} M + 2.868. \tag{9.2}$$

Using the measured system gain[2] of the camera, the read out noise can be converted to e/(px s) (Figure 9.4b). At EM-gain of 25 the read noise

1 I generated a function *CCDcharactize.m* for Nanocenter that can automatcally acquire data about read noise, dark noise and system gain.

2 The system gain can be estimated from the slope of the variance as function of signal.

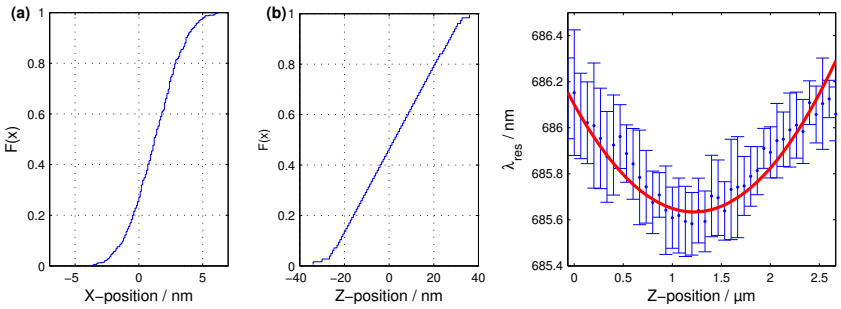

Figure 9.3: (a) and (b) Accuracy of positioning in x and z. The standard deviation is 2 nm in x and 13 nm in z. (c) Resonance wavelength as function of focus. The errorbars are obtained by taking the standard deviation of 5 consecutive measurements. The data is fit with a 2nd order polynomial ±1.2 µm around the local minimum at ≈1.3 µm ($\chi^2_{\text{red}} \approx 0.28$).

goes down to 1 e/(px s) already - so its contribution is very small. In general, the higher the EM-gain the lower the read noise contribution.

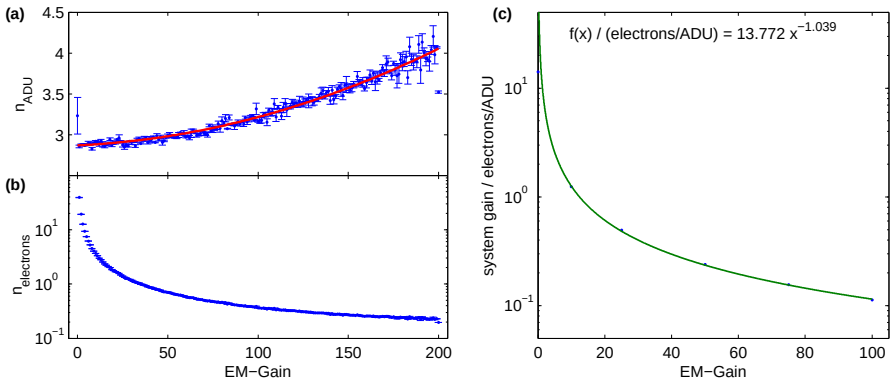

Figure 9.4: Characteristics of the iXon888 (a) Read noise as measured in ADU for different gains from 0 to 200. (b) The data in (a) converted to noise in electrons using the EM-Gain dependent system gain. (c) System gain measured (dots) and approximated (line) using a power law.

Finally, there is **shot noise** n_{shot}. This noise is a fundamental property of light and can be described by poissonian statistics. For CCDs, the shot noise only depends on the photon flux Φ_p, the quantum efficiency η, and the exposure time t_{exp}.

$$n_{\text{shot}} = \sqrt{\Phi_p \eta t_{\text{exp}}} \tag{9.3}$$

In the case of intensified cameras like an EM-CCD two more factors have to be introduced - the system gain G, and the excess noise factor F - and Equation 9.3 changes to

$$n_{\text{shot}} = GF\sqrt{\Phi_p \eta t_{\text{exp}}} \tag{9.4}$$

The excess noise factor F for an EM-CCD depends on the EM-gain M and the number of gain registers N_g present in the camera and has been measured and described theoretically[82]

$$F^2 = 2(M-1)M^{-(N_g+1)/N_g} + \frac{1}{M} \tag{9.5}$$

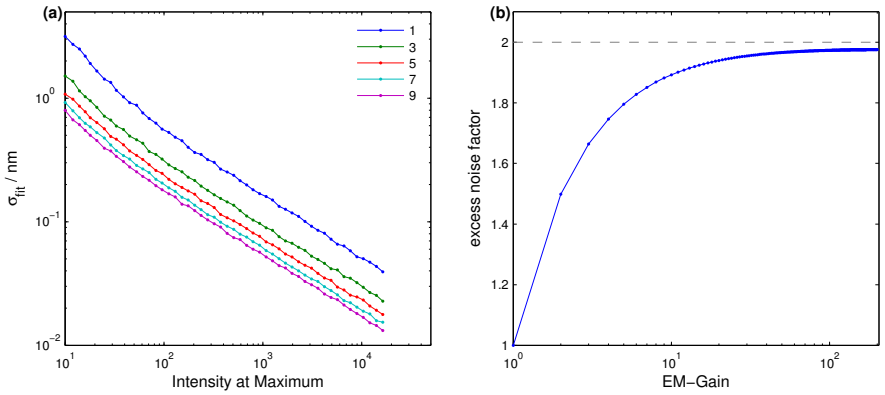

Figure 9.5: (a) Influence of intensity and averaging on the variation in fit accuracy using a Lorentzian function. Clearly, the lowest standard deviation is at highest signal levels and maximum of averages. (b) Excess noise factor as a function of EM-Gain. At an EM-Gain of about 25 the excess noise factor is already close to its maximum of 2.

Figure 9.5b shows F as function of EM-gain. At an EM-gain of about 25, F^2 is already close to its maximum value of 2. Hence, in typical situations, where the EM-gain is around 50, the shot noise of an EM-CCD is a factor of $\sqrt{2}$ higher than in a conventional CCD.

Additionally, and somehow related to the camera is the task of extracting the parameters $\Delta\lambda$ and FWHM of the spectrum. The easiest and most error-prone method is to simply read of the maximum and the FWHM. Of course, the better way is to use an appropriate model and fit the spectrum. This will also improve the resolution because there are usually enough sampling points available. Since plasmons are damped driven oscillators, a Lorentzian function is usually a good choice for the description of dipolar oscillations. Using this function, I performed a Monte Carlo simulation to estimate the influence of the intensity of the spectra using simulated time traces of 2000 spectra in the shot noise limit ($\sqrt{2N}$ only) and the resolution of 1.2 nm/px of my setup. Furthermore, I performed this simulation for different amount of averaging. The resulting fitting noise[3] σ_{fit} as function of the maximum intensity N_{max} is shown in Figure 9.5a.

For intensities larger 100 ADU, it is a linear function of the maximum intensity in a loglog-space and increasing the amount of averaged spectra decreases σ_{fit} as intuitively expected. For a typical intensity of 5000 ADU and 3 averages, the noise is 0.04 nm. Increasing the intensity increases therefore the spectral resolution because it increases the signal to noise ratio $N/\sqrt{2N} = \sqrt{N/2}$. Additionally, increasing the resolution of the spectrometer can increase the spectral resolution as well because it increases the number of sampling points. Note, that the σ_{fit} as function of maximum intensity is actually the transformation of intensity noise to spectral noise (albeit the noise of the EM-CCD and the error of the fit cannot really be seperated). The spectral noise is usually very important when time traces

3 The fitting noise is estimated as the standard deviation of the resonance positions of the 2000 spectra, $\sigma_{\text{fit}} = \sqrt{\frac{1}{n-1}\sum_{i=1}^{n} s(\lambda_{\text{res,i}} - \overline{\lambda_{\text{res}}})^2}$.

shall be recorded and small step-like events shall be resolved like in Chapter 12.

9.1.2 *Simulation*

With all the knowledge presented in Section 9.1.1, it is now possible to simulate the spectra acquistion. Only a few additional information is needed, i.e. the amount of light at the sample plane (see APPENDIX) and the numerical aperture of the objective, which is typically between 0.6 and 0.8 in my case. I implemented set of functions with the parental function *SimEnsemble()* that takes a struct containing all information about the stage, the camera, and the simulated particles and virtually performs a measurement.

Before I finally show a comparison of a real experiment along with a simulation using the same parameters that were used in the experiment, I will first present the details of a measurement — especially the refinement process - and how these are implemented for simulation. As stated in Section 9.1.1, the particles are recognized using image processing routines and their coordinates in the true color image are transformed into stage to slit movements first. After that, a refinement in the X-position and Z-position takes place before finally the spectra are acquired. The important points for the simulation are the process of position refinement and spectra acquistion.

As for the spectra acquisition, I use two sets of exposure times and EM-gains. For the refinement process, I use exposure times around 25 ms and an EM-gain of about 150. In the final spectra acquisition, the exposure time is around 100 ms and the EM-gain about 50. Using the data shown in Figure 9.4 and Equation 9.5 the noise of the spectra can be simulated for any set of exposure times and EM-gains. The particle spectra are simulated using QSA.

QSA provides the scattering cross-section as function of wavelength $\sigma_{\mathrm{sca}}(\lambda)$.[4] This has to be converted into a photon flux $\Phi_{\mathrm{e,cam}}$ at the camera using the quantum efficiencies of the grating and the camera,

$$\Phi_{\mathrm{e,corr}}/(e/(\mathrm{px\ nm^2 s})) = \Phi_{\mathrm{p,In}}\frac{\lambda}{hc}\eta_{\mathrm{grating}}\eta_{\mathrm{QY}}s_{\mathrm{px}} \tag{9.6}$$

Actually, the photon flux $\Phi_{\mathrm{p,In}}$ is a flux per wavelength because I have to take the pixel size into account. With this I obtain a photon flux at the camera of about $0.4\,e/(\mathrm{px\ nm^2 s})$ to $1.8\,e/(\mathrm{px\ nm^2 s})$. Using

$$\Phi_{\mathrm{e,cam}} = \Phi_{\mathrm{e,corr}}\sigma_{\mathrm{sca}}(\lambda), \tag{9.7}$$

I finally obtain the $e/(\mathrm{px\ s})$ at the camera. At this point, all processes controlled by the camera have to be considered, i. e. the exposure time t_{exp}, the EM-gain M, the system gain[5] G and the electronical background offset I_{offset}, which yields

$$I_{\mathrm{cam}}/ADU = \Phi_{\mathrm{e,cam}}t_{\mathrm{exp}}MG + I_{\mathrm{offset}}. \tag{9.8}$$

4 $[\sigma_{\mathrm{sca}}(\lambda)] = \mathrm{nm}^2$
5 $[G] = e/ADU$

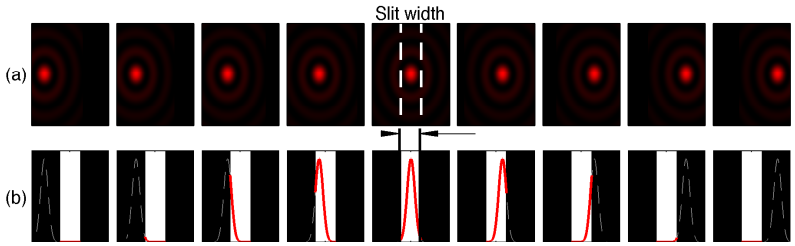

Figure 9.6: Calculated movement of a particle under slit. (a) Simulated image. (b) Intensity profiles inside the slit as function of particle position.

I_{offset} is used by the manufactorer to avoid negative voltage at the analog to digital converter (ADC). Using Equation 9.4 and Equation 9.5, the shot noise is added before the system gain is taken into account and the background offset is added in Equation 9.8 since the system gain resembles the amplification done by the ADC. The read noise is added afterwards and the dark noise is neglected as explained in Section 9.1.1.

For the refinement process the actual spectra are not needed but rather the intensity as a function of position, that is to say the zeroth order diffraction. Since the Imspector is a fixed transmission grating only the first order diffraction is available. To obtain the intensity information I sum the CCD images in their spectral direction. After obtaining this pseudo-image of the sample I fit the intensity profile with a gaussian function to get the optimal position in the center of the slit. The same I do for the refinement in the Z-direction although there it's not the center of the slit but the position of the optimal focus.

In the simulation, I approximate the diffraction limited spot produced by the particle by a gaussian function neglecting the higher order peaks of the Bessel-function (diffraction of a pinhole). For the refinement in X-position I virtually move the particle under a slit of the appropriate size (800 nm in the sample plane) and sum the intensity of the part of the spot that falls within the slit (Figure 9.6). Then I use the spectrum of the particle and multiply it by the fraction of the spot inside the slit, calculate the noise and sum the spectrum for each X-position. This yields the intensity as function of X-position, which can be fitted with a gaussian function and an apparently optimal X-position can be obtained.

In the next step, the Z-position is refined. Here, the simulation is slightly more complicated. For the refinement of the Z-position virtually two slits have to be considered - the real slit of the spectrometer and the virtual slit, which is the depth of field (DOF) of the objective.

$$\text{DOF}/\mu\text{m} = \frac{1000}{7A_{\text{objective}}M} + \frac{\lambda}{2A^2_{\text{objective}}} \tag{9.9}$$

As approximation for λ I use the resonance wavelength of the simulated spectrum. The change of the diameter of the diffraction limited

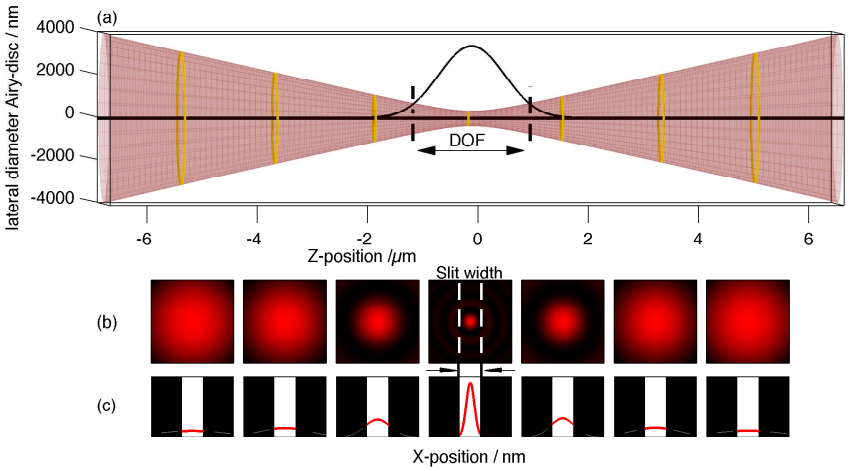

Figure 9.7: Calculation of the diameter of the Airy-disc as function of focus. The Z-Airy-disc as well as the depth of field (DOF) is shown. The yellow lines show the positions of the computed images and intensity profiles. The images show the intuitive trend of image blurring when moving out of focus.

spot as function of Z-position I approximated using the gaussian beam propagation

$$w(z) = w_0 \left[1 + \left(\frac{\lambda z}{\pi w_0^2} \right)^2 \right]^{1/2}, \tag{9.10}$$

where, w_0 is the diameter of the diffraction limited spot in focus, which is about 700 nm as measured in my microscope. For the axial direction I approximated the on axis intensity profile with an gaussian beam that has a width of twice the diameter of the lateral diffraction limited spot. Changing the Z-position changes the radius of the spot in the image (Figure 9.7a and b). In principle, it is the same as cutting a double cone at different heights parallel to its bases. The intensity of the spot is defined by the amount of light within the DOF of the objective. Considering both radius and intensity, I obtain the intensity profiles for the diffraction limited spot shown in Figure 9.7c yielding the intensity seen by the spectrometer as function of Z-position when applied to the spectrum of the particle as explained for the X-position refinement. As mentioned above, the optimal focus is found by fitting a gaussian function to this intensity profile. Using the function of λ_{res} as function of Z-position (Figure 9.3) the change of λ_{res} is obtained.

For both of these refinement processes the position noise as shown in Figure 9.3a and b is used. Additionally, I use an offset noise of 250 nm for X and 100 nm for Z to account for unsystematic effects like drifts in the sample.

To show the accuracy of this simulation, I performed a sensitivity measurement changing the refractive index around gold nanorods using glycerol several times. The cumulative distributions of the measured shifts are shown in Figure 9.8a. It can be seen that the distribution gets broader when the shifts get bigger, which is partially caused by the differing sensitivities of each particle as explained in Chapter 10. In Figure 9.8b the results of the simulation are shown.

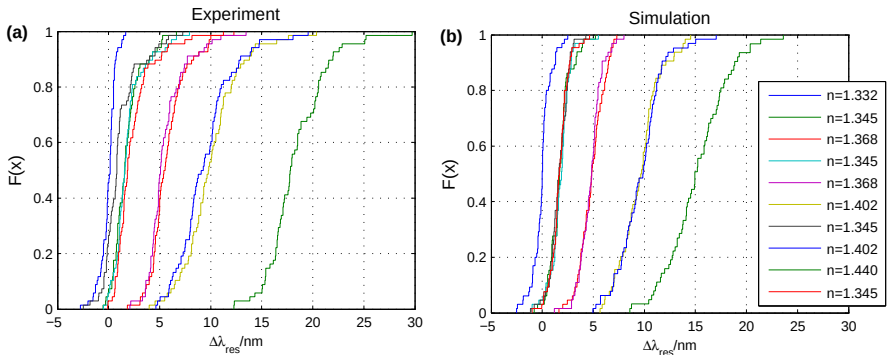

Figure 9.8: (a) Measuring the shift of 68 gold nanorods changing the refractive index with glycerol/water mixtures. (b) Same data but simulated with the parameters used in the real experiment. The average shifts and standard deviations are given in Table 9.2

Qualitatively, the simulation looks very similar to the experiment and comparing the values for average shift and distribution width it also agrees well quantitively (compare Table 9.2. Overall, there seems to be a slight underestimation of the distribution width, which can be explained by changes on the particle surface or imperfect solvent exchange that are hard or very speculative to simulate.

Furthermore, I implemented the evaluation of the individual noise contributions for each particle in the simulation since these are key parameters for optimizing the measurements. The noise contributions for one run and the average contributions over all runs of the simulated measurement are shown in Figure 9.9a and b, respectively.

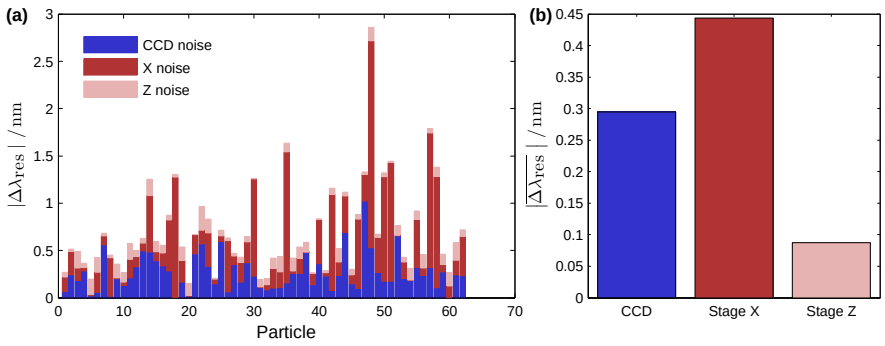

Figure 9.9: (a) Noise contributions of misplacement in X and Z as well as CCD noise. For each particle the individual noise contributions are shown. (b) The average of each noise contribution.

Note that the presented comparison in Table 9.2 is done with one examplatory simulation and the values may change from simulation to simulation since it is a Monte Carlo type simulation albeit the variation is very small, which can be seen comparing the values of the repeats for the same refractive index.

The good agreement of the simulation with real measurements shows that this can be used to choose the optimal parameters for an experiment in advance. For instance, the parameters for the shown measurements were chosen for a good compromise of speed and precision but using a finer sampling in the X-position refinement will lower

Refractice Index	Experiment /nm		Simulation /nm		Difference /nm	
n	$\Delta\lambda_{res}$	$\sigma_{\Delta\lambda_{res}}$	$\Delta\lambda_{res}$	$\sigma_{\Delta\lambda_{res}}$	$\lvert\Delta\lambda_{res}\rvert$	$\lvert\Delta\sigma_{\Delta\lambda_{res}}\rvert$
1.332	0.14	0.61	0.00	0.56	0.14	0.05
1.345	1.60	1.07	1.69	0.86	0.09	0.21
1.368	5.48	1.45	4.82	1.24	0.66	0.21
1.345	1.57	0.86	1.89	0.77	0.32	0.09
1.368	5.09	1.21	4.82	1.00	0.27	0.21
1.402	9.79	2.21	9.68	1.71	0.11	0.50
1.345	0.80	1.34	1.62	0.90	0.82	0.44
1.402	9.17	2.13	9.86	1.89	0.71	0.24
1.440	17.81	2.71	14.95	2.92	2.14	0.21
1.345	1.85	1.31	1.66	0.63	0.19	0.68

Table 9.2: Measured and simulated shifts and shift distributions for the experiment shown in Figure 9.8. On average the measured and simulated $\Delta\lambda_{res}$ and $\sigma_{\Delta\lambda_{res}}$ agree well within 11% and 16%, respectively.

the noise, hence, increase the precision on the resonance wavelength on the cost of speed. Also the number of averages could be increased to reduce the CCD-noise (since the intensity in the experiment was already high there is little room for increasing the exposure time). Since my setup has been cloned, this simulation can be used for the other setups as well as soon as the setup characteristics like camera noise and stage noise are known.

Clearly, when it comes to sensing experiments not only the performance of a particle in the setup has to be evaluated but the suitability of that sensor for sensing a certain molecule has to be taken into account as well. Calculations in that respect have been done the single unlabeled detection of proteins and are shown in Chapter 12.

9.2 MIDIR (900 nm TO 1700 nm)

For IR-spectroscopy, I added an Acton SP-2156 reflective spectrograph (Grating: 85 l/mm, 1.35 µm Blaze) with a Xenics Xeva-Lin-2.5 InGaAs detector for IR-spectroscopy at one side port of the microscope (Figure 9.1). Furthermore, I placed a rotational stage with a suitable polarisation filter (both Thorlabs) in front of the spectrograph, which allowed me to collect polarisation-dependent spectra of triangular particles lithographically produced by the group of Prof. Gießen (see Chapter 11). Further characterization of this camera and spectrometer has not be done yet but is planned for the future when particles for sensing experiments in the IR are readily available. A synthesis protocol for nanoparticles with reasonable volume to provide enough intensity is not yet available in our group.

10

SIZE VARIATION ACCOUNTS FOR ONE THIRD OF INTERPARTICLE VARIATION IN PLASMONIC SENSITIVITY OF GOLD NANORODS

10.1 INTRODUCTION

PLASMONIC nanoparticles change their resonance wavelenth λ_{res} by $\Delta\lambda$ upon refractive index changes Δn in their local environment, the sensing volume. This effect provides an attractive optical method for label-free nano-sensing in molecular dimensions. Changing the nano-particle geometry allows to optimize their plasmonic sensitivity $S = \Delta\lambda/\Delta n$ to a large degree.[83,84,85] By optimizing the trade-off of plasmonic sensitivity and noise level, even single molecule detection was recently demonstrated.[86,87]

Since plasmonic sensitivity, sensing volume, and the signal to noise ratio strongly depend on the nano-particle size, precise information on the nano-sensor geometry and size is required for precision measurements. At least for nanoparticles produced by wet-chemical synthesis (crystallization from solution), the variation in nanoparticle size within one batch is usually quite significant (above 10%) and size selective purification methods are not yet routinely applicable for nanoparticles.

Transmission electron microscopy is the most commonly used technique for nano-particle size and shape characterization. In mos cases, only mean values are determined from the same batch as gathering correlated spectroscopic and TEM information of the exact same particle is a challenging and time-consuming task usually bound to low statistics.[88,89] There is therefore the strong need to know the exact nanoparticle size for each individual nanoparticle that is used for an optical sensing experiment.

In this chapter, I show how to estimate the size of gold nano-rods directly from the plasmon linewidth measured from optical spectra utilizing the well-known increase of radiation damping with nanoparticle size.[15] I verify this approach by collecting high-resolution scanning electron microscopy (SEM) images of the same particles (Figure 10.1a, b) and obtain an agreement within the SEM accuracy (< 10%). I then apply this approach to reduce the distribution (between particles) of the measured plasmonic sensitivity S by 30% by correcting for the systematic error introduced from the variation in particle size.

10.2 RESULTS AND DISCUSSION

For the extraction of the nanorod dimensions, I first need to know the spectral properties of differently sized particles. Therefore, I used the

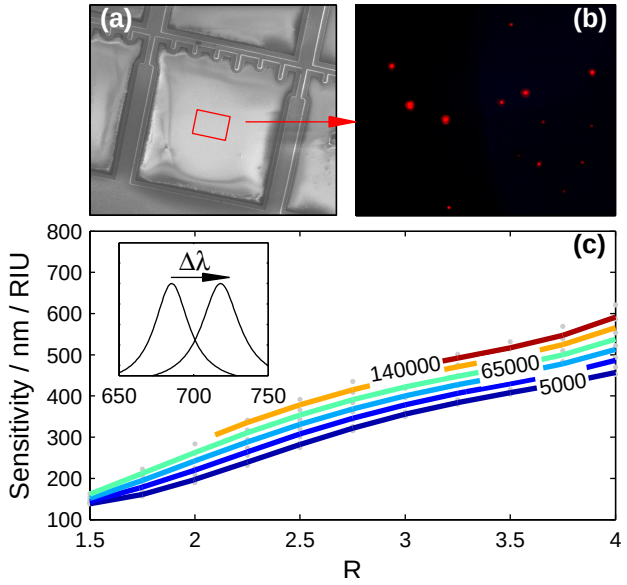

Figure 10.1: (a) SEM overview image containing the measured area in the dark-field microscope shown in (b). (c) Showing sensitivity as a function of aspect ratio AR. The lines are sensitivity at constant volume in nm^3. The inset shows symbolically the change of the plasmonic resonance due to a change of the refractive index corresponding to Equation 10.2.

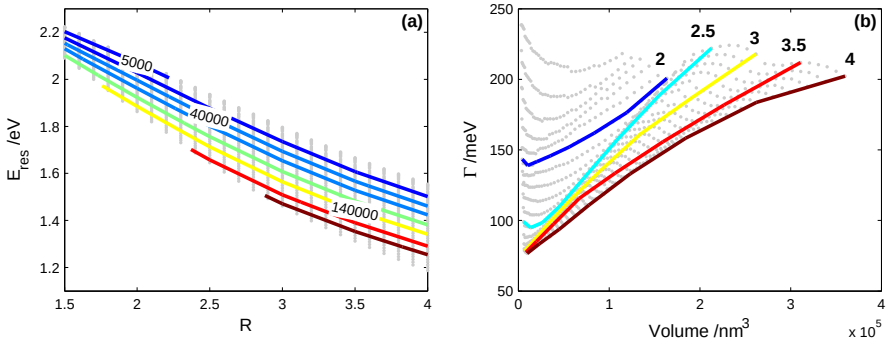

Figure 10.2: Showing E_{res} and Γ, σ_{sca} as functions of aspect ratio and volume, respectively, as obtained from BEM simulations. Lines show levels of (a) constant volume or (b) constant aspect ratio.

boundary element method MNPBEM toolbox [14] to simulate the scattering cross sections σ_{sca} of hemispherically capped gold cylinders (gold nanorods) with diameters D from 15 nm to 50 nm in steps of 1 nm and aspect ratios $AR = L/D$ from 1.5 to 4 in steps of 0.1 using tabulated optical constants for gold. [10] The resonance energy E_{res}, Full-Width-at-Half-Maximum Γ and the maximum scattering cross section σ_{max} for each of the simulated spectra were extracted using the Lorentzian function

$$\sigma_{sca}(E) = \sigma_{max} \frac{\Gamma^2}{4(E - E_{res})^2 + \Gamma^2}. \tag{10.1}$$

Furthermore, the refractive index of the surrounding medium was changed from $n_1 = 1.33$ (water) to $n_2 = 1.40$ and the simulation was

carried out for the same range, but in steps of 5 nm for D and steps of 0.25 for AR. This yielded the bulk sensitivity

$$S = \frac{\lambda_{\mathrm{res}}(n_1) - \lambda_{\mathrm{res}}(n_2)}{n_1 - n_2} \equiv \frac{\Delta\lambda}{\Delta n} \tag{10.2}$$

of each simulated rod, where $\lambda_{\mathrm{res}} = \hbar c / E_{\mathrm{res}}$. Next, the quantities D, AR as discretized functions of E_{res} and Γ and S as discretized functions of D and AR were interpolated by performing a surface fit with a 5^{th} order polynomial (equations and coefficients in Appendix B). The interpolation embodies the results of the time-consuming BEM simulations in compact polynoms. The relative error introduced by this interpolation is less than 5 % for D, less than 3 % for AR and less than 2 % for S, which is neglegible compared to the experimental errors outlined below.

Figure 10.1 and Figure 10.2 depict the results for the sensitivity and the particle dimensions, respectively. E_{res} as function of AR shows the expected almost hyperbolic dependency.[12] In contrast to a quasi-static calculation, a significant change in E_{res} is observed not only for an increase in AR but also for an increase in particle volume (Figure 10.2a). Hence, for a fixed E_{res}, AR varies as much as ± 1. In case of Γ as function of volume (Figure 10.2b), I observe nearly linear dependencies for constant AR.

By extracting E_{res} and Γ from a nanorod spectrum its dimensions are uniquely determined. Note, that the absolute scattering intensity is not necessary to extract the sizes, which renders the method easy-to-use at optical dark-field microscopes, where the determination of absolute intensities is difficult as the excitation light does not enter the detection path and the exact illumination intensity varies by orders of magnitude from day to day due to slight condensor focus variations.

In order to validate the size determination by this simulation approach, the scattering spectra of 32 gold nanorods were measured in a dark-field microscope. All single particle scattering spectra were taken at a Zeiss Axio Observer D1 equipped with an Piezostage PI542 and a Z-Piezo PIFOC-721. The spectra were aquired using an ImSpector V10E and an Andor EMCCD. A home-built MATLAB™software was used for acquisition. Exposure times were in the range of 100 ms to 250 ms with an electron multiplying gain set to 50. The particles were automatically centered at the slit of the spectrometer as well as focused by optimizing the intensity.

The nanorods were synthesized in a standard wet-chemical process[36], immobilized on a glass substrate equipped with a binary labeled grid using sodium chloride in situ. Spectra were acquired after flushing with deionized water. Next, the particles were identified again in the scanning electron microscope (SEM) Nova NanoSem 600 using the features on the grid.The SEM images were evaluated manually to extract the particle dimensions.

This way, a correlation of the direct size determination using SEM and the indirect determination using my approach was successfully achieved. Three examplatory nanorods with their SEM image and their scattering spectrum as well as the overall result are shown in

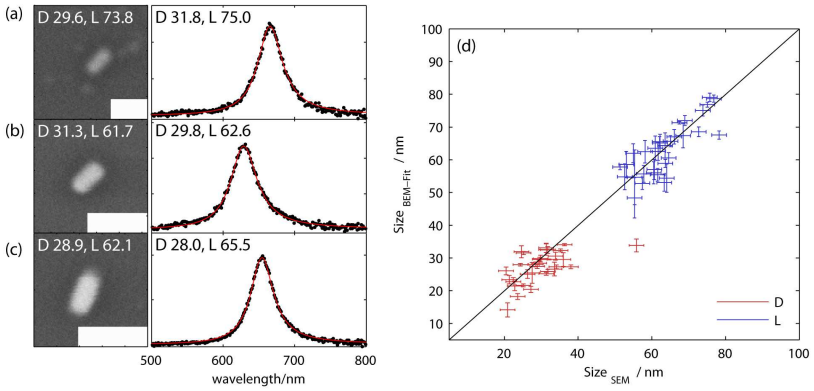

Figure 10.3: Correlation of diameter D and length L of the same particles as estimated with BEM simulations (y-axes) and SEM measurements (x-axes). The sizes scatter around the expected bisecting line (black) with $\chi^2_{\text{red}} \approx 4.3$.

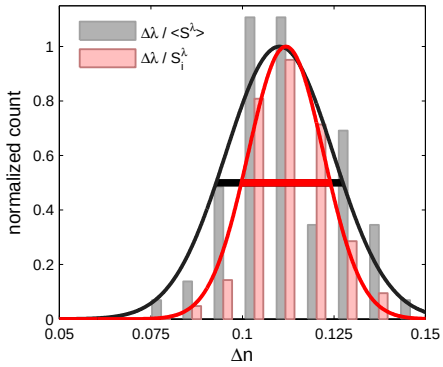

Figure 10.4: $\Delta\lambda_{\text{res}}$ mapped to Δn-space using the size information and furthermore the sensitivity information simulated in BEM. Calculating with individual sensitivities leads to a 30% narrower distribution and a slight shift in maximum position.

Figure 10.3. I calculated the errors for the size determination using BEM by error propagation, e. g.

$$\Delta D_{\text{BEM}} = \sqrt{\left(\frac{\partial D}{\partial E_{\text{res}}}\Delta E_{\text{res}}\right)^2 + \left(\frac{\partial D}{\partial \Gamma}\Delta\Gamma\right)^2}, \tag{10.3}$$

using the parameter errors ΔE_{res} and $\Delta\Gamma$ from the Lorentz fit of the measured spectra according to Equation 10.1 and the function $D(E_{\text{res}},\Gamma)$ from Equation B.1. The sizes scatter around the expected bisecting line. Using $\sigma_i = 2\,\text{nm}$ for x_i, I obtain $\chi^2_{\text{red}} \approx 4.3$.

As shown in Figure 10.1, the sensitivity varies strongly for different sizes of nanorods. Up to now, many particles are measured in solutions of different refractive indices and their shifts are averaged to calculate the response neglecting the different sensitivities. My method overcomes this approximation as shown below.

To proof the applicability of my method, I performed a typical bulk sensitivity measurement. I measured the resonance wavelength of single nanorods in water ($n = 1.332$) and glycerol ($n = 1.44$). The sensitivities of the particles were calculated using the sizes determined by our approach. Compared to the usual averaging over all of the particles, I

can now use their individual sensitivity. I transformed our single particle shifts to Δn-space using Equation 10.2 and achieved a narrowing of the distribution in Δn by about 30% compared to averaged sensitivities (Figure 10.4). Note, that the median is slightly shifted as well, which might point at a systematical error in estimating the averaged sensitivities.

In theory, I expect a sharply peaked distribution but several reasons may cause the remaining distribution width. A few minor reasons can be measurement uncertainty, non-rod-shaped particles having similar spectra or rods with different endcap structures.[12] One major issue could be the contamination of the rods by molecules present in the solutions, which would alter the expected shift upon refractive index changes. This will be investigated in future work. Though, my method can reduce the distribution its strength lies within the quantitative determination of absolute rod dimensions and the online selection of appropriate particles without the need for an electron microscope. Furthermore, knowing the size of the individual particles in an experiment is mandatory to interpret a certain shift, for instance caused by target molecules in a sensing application. For single molecule experiments,[86] it is beneficial to select the best particle in advance instead of a doing a correlation using TEM or SEM.

In summary, I demonstrate that it is possible to extract the dimensions of hemispherically capped nanorods from optical scattering spectra using E_{res} and Γ in combination with BEM simulations. This technique provides a reasonable accuracy of 10% in average and allows for the online optimization of single particle sensing experiments and improvement of single particle sensitivity measurements.

11

POLARIZATION-DEPENDENCE OF BOWTIE STRUCTURES

FOR a cooperation with the group of Prof. Gießen from Stuttgart, I investigated the single particle scattering of Bowtie structures. These structures consist of two (mostly) equilateral triangles pointing one tip at each other (compare Figure 11.1). They may be used in sensing applications due to the hot spot that these structures exhibit. Depending on the gap between them, the strength of the hot spot, i.e.a volume of large field enhancement, will change and there will be a shift in resonance position.[90,91] This shift in resonance position of the longitudinal mode has been measured in the group of Prof. Gießen by transmission spectroscopy on fields of similar structures and varying gap distances (compare Figure 11.1). My task was the verification of the observed effects on single structures.

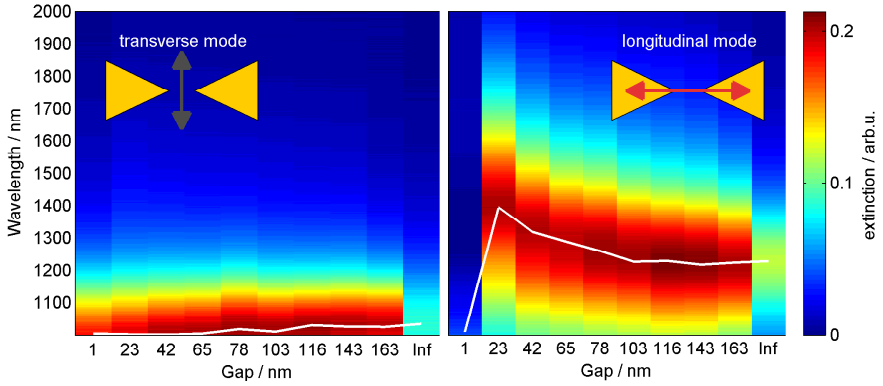

Figure 11.1: Transmission measurements of fields of Bowties of the same shape (measurements were performed by the group of Prof. Gießen). The transverse plasmon mode changes only little by changing the gap between both the triangles but the longitudinal mode changes the resonance position significantly by about 150 nm. The gap 'Inf' corresponds to a single triangle, which should be similar to two triangles seperated by very large gap.

For this, I acquired scattering spectra of 9 structures with different gaps and a single triangle using the setup described in Section 9.2. I used the polarization filter to acquire their polarization depend spectra in 10° resolution.The exposure times were in the range of 200 ms. Furthermore, I acquired images of each investigated structures using a scanning electron microscope (SEM). From the polarization dependend spectra, I selected the perependicular resonances that resemble the transverse and logitudinal plasmon modes. The results are shown in Figure 11.2.

The black vertical lines correspond to the transverse plasmon mode (along the base of the triangles) and the red vertical lines to the longitudinal mode. The transverse mode stays approximately at the same resonance position for all gap distances since it is apparently

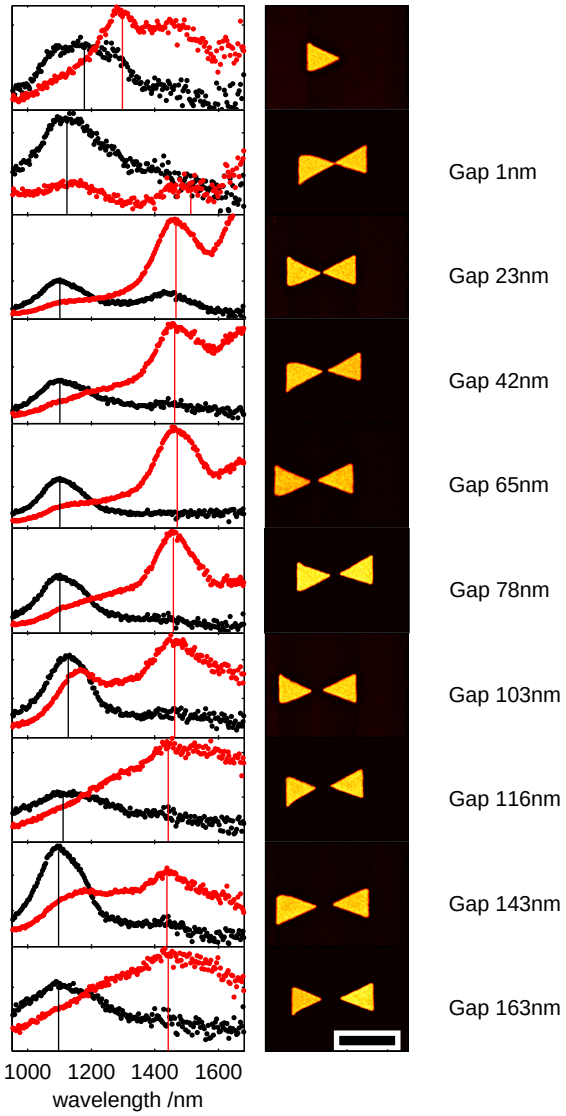

Figure 11.2: Showing spectra with perpendicular polarization for bowties with varying gap distances and a single triangle. The black dots depict the transverse plasmon oscillation and the red dots the longitudinal one. The scale bar is 500 nm.

unaffected by a plamon coupling in the longitudinal direction. The longitudinal mode shows a slight shift of ≈ 30 nm to smaller wavelengths when the gap size is increased. This effect is much less pronounced compared to the transmission measurements where the plasmon shifts by as much as 150 nm. Additionally, the resonance position for the biggest gap size almost matches the resonance position of the single triangle in thetransmission measurements, but in my single structure scattering measurements, there is a jump between the structure with a gap of 163 nm and the single triangle of ≈ 130 nm. The peak structure of the longitudinal modes looks also more complicated compared to the peaks in the transmission measurements. The general difference of about 150 nm can be attributed to difference in angle of incidence of the illumination light.[92,93]

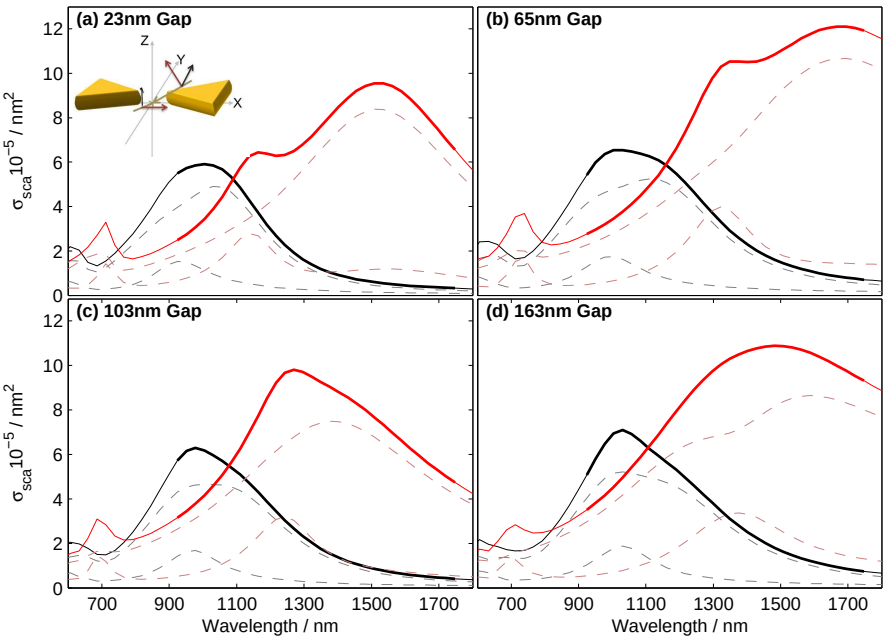

Figure 11.3: Simulated spectra of 4 different Bowtie structures. The dashed lines correspond to different combinations of directions of the polarization vector and the illumination vector. The full lines are the summed spectra of the same mode and the thick lines represent the actually measured wavelength range.

To understand this peak structure and to exclude measurement artefacts, I simulated some of the structures in BEM, using the size information, I obtained from the SEM images. Furthermore, I included the illumination geometry of our dark-field spectroscopy setup, i.e. the light is shining at $\approx 60°$ relative to the surface normal. In the simulation, I investigated the cases where the light shines along the longitudinal mode and along the transverse mode and in both cases with two perpendicular polarization directions (inset Figure 11.3) yielding 4 spectra per structure. Because of the size of the structures, these simulations where very demanding with respect to memory and time. And due to the free parameters thickness and edge sharpness, a comparison of simulation and experiment can be done only qualitatively, unfortunately.

Nevertheless, the results of the simulations look similar to my measurements.The spectra for the 4 combinations of the polarization vector and illumination vector (dashed lines in Figure 11.3) show different resonance positions even when the components of the polarization vectors in the xy-plane have the same direction (color coded in Figure 11.3: red dashed lines and black dashed lines correspond to the same direction of the polarization direction, where red and black represent the perpendicular directions). The summed spectra (of the same direction) show more than one peak, which weren't visible in the ensemble extinction spectra (Figure 11.1). Due to the illumination under oblique angles, there seems to be a complex interplay of different plasmon modes that are not excited this way or averaged out in the ensemble extinction measurements, where the light shines parallel to

the surface normal. Furthermore, there is an additional feature that might be investigated in future measurements, that is the resonance at around 700 nm, which corresponds to a resonance in z-direction in the simulations.

In summary, the single structure measurements show also a blue-shift when the gap size is increased like the ensemble spectra although the magnitude of shift is much smaller. Compared to ensemble spectra variations in the shape of single structures (for example broken tips at triangles) might add additional variations in the spectra because they are not averaged out. The overall offset in the resonance positions between single and ensemble spectra could be explained with the different angle of incidence of the illumination.[90,91] Simulations according to the resonance position difference are ongoing, due to the computational time. For future measurements, an investigation of the visible part of the spectra containing the resonance in z-direction (out-of-plane oscillation).

12

SINGLE UNLABELED PROTEIN DETECTION ON INDIVIDUAL PLASMONIC NANOPARTICLES

For this publication I provided a receipt to synthesize big rods and simulations in QSA and BEM for the calculation of the sensing volume as well as the noise calculations for Figure 12.3 and Figure 12.7. The noise calcuations I implemented in MATLAB to be easily adaptable to other setups of our group.

12.1 INTRODUCTION

MOSTLY hidden to us, dissolved molecules show complex conformational dynamics, molecular interactions and spatial diffusion at room temperature. Many of those features average out in measurements integrating over time or large ensembles of molecules. Knowing the detailed dynamics is essential to understand biological functions at the molecular level[94]. However, few experimental techniques provide access to molecular events in solution and commonly require fluorescent dye labels attached to the molecule of interest.[95] Analyte modification could potentially influence biological processes[96] triggering current searches for unlabeled protein detection methods. Currently optical microcavities (whispering gallery modes WGM),[97,98] surface-enhanced Raman scattering (SERS),[99] and electric detection via carbon nanotube[100] or boron-doped silicon nanowire[101] field-effect transistors are discussed for detection of unlabeled proteins. Each of those methods suffers from one or more disadvantages, e.g., complex sensor fabrication, or low signal-to-noise level, which has prevented their practical use in most cases. Here, we utilize single gold nanoparticles to detect single unlabeled proteins with high temporal resolution. In comparison with previously described techniques, the signal to noise ratio is significantly improved and allows the direct identification of single molecular binding and unbinding events. This allows now to resolve equilibrium coverage fluctuations otherwise hidden in ensemble measurements. Plasmonic sensors open new experimental access to the exciting Brownian dynamics of unlabeled macromolecules. Potentially, our method enables the study of protein folding dynamics, protein adsorption processes and kinetics, as well as non-equilibrium soft matter dynamics on the single molecule level. Our simulations predict the ability of the sensor concept to detect the presence of small molecules below a molecular weight of one kDa.

Plasmonic nanoparticles[102,103,104] react to refractive index changes in their direct environment by a shift of the plasmon resonance (Figure 12.1a). This can be monitored on single nanoparticles by optical dark-field spectroscopy.[33] So far, signal to noise ratio and time resolution was not sufficient to identify single molecular binding events. We

improved the plasmon spectroscopy technique considerably by using an intense light source (white light laser), an intensified CCD camera, and a tailored nanoparticle geometry. These changes allow for continuous monitoring of very small changes in the plasmon resonance wavelength with a time resolution at least 4 to 6 orders of magnitude better than the previous state of the art (Figure 12.1b). These improvements allow us to resolve discrete steps in the plasmon wavelength which are caused by single adsorbing molecules (Figure 12.1c).

With these advances to plasmon sensors, we introduce a new tool for label free single molecule detection. Compared to optical microcavities,[105] the plasmon sensor benefits from its less complex optical setup and simple wet-chemical sensor fabrication. In addition, the volume influencing the sensor is orders of magnitude better matched to typical molecular dimensions of proteins. Also, plasmonic nanoparticles can be inserted into living cells,[106] providing the potential opportunity for in-vivo monitoring of bio-molecules.

12.2 RESULTS AND DISCUSSION

For our experiments, rod-shaped gold nanoparticles are immobilized in a glass capillary with the possibility to introduce and change the liquid environment. The light scattering spectrum of a single gold nanorod is measured under illumination from a white light laser. The laser illuminates the particles in total-internal reflection geometry such that only scattered light is picked up by the microscope and spectrally investigated (Figure 12.1a). With this setup, we obtain single particle scattering spectra within a few milliseconds.

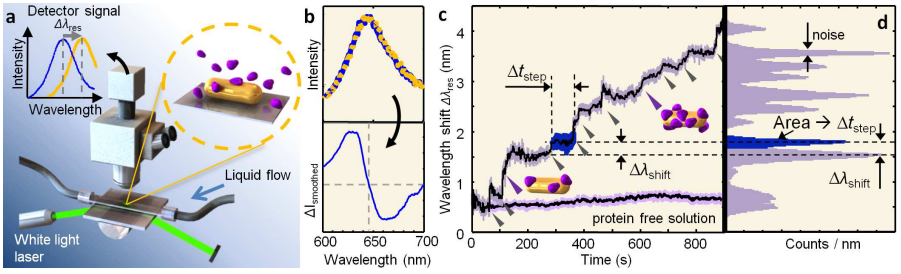

Figure 12.1: Experimental setup and time-resolved single protein attachment. (a) Diagram of our total internal reflection setup with a magnified view ofthe flow cell. The inset on the upper left illustrates the plasmonic wavelength shift at the heart of our sensing principle. (b) Measured resonance spectrum of a single Au nanorod with an exposure time of 10 ms before and after single protein attachment (upper panel) and the difference between both (lower panel). (c) Resonance wavelength of an individual nanorod during single protein attachment events and without protein solution. (d) Histogram of the same time trace showing distinct peaks for each step.

Molecular adsorption processes induce only very small shifts in the plasmon resonance when compared to the plasmon linewidth of about 50 nm. However, we are able to determine the plasmon resonance wavelength with an accuracy of 0.03 nm by fitting the entire spectral resonance. This accuracy corresponds to 1/1000 of the spectral

linewidth similar to the super-resolution obtained in STORM/PALM microscopy.[107,108] To investigate molecular binding events, we introduce the blood plasma protein fibronectin (molar weight 450 kDa). A shift in the plasmon resonance clearly indicates adsorption of fibronectin to the gold nanoparticles. The plasmon shift follows the Langmuir adsorption curves known from ensemble experiments (e.g. surface plasmon resonance sensors, SPR) with the characteristic time scaling with fibronectin concentration (Figure 12.4a). When we decrease the fibronectin concentration down to 1.25 µg ml^{-1}, discrete steps start to appear in the resonance wavelength time trace (Figure 12.1c). These discrete steps are caused by individual attaching molecules. We found that using wavelength histograms as shown in Figure 12.1d is the best way to systematically identify single protein binding steps. In the histogram, each Gaussian peak corresponds to a molecule attaching to the plasmon sensor. Neighboring Gaussian peaks are separated by $\Delta\lambda_{\text{shift}}$ and their integrated area yields the step time Δt_{step}. Assuming delta-like events, the width corresponds to the experimental noise level. For the experiment shown in Figure 12.1c, the average step height $\Delta\lambda_{\text{shift}}$ is approximately 0.3 nm with about Δt_{step} =50 s between steps and a noise level of 0.07 nm. Sometimes, step identification is difficult as expected from the small difference between step-height and noise level.

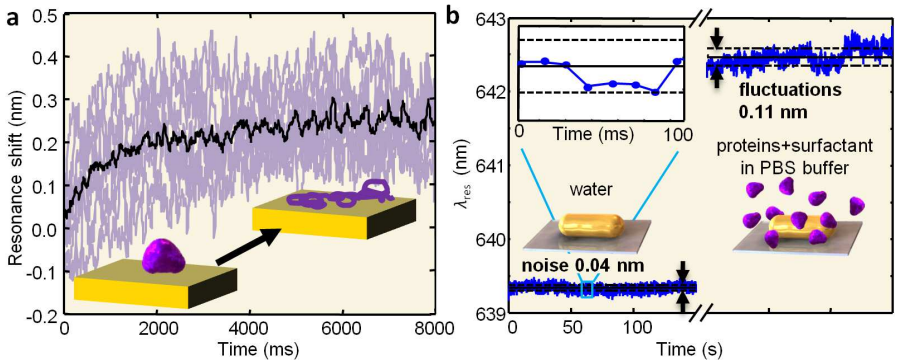

Figure 12.2: Time-resolved fibronectin binding dynamics and equilibrium fluctuations. (a) Mean adsorption behavior (black) averaged from 8 single adsorption events (violet) taken from a single rod. The deviation from a step-like form suggests a protein denaturing on the timescale of 10 s to 20 s (inset). (b) Compared to the noise level of 0.04 nm (standard deviation) in pure water, the fluctuation amplitude increases significantly to 0.11 nm in a protein surfactant mixture (25 µg ml^{-1} Fibronectin, 0.2wt% SDS) due to equilibrium protein coverage fluctuations.

We carefully checked that the observed steps indeed correspond to single protein binding events. The attachment frequency (the inverse of the time between steps Δt_{step}) increases as expected with protein concentration and is in quantitative agreement with theoretical predictions assuming diffusion limited rates (Figure 12.5a). Furthermore, the distribution of adsorption events follows Poissonian statistics (Figure 12.5b). To validate the step height $\Delta\lambda_{\text{shift}}$, we checked if it varies with protein size. Fibronectin is a dimeric protein that can be cleaved into its monomeric constituents by tris(2-carboxyethyl) phosphine,

TCEP. Indeed, the average shift or step height induced by monomeric fibronectin is about half the value as that of dimeric fibronectin (Figure 12.5c). As an additional validation, we follow the desorption of the proteins reported before[109] by washing with sodium dodecyl sulfate SDS. We observe clearly pronounced desorption steps (Figure 12.5d). However, the step height is significantly larger than for the adsorption steps, indicating the simultaneous desorption of clusters of proteins. The desorption process results in a plasmon resonance blue shifted compared to the original wavelength, indicating a negative charging of the gold particles[110] by SDS. A control experiment of pure gold nanorods exposed to SDS results in similar blue shift (Figure 12.4b). Taken together, the control experiments strongly confirm our achievement of single molecule sensitivity.

Being able to resolve single protein binding, we can try to time-resolve the adsorption process itself - information fundamentally hidden in ensemble measurements. For this, we manually superimpose and average all steps within one measurement to increase the signal to noise ratio further. We observe a plasmonic red-shift during the adsorption process with about 1.95 s timescale (Figure 12.2a). Similar observations show up on superimposed steps of other measurements (Figure 12.6) confirming the existence of a real physical process. We believe that this slow red-shift within one adsorption event arises from a slow denaturing of the protein on the surface, bringing it closer to the particle (Figure 12.2a inset). Such denaturing of proteins near metal surfaces is, by itself, a well known phenomenon.[111] Our method allows now for observation of the temporal evolution of this process in detail and should trigger the development of models to explain the observed denaturing timescale.

The most exiting feature of sensors with single molecule sensitivity is the window they provide to molecular dynamics, Brownian motion, equilibrium, and non-equilibrium fluctuations. Equilibrium coverage fluctuations give direct access to binding constants without mass transfer complications.[112] In addition, equilibrium fluctuations are linked to non-equilibrium properties via fluctuation-dissipation theorems.[113] The recent discovery of unexpected fluctuation theorems, e.g., the Jarzynski theorem,[114] have increased the demand for experimental techniques to study molecular fluctuations. Within our experiment, we observe equilibrium coverage fluctuations of fibronectin on the sensor surface under conditions of weak binding affinity. To adjust the binding affinity, we added both fibronectin and SDS and observed an increase in the fluctuation amplitude from 0.04 nm to 0.11 nm (Figure 12.2b). The stability of our current setup prevents us from recording time-traces long enough for statistical evaluation with respect to fluctuation theorems, but the results clearly show the potential for molecular coverage analysis.

To fully understand the future potential of single plasmonic nanoparticles as molecular sensors, we investigated theoretically and experimentally the limit of the method, in particular the improvements needed for detecting smaller molecules. It is important to understand that it is not trivial to choose the optimal nanorod size since

there is a trade-off of signal strength and resonance accuracy. Larger nanorods generally give stronger light scattering signals and should allow to determine the plasmon resonance with higher accuracy. (Retardation effects and radiation damping lead to increased plasmon linewidth at some point.) However, the sensing volume that influences the resonance position also increases with particle size (Figure 12.3a and Figure 12.5a in the Supporting Information) which decreases the perturbation caused by a single molecule. Indeed, experiments using large, medium and small gold nanorods (14 nm, 35 nm, 50 nm width) show larger median plasmon shifts for smaller particles (Figure 12.3b).

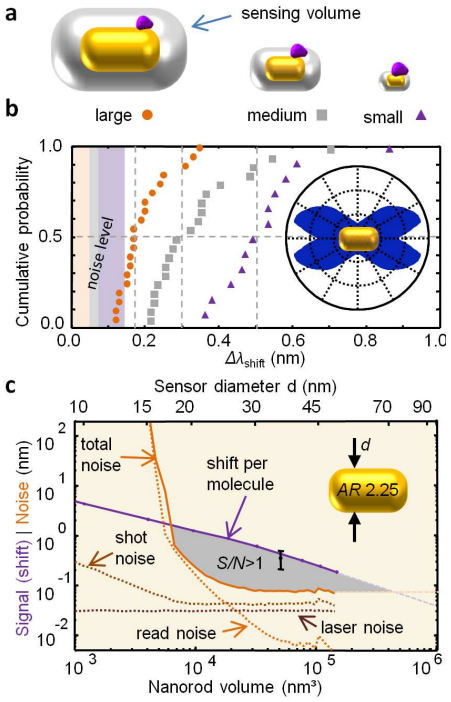

Figure 12.3: Optimal nanorod sensor dimensions. (a) The modification of sensing volume with particle size implies a change in occupied volume fraction. (b) Cumulative probability of measured resonance shifts per adsorbed molecule within one trace for large rods (orange, mean shift 0.17 nm), medium rods (gray, 0.30 nm), and small rods (purple, 0.51 nm). The respective noise level is shaded on the left hand side. The large-shift tail in the cumulative distribution is caused by the position dependent sensitivity along the rod (the inset shows a simulation for a 12 nm diameter protein on a 35 nm wide nanorod.). (c) Simulated shift induced by a 12 nm diameter adsorbing protein (purple) compared to the noise level of our setup. In the gray area, the signal to noise level is above one. The data point for 35 nm rods is the average shift per molecule as measured experimentally.

Using experimentally determined noise levels from our laser and camera and the sensor response (shift per molecule) calculated with the boundary element method,[13,115] we studied the signal to noise ratio for rods between 10 nm and 50 nm in width (aspect ratio AR 2.25). The results show an optimal size region with signal to noise S/N > 1 for particles with widths between 20 nm to 45 nm (Figure 12.3c). The calculated shift per molecule matches very well the measured value,

confirming once more single molecule detection. The theoretical description allows us to determine the limit of plasmonic nanoparticle sensors to detect small molecules. Increasing the laser power up to a point where the absorbed light increases the particle temperature by 1 K, we could detect molecules of 4 nm diameter within the current geometry and setup using nanorods with 20 nm width. Smaller nanorods improve the detection limit even more but require much stronger lasers. Further improvements would bring the use of plasmonic structures with even higher sensitivity such as metamaterials,[116,117,118] rattles,[85] silver particles,[80] or plasmonic hot spots.[119]

Single molecule detection with individual plasmonic nanoparticles is not simply a dramatic downscaling of current sensors but a qualitative new step as it resolves molecular dynamics. With our new scheme, we can monitor desorption and adsorption processes in real time on a single molecule basis including conformational protein dynamics. Additionally, we demonstrate its suitability for observing equilibrium coverage fluctuations. These fluctuations hold information about binding kinetics and non-equilibrium thermodynamics. Single plasmon biosensors are therefore a new tool to study fundamental phenomena on the molecular level with impact for understanding of biological processes and thermodynamics of small systems.

The dramatic improvements in signal to noise ratio for plasmon sensors we obtained here for our goal of single molecule detection will also improve other plasmonic sensors, e.g. plasmon rulers[120] or hydrogen sensors.[121]

12.3 EXPERIMENTAL SECTION

12.3.1 *Materials and Methods*

MATERIALS. Fibronectin from bovine plasma (F1141-1mg), Phosphate buffered saline (PBS) and sodium dodecyl sulfate (SDS) were bought from Sigma. The PBS solution was filtered with a 20 nm pore size filter before usage. Different concentrations of protein solution were prepared by diluting a concentrated fibronectin solution with PBS. The optimal concentration for the detection of single steps was 1.25 µg ml^{-1}.

SETUP. A commercial upright microscope from Zeiss (Axioscope) equipped with a white light laser (WLL) from Koheras (SuperK-Power, spectral regime 460 nm to 2400 nm, total average power output 2.8 W) as the illumination source was used. The laser was coupled via total internal reflection onto the sample (Figure 12.1). The scattered light was analyzed by an ImSpector V8 (Specim) coupled to an EM-CCD camera (iXon, Andor DV885). The exposure time for medium rods was 10 ms with a cycle time of 13.7 ms. The gain was adjusted if needed, normally ranging between no gain and gain factor five.

FLOW CELL. We used home-build flow cells consisting of a glass capillary (2 mm x 0.1 mm) attached with glue to flexible tubing. Thus, a liquid exchange was easily possible. The refractive index between the flow cell and the glass surface was matched with immersion oil.

SAMPLE PREPARATION. The gold nanorods we used as sensors were prepared in a two step wet-chemical synthesis. In the first step seeds were grown from $HAuCl_4$ solution. These seeds were then enlarged in a second step to gold nanorods. The dimensions used in the experiments range from small ($14\,nm \times 40\,nm$, $\lambda_{res} = 674\,nm$ over medium ($35\,nm \times 78\,nm$, $\lambda_{res} = 635\,nm$) to large ($50\,nm \times 107\,nm$, $\lambda_{res} = 664\,nm$) rods. Particles were immobilized with 1 M NaCl in the flow cell. Upon inspection in the TIR microscope, they were clearly visible to the eye as bright red spots on a dark background. Differences appeared in their intensity that scales quadratically with the particle volume. The immobilized gold nanorods were rinsed extensively in pure water and filtered PBS (0.01 M phosphate buffer, 0.0027 M potassium chloride and 0.137 M sodium chloride). Crucial to the quality of the experiment was the stability of the resonance wavelength. Stabilizing the wavelength normally took about one hour. When a stable resonance wavelength was achieved for several minutes, one end of the flow cell tubing was put into the protein solution and gravitational force generated a flow towards the gold nanorod under investigation. At this point in time, the measurement was started and no further adjustments at the setup were carried out during measurement.

12.3.2 *Control experiments*

ENSEMBLE LIKE ADSORPTION CURVE. We tested our system with different concentrations ($10\,\mu g\,ml^{-1}$ (22.2 nM), $5\,\mu g\,ml^{-1}$ (11.1 nM), and $1.25\,\mu g\,ml^{-1}$ (2.8 nM)) of fibronectin. The time dependence of the measured resonance shift is concentration dependent and can be described by $\Delta\lambda_{shift}/\Delta\lambda_{max} = 1 - e^{-ckt}$. In Figure S1 data of typical adsorption curves are plotted. The blue lines are fits with the adsorption coefficients k $=2.8 \times 10^{-4}\,cm^3\,s^{-1}\,\mu g^{-1}$, $2.6 \times 10^{-4}\,cm^3\,s^{-1}\,\mu g^{-1}$ and $2.6 \times 10^{-4}\,cm^3\,s^{-1}\,\mu g^{-1}$, respectively (from lowest to highest concentration). In literature, a value of
$1.0 \times 10^{-4}\,cm^3\,s^{-1}\,\mu g^{-1}$ for the adsorption coefficient of fibronectin on gold is reported. The inset shows a comparison of the actual concentrations to the concentrations calculated only using this literature value for the adsorption coefficient of fibronectin to gold. The good agreement of our data obtained on single particles with this literature value and the correct concentration dependent behavior of the adsorption dynamics, proofs that fibronectin is solely responsible for the observed shifts.

ATTACHMENT FREQUENCY. The time between steps varies systematically with concentration and agrees with that calculated for diffusion limited adsorption processes. In more detail, the number of

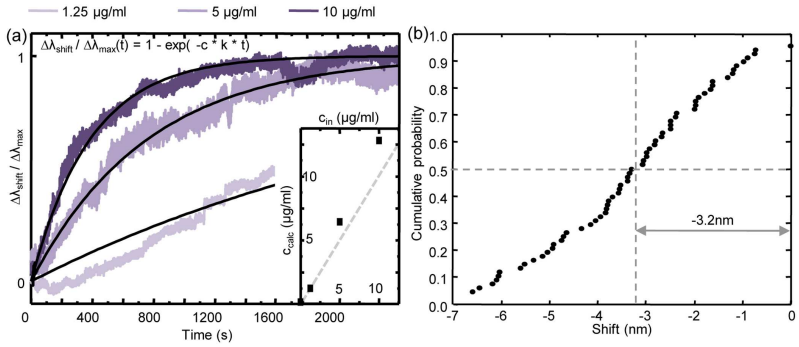

Figure 12.4: (a) Ensemble-like adsorption curves of fibronectin on Au nanorods at different concentrations of fibronectin. The blue lines are fits. The inset shows a comparison of the actual solution concentration to the concentration calculated from the adsorption curves using the value $6.9\times10^{-4}\,\mathrm{cm\,s^{-1}}\,a/m = 1.0\times10^{-4}\,\mathrm{cm^3\,s^{-1}\,\mu g}$ (1) for the adsorption coefficient of fibronectin on gold (footprint area $a = 11\times10^{-14}\,\mathrm{cm^2}$, dry mass of single protein $m = 7.5\times10^{-13}\,\mu\mathrm{g}$). The gray dashed line is the ideal fit.(b) Control experiment of gold nanorods exposed to pure SDS solution shows a blue shift similar to the one observed after fibronectin desorption, most likely due to negative charging of the nanoparticles.

protein hits on an area after time t is described by $N = cA_{rod}(Dt)^{1/2}$, where c is the protein concentration, Arod the available surface of the rod, and D the diffusion constant. The latter is described by the Einstein-Stokes law $D = k_\mathrm{B}T/(6\pi\eta r)$ (Boltzman constant k_B, temperature T, viscosity η, protein radius r). -This equation is only valid for the first few adsorbing molecules (afterwards the amount of the particle surface already occupied has to be taken into account), so we only take the first five events into account. The time of the measurement (for the first 5 steps) therefore varies with concentration. The calculated number of attachment events is presented in Figure 12.5a together with the measured values. The calculated and measured numbers of events are in good agreement. (Values used: $T = 300\,\mathrm{K}$, $r = 6\,\mathrm{nm}$, $A_\mathrm{rod} = 5718\,\mathrm{nm^2} = 2/3\pi ab$ with rod dimensions a, b)

POISSONIAN STATISTICS. The arriving time of the proteins, defined as the time between events, is checked against a Poissonian distribution. Such a Poissonian distribution gives evidence for single uncorrelated events. The entire trace is therefore divided into bins defined by the mean arriving time. Counting the number of events within each bin gives the statistics shown in Figure S2b. Checking the measured distribution with a χ^2-Test against the expected values for Possonian statistics supports the hypothesis of uncorrelated events with a confidence level larger than 95%.

MOLECULAR SIZE INFLUENCES THE INDUCED SHIFT. The third strong hint for single molecule events is the dependence of the step size, $\Delta\lambda_\mathrm{shift}$, on the size of the protein. As expected, smaller proteins show a smaller shift (see Figure S2c). This was tested by cutting the fibronectin dimer into monomers by addition of 5 mM tris(2-carboxyethyl)phosphine (TCEP, Sigma). After 5 min of incubation, the

solution was ready to use. Notice, at this molecule size the detection limit was reached, thus identification of single binding events became difficult.

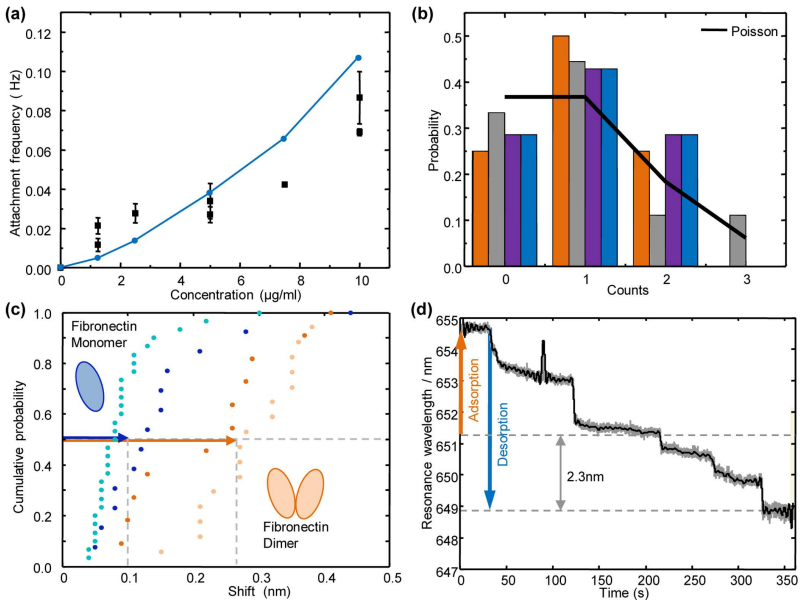

Figure 12.5: Control measurements confirming single protein attachment. (a) Influence of fibronectin concentration on attachment frequency. Measured data (black), calculated data (blue). (b) Probability of protein adsorption events within the mean adsorption time for four different time traces. The black line corresponds to a perfect Poissonian distribution. (c) Cumulative probability of measured resonance shifts per adsorbed molecule within four time traces. Two time traces correspond to the attachment of fibronectin dimers (light and dark orange) and two to fibronectin monomers (light and dark blue). (d) Protein desorption in the presence of SDS. The final resonance wavelength is blue shifted by 2.3 nm compared to the resonance position of the rod before adsorption due to particle charging (see Figure 12.4b).

DESORPTION. As an additional validation of the experiment, we measured desorption of the proteins caused by washing with 0.2 wt% SDS. Figure 12.5d shows a typical desorption curve. Notice, that desorption steps are larger in height compared to adsorption steps and there are less in number. This indicates the detachment of several proteins together. Also the final resonance wavelength of the sensing particle is blue shifted compared to the starting value before adsorption. SDS is known to transfer negative charges which can shift the resonance position of a plasmonic nanoparticle to the blue3. As a control experiment, CTAB coated nanorods were washed with SDS without any fibronectin. In this case, the resonance wavelength of the gold nanorods also blue shifts (see Figure 12.4b). Washing the particles again with 50 mM CTAB or 1 M NaCl solution, shifts the resonance back to its original value.

ADDITIONAL AVERAGED BINDING STEPS. In Figure 12.6, additional averaged binding steps are plotted. Each graph is taken from a different nanorod while all violet traces within one graph show differ-

ent binding steps on the same nanorod. The averaged binding event is shown in black. Fitting the averaged curve with $\Delta\lambda_{\text{shift}} = A(1 - e^{-t/\tau})$ gives the following time scales for the binding events: 2.08 s, 1.28 s and 1.85 s. The parameter A describes the height of the final shift.

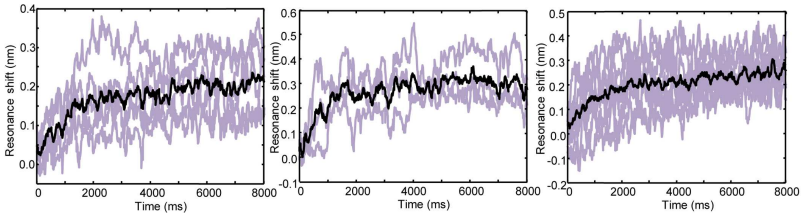

Figure 12.6: Additional time traces of superimposed steps. Each graph shows data taken from a different nanorod. Violet traces show different binding events on the same nanorod. The black curve is the average of the violet traces.

12.3.3 *Simulations*

SIMULATION OF EXPECTED SHIFTS. In addition to the experiments, we simulated the expected shift per adsorbed molecule, $\Delta\lambda_{\text{shift}}$. It was proportional to the change in refractive index, Δn, the plasmonic sensitivity, $S = \Delta\lambda_{\text{shift}}/\Delta n$, and the volume fraction V_{frac} of the protein V_{prot}[1] to the total sensing volume V_{sens}, i.e. $V_{\text{frac}} = V_{\text{prot}}/V_{\text{sens}}$. Together it follows that $\Delta\lambda_{\text{shift}} = S\Delta n V_{\text{frac}}$. All simulations were performed for gold nanorods with the aspect ratios of $AR = 2.25$, the dielectric function of gold from Johnson&Christy4 and a spherically capped cylinder as shape for the gold nanorod.

We approximated the refractive index change induced by the protein with $\Delta n = 0.17$ taking the literature value for a typical refractive index of a biomolecules of 1.55, which is 0.17 difference to water. The sensitivity S of these particles was numerically calculated (Figure 12.7a). It changed only slightly from 160 nm/RIU to 240 nm/RIU for rods with diameters between 5 nm and 50 nm. Hence, the important term for the size of the induced shift per molecule $\Delta\lambda_{\text{shift}}$ was the volume fraction V_{frac}, the ratio between the fixed analyte volume V_{prot} and the sensing volume V_{sens}.

To estimate the volume fraction, we first determined the sensing distance d that produces $1/e$ of the maximum shift.(i.e. a gold nanorod in a medium with $n = 1.5$). Technically, we simulated the plasmon resonance for a given particle size with an increasing shell of protein around it using the boundary element method (BEM) (Figure 12.7b). From the sensing distance, the sensing volume V_{sens} is obtained by $\pi d[ab + ad + bd + 4/3d^2]$with rod length a, width b and sensing distance d. We found that the sensing volume is approximately equal to the particle volume.

Multiplication of these parameters (change in refractive index Δn, plasmonic sensitivity S, volume fraction V_{frac}) gives the shift per

1 The protein volume needs to be corrected if the protein extends out of the sensing volume. In this case, only the protein volume inside the sensing volume is counted.

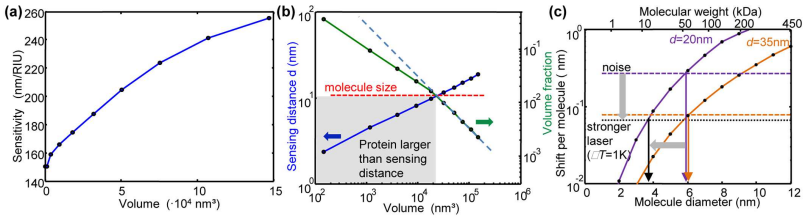

Figure 12.7: Simulated values for plasmon shifts induced by adsorption of single molecules. All values are simulated for gold nanorods with a fixed aspect ratio of 2.25. (a) The plasmonic sensitivity ($\Delta\lambda/\Delta n$) as a function of nanorod volume. (b) Sensing distance d (blue) of the volume influencing the plasmon resonance and the volume fraction (green) that a fibronectin molecule (diameter 12 nm, dashed line) is occupying in this sensing volume. If the protein diameter is larger than the sensing distance (for small gold nanorods), the volume fraction is not increasing as much as before. (c) The resonance shift per adsorbed molecule for two gold rods with a width of 20 nm (purple) and 35 nm (orange) as a function of molecule diameter. The vertical dashed lines show the noise values in the current setup (the noise level is smaller for the larger rods due to their stronger light scattering cross section). Irrespective of rod diameter, the smallest detectable protein is currently about 6 nm in diameter (the effect of better signal for larger rods and larger shift per molecule for smaller rods almost cancel out).

molecule, $\Delta\lambda_{\text{shift}}$. A simplified simulation based on the quasi-static approximation confirms the obtained values giving surprisingly comparable result.

SIMULATION OF THE SETUP NOISE. To get insight into the final values for the noise from the participating noise sources, we first measured each of them individually. We then included as well the power of the light source, the scattering efficiency of the sample, measured transmission losses in the light path, and the quantum efficiency of the EM-CCD camera to determine the final noise values.

The laser noise was measured for 10000 frames (t_{exp} 30 µs to 0.1 s) on a bright white silica particle (diameter 314 nm). The normalized standard deviation of the intensity at various wavelength gave values around 1.5%, which is in good agreement manufacturer specification.

The read noise is the noise introduced by the CCD camera while reading out, independent from the signal level. It was measured for several gain values by subtracting two dark pictures with minimal exposure times and extracting the standard deviation of the noise. As two pictures were used, the noise is reduced by square root of two. The gain dependent read noise for 20 binned pixels was measured to be $15.903 + (1.151\text{gain}) + (0.007\text{gain}^2)$. Due to the thermoelectric cooling of the camera, dark current noise is negligible.

The shot noise originates from photon statistics and is given by the square root of the number of arriving photons.

To determine the noise specific to a given particle size, the scattering spectrum for a set exposure time of 10 ms was calculated using the measured effective setup transmission for the given illumination flux of 2.4×10^{21} photons per second, wavelength and m^2 for a particle scattering cross section of $3.9\times10^{-15}\,\text{m}^2$. The maximum possible

gain without saturating the camera was used. Each wavelength of this "perfect spectrum" was mathematically overlaid with random values for all noise terms taken from a Gaussian distribution multiplied with the previously determined noise.

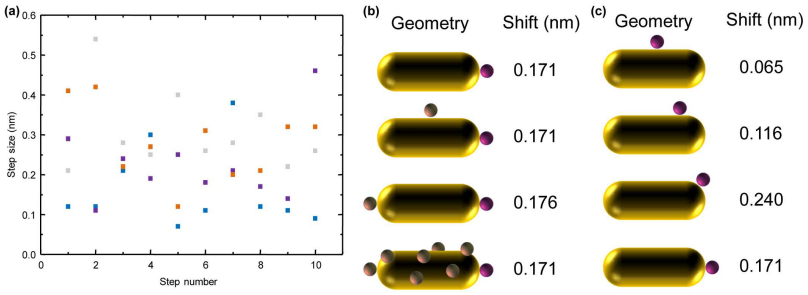

Figure 12.8: (a) Step height ($\Delta\lambda_{\text{shift}}$) as a function of proteins already adsorbed. The experimental data, shown here for four different time traces in different colors, shows no apparent trend as expected. (b)-(c) Shifts calculated with the boundary element method (BEM). (b) Shift after the addition of one protein (pink) with and without other proteins (brown) already present. (c) Calculated shifts for a protein attaching at different positions along the gold nanorod.

SIMULATION OF ATTACHMENT POSITION SENSITIVITY. Again, we used the boundary element method BEM to simulate particle spectra. The shift between a naked nanorod and a nanorod with an attached protein was calculated for various positions of the protein along the nanorod surface. The results are shown in Figure 12.3b. A protein at the middle of the side position gave the minimal shift and at 10° away from the tip, the maximum shift. The ratio of the two is about 4 which agrees well with the measured variation in shift magnitudes for proteins adsorbing on the same gold nanorod.

HISTORY DEPENDENCE. Furthermore, we carried out simulations to investigate the role of the number of proteins already attached. For this, we added one molecule at a given position to particles covered with increasing number of other molecules. The shift for this one molecule did not depend much on the surface coverage compared to the dependence on attachment position (see Figure 12.8b and c).

13

SUMMARY

In this thesis, I have presented new experimental results on the synthesis of gold nanorods as well as on the measurement of single particle spectra and I want to summarize them here, briefly.

In Chapter 9, I presented my automized dark-field microscope that is capabable of collecting spectra in the range of 450 nm to 1750 nm. I showed the characteristics of that setup for the spectra acquisition in the UV-VIS range and how I used this information to simulate the measurements. Additionally, I show the major noise sources of the measurements and ways to reduce the noise. My setup was replicated three times until now and has become the state of the art measurement platform in our group.

Using this setup, I showed how to estimate the size of gold nanorods directly from the plasmon linewidth measured from optical spectra utilizing the well-known increase of radiation damping with nanoparticle size (Chapter 10). I verified this approach by collecting high-resolution scanning electron microscopy (SEM) images of the same particles and obtained an agreement within the SEM accuracy (< 10%). Then I used this information to reduce the distribution (between particles) of the measured plasmonic sensitivity S by 30% by correcting for the systematic error introduced from the variation in particle size. In Chapter 12, I showed how the combination of setup charactersitics and simulations of sensitivity and sensing volume can be used to select appropriate gold rods for single unlabeled protein detection . Additionally, I showed single particle spectroscopy in the IR region in Chapter 11. I investigated the single particle scattering of Bowtie structures. These structures consisted of two (mostly) equilateral triangles pointing one tip at each other. I used the polarization filter to acquire their polarization depend spectra and acquired images of each investigated structures using a SEM. Furthermore, I simulated the spectra of the structures considering the oblique illumination angle in our setup, which leads to additional plasmon modes in the spectra. The simulations agreed well with the measurements form a qualitative point of view.

In the synthetic part of my thesis, I used a combination of SAXS and optical extinction spectroscopy to investigate the formation of gold nanorods and nanorods from a gold-copper alloy (Chapter 5). The latter represented one of the first metal alloy nanoparticle synthesis protocols for producing rod-shaped single crystalline gold-copper ($Au_xCu_{(1-x)}$) alloyed nanoparticles, which is shown in Chapter 3. I characterizef them with various direct and indirect optical and electron microscopy techniques in order to verify the presence of copper in the particles. The optical and SAXS spectra allowed me to extract the mean particle width $D(t)$ and the mean length $L(t)$ as well as the width and length distributions $\sigma_D(t)$ and $\sigma_L(t)$. I found that

both length and width independently follow an exponential growth behavior with different time-constants, which intrinsically leads to a switch between positive and negative aspect ratio growth during the course of the synthesis. This switching from "1D" (mainly extension in length) to "3D" (extension in all directions) growth is accomplished without a change in growth mode and limits the aspect ratio of the final products to about 3.

In Chapter 6, I show the results from a second session at the SAXS-beamline of the Paul-Scherrer Institute. Here, I studied the influence of each entity in the growth solution on the kinetics of the growth except ascorbic acid using again simultaneous SAXS and UV-VIS spectroscopy. But differently to my earlier work, I extracted apparent rate constants for length and width growth using a Boltzman function (Equation 6.1), which can be the same as an exponential function. Each component in the growth solution was varied keeping the others constant. I found a linear relation of the rate constants as a function of $[HAuCl_4]/[CTAB]$ ratio pointing at a the loading of CTAB-micelles with gold-ions and the influence of different diffusion velocities of CTAB-micelles. The rate per seed as function of $[HAuCl_4]/[seed]$ ratio also increased linearly, which can be explained by the amount of monomer per seed available. Furthermore, I saw a correlation of final aspect ratio and ratio of rate constants for length and width growth rate for different $[AgNO_3]/[HAuCl_4]$ ratios. On very high silver concentrations only spheres are obtained as expected. In an additional experiment, I identified ascorbic acid as the yield limiting species in the reaction by the use of spectroscopic monitoring and TEM (Chapter 4.

As stated in Chapter 7, most of my synthetic work I performed in the framework of the research project “nanopolymeric contrast agents for photoacoustic imaging" (short title: POLYSOUND), which was a joint project of the Fraunhofer Institute for Biomedical Engineering (IBMT), the Centre for Biomaterial Development (GKSS, part of Helmholtz-Zentrum Geesthacht Centre for Materials and Coastal Research), and our group, funded by the German Federal Ministry of Education and Research BMBF. It was a succesful feasability study of a proof of principle of the concept of photoacoustic imaging in biomaterials using NIR-absorbing nanoparticle polymers, which will degrade and be egested by natural matabolism and gold nanorods with plasmon resonance that can be tuned to meet application requirements. I was responsable for the research on the nanorod synthesis, which was to be extended to provide nanorods that absorb light at 1064 nm as well as the reporting of our part in this project.

Part IV

APPENDICES

A

ESTIMATION OF DARK CURRENT

Showing the measurements for the dark current. I kept the shutter of the camera closed and blocked the light path to the camera in the microscope additionally. Then I changed the exposure time from 0.1s to 600s and acquired three images at each exposure time for 6 different temperatures. In each image I estimated the mean value and I used the three repeat measurements to estimate the standard deviation, which are shown in Figure A.1. The slope of the mean ADU/px or e/px as function of exposure time yields the dark current.

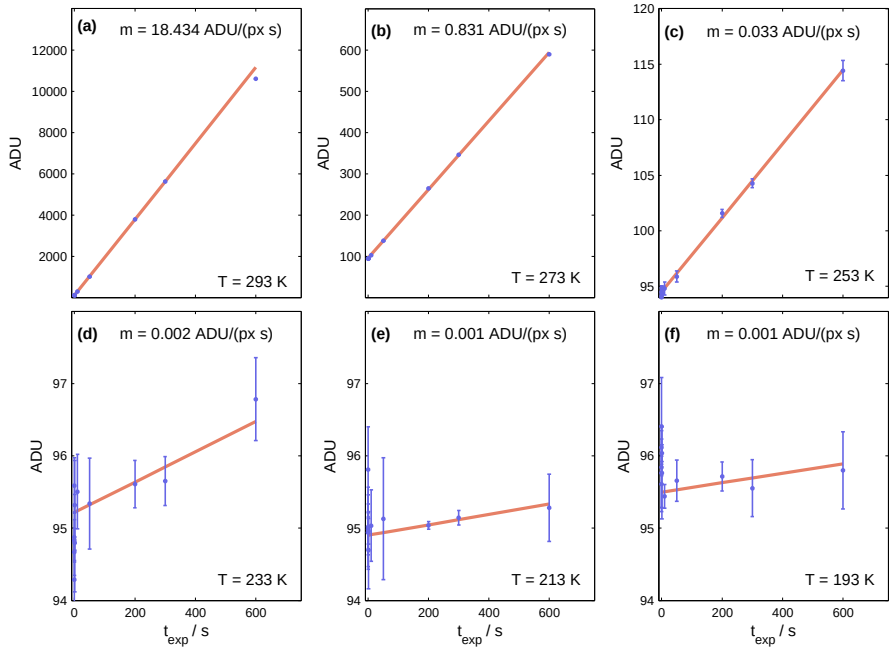

Figure A.1: (a)-(f) Showing the mean pixel ADU! for different exposure times from 0.01 s to 600 s at 293 K, 293 K, 273 K, 253 K, 233 K, 213 K, and 193 K, respectively. The slope in each graph represents the dark current as ADU/(px s). Using the system gain, these can be converted to e/(px s) as shown in Figure A.2.

The dark current as function of temperature is shown in Figure A.2. It can be seen that at 193 K it can be neglected in the simulations.

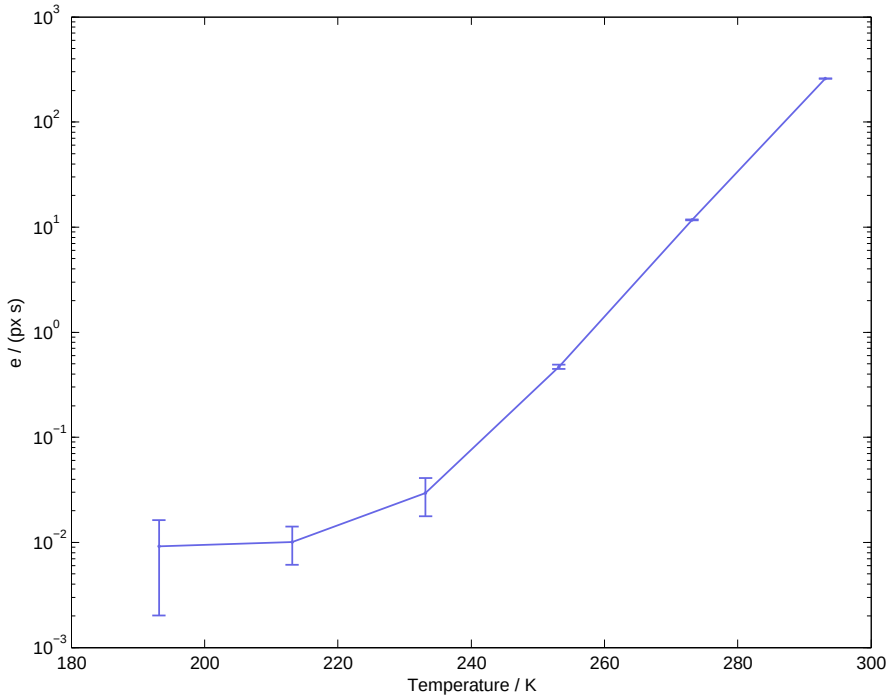

Figure A.2: Dark current as function of temperature.For the deep cooled CCD may be neglected — especially for small exposure times.

B

POLYNOMS AND COEFFICIENTS FROM BEM

THE INTERPOLATION POLYNOMS. D, R, and S were interpolated by performing a surface fit with 5^{th} order polynomials,

$$D = \sum_{m+n\leq 5} a^D_{mn} E^m_{\text{res}} \Gamma^n , \tag{B.1}$$

$$R = \sum_{m+n\leq 5} a^R_{mn} E^m_{\text{res}} \Gamma^n , \tag{B.2}$$

$$S = \sum_{m+n\leq 5} a^S_{mn} D^m R^n . \tag{B.3}$$

The numerical values for the coefficients are given in Table B.1.

Table B.1: Table containing the obtained coefficients for the function f(x,y) as denoted in Equation B.1, Equation B.2, and Equation B.3.

COEFFICIENTS	*D*	*AR*	*S*
a_{00}	1858.453	104.803	4114.825
a_{01}	-56851.210	1310.219	-7223.749
a_{02}	306521.856	-3891.239	5133.028
a_{03}	242341.782	-14656.461	-1768.073
a_{04}	-2115652.723	52375.224	300.632
a_{05}	2915233.841	-60879.876	-20.221
a_{10}	-1256.189	-379.412	-78.541
a_{11}	74365.292	-2406.678	64.366
a_{12}	-622719.345	11094.404	-19.315
a_{13}	476542.043	-1463.110	2.592
a_{14}	-101067.185	-2691.703	-0.144
a_{20}	-364.221	526.597	2.854
a_{21}	-2849.150	1059.797	-1.341
a_{22}	311925.861	-6477.111	0.147
a_{23}	-118474.366	786.683	0.005
a_{30}	-920.665	-325.280	-0.071
a_{31}	-21236.973	21.481	0.026
a_{32}	-52694.001	1233.149	-0.002
a_{40}	1234.240	88.844	0.001
a_{41}	6181.779	-68.562	-0.0001358
a_{50}	-331.533	-8.202	-0.0000032

BIBLIOGRAPHY

[1] M. Faraday, T. Martin, W. Bragg, and T. R. I. of Great Britain, *Faraday's Diary (7 Vol. Set)*. HR DIRECT, 2008.

[2] J. C. Maxwell, "A dynamical theory of the electromagnetic field," *Philosophical Transactions of the Royal Society of London*, vol. 155, pp. 459–512, 1865.

[3] L. Rayleigh, "XXXIV. on the transmission of light through an atmosphere containing small particles in suspension, and on the origin of the blue of the sky," *Philosophical Magazine Series 5*, vol. 47, no. 287, pp. 375–384, 1899.

[4] G. Mie, "Beiträge zur Optik trüber Medien, speziell kolloidaler Metallösungen," *Annalen der Physik*, vol. 330, no. 3, pp. 377–445, 1908.

[5] R. Gans, "über die form ultramikroskopischer goldteilchen," *Annalen der Physik*, vol. 342, no. 5, pp. 881–900, 1912.

[6] H. Siedentopf and R. Zsigmondy, "Über Sichtbarmachung und Größenbestimmung ultramikoskopischer Teilchen, mit besonderer Anwendung auf Goldrubingläser," *Annalen der Physik*, vol. 315, no. 1, pp. 1–39, 1902.

[7] R. P. Feynman, "There's plenty of room at the bottom," *Engineering and Science*, vol. 23, pp. 22–36, February 1960.

[8] "Michael faraday," 2012.

[9] M. Faraday, "The bakerian lecture: Experimental relations of gold (and other metals) to light," *Philosophical Transactions of the Royal Society of London*, vol. 147, pp. 145–181, 1857.

[10] P. Johnson and R. Christy, "Optical constants of noble metals," *Phys Rev B Phys Rev B*, vol. 6, no. 12, pp. 4370–4379, 1972.

[11] C. Bohren and D. R. Huffman, *Absorption and Scattering of Light by Small Particles*. Wiley-Interscience, 1983.

[12] S. Prescott and P. Mulvaney, "Gold nanorod extinction spectra (vol 99, art no 1235047, 2006)," *J Appl Phys*, vol. 99, pp. 123504–, 2006.

[13] F. J. García de Abajo and A. Howie, "Retarded field calculation of electron energy loss in inhomogeneous dielectrics," *Phys. Rev. B*, vol. 65, p. 115418, Mar 2002.

[14] U. Hohenester and A. Trugler, "Mnpbem - a matlab toolbox for the simulation of plasmonic nanoparticles," *Computer Physics Communications*, vol. 183, no. 2, pp. 370–381, 2012. 868OA Times Cited:1 Cited References Count:36.

[15] C. Sönnichsen, T. Franzl, T. Wilk, G. von Plessen, J. Feldmann, O. Wilson, and P. Mulvaney, "Drastic reduction of plasmon damping in gold nanorods," *Phys. Rev. Lett.*, vol. 88, p. 077402, Jan 2002.

[16] M. Hu, C. Novo, A. Funston, H. Wang, H. Staleva, S. Zou, P. Mulvaney, Y. Xia, and G. V. Hartland, "Dark-field microscopy studies of single metal nanoparticles: understanding the factors that influence the linewidth of the localized surface plasmon resonance," *J. Mater. Chem.*, vol. 18, pp. 1949–1960, 2008.

[17] C. Novo, D. Gomez, J. Perez-Juste, Z. Zhang, H. Petrova, M. Reismann, P. Mulvaney, and G. V. Hartland, "Contributions from radiation damping and surface scattering to the linewidth of the longitudinal plasmon band of gold nanorods: a single particle study," *Phys. Chem. Chem. Phys.*, vol. 8, pp. 3540–3546, 2006.

[18] G. J. Nusz, A. C. Curry, S. M. Marinakos, A. Wax, and A. Chilkoti, "Rational selection of gold nanorod geometry for label-free plasmonic biosensors," *ACS Nano*, vol. 3, no. 4, pp. 795–806, 2009.

[19] N. R. Jana, L. Gearheart, and C. J. Murphy, "Seed-mediated growth approach for shape-controlled synthesis of spheroidal and rod-like gold nanoparticles using a surfactant template," *Advanced Materials*, vol. 13, no. 18, pp. 1389–1393, 2001.

[20] J. Pérez-Juste, I. Pastoriza-Santos, L. M. Liz-MarzÃ!'n, and P. Mulvaney, "Gold nanorods: Synthesis, characterization and applications," *Coordination Chemistry Reviews*, vol. 249, no. 17, pp. 1870 – 1901, 2005. <ce:title>36th International Conference on Coordination Chemistry, Merida, Mexico, July 2004</ce:title>.

[21] M. Liu and P. Guyot-Sionnest, "Synthesis and optical characterization of au/ag core/shell nanorods," *J Phys Chem B*, vol. 108, no. 19, pp. 5882–5888, 2004.

[22] X. Wang, Z. Zhang, and G. Hartland, "Electronic dephasing in bimetallic gold-silver nanoparticles examined by single particle spectroscopy," *J Phys Chem B*, vol. 109, no. 43, pp. 20324–20330, 2005.

[23] J. Becker, I. Zins, A. Jakab, Y. Khalavka, O. Schubert, and C. Sönnichsen, "Plasmonic focusing reduces ensemble linewidth of silver-coated gold nanorods," *Nano Lett*, vol. 8, no. 6, pp. 1719–1723, 2008.

[24] R. Schaak, A. Sra, B. Leonard, R. Cable, J. Bauer, Y. Han, J. Means, W. Teizer, Y. Vasquez, and E. Funck, "Metallurgy in a beaker: Nanoparticle toolkit for the rapid low-temperature solution synthesis of functional multimetallic solid-state materials," *J Am Chem Soc*, vol. 127, no. 10, pp. 3506–3515, 2005.

[25] A. Sra and R. Schaak, "Synthesis of atomically ordered aucu and aucu3 nanocrystals from bimetallic nanoparticle precursors," *J Am Chem Soc*, vol. 126, no. 21, pp. 6667–6672, 2004.

[26] A. Sra, T. Ewers, and R. Schaak, "Direct solution synthesis of intermetallic aucu and aucu3 nanocrystals and nanowire networks," *Chem Mater*, vol. 17, no. 4, pp. 758–766, 2005.

[27] G. M. Dalpian and J. R. Chelikowsky, "Self-purification in semiconductor nanocrystals," *Phys. Rev. Lett.*, vol. 96, p. 226802, Jun 2006.

[28] D. J. Norris, A. L. Efros, and S. C. Erwin, "Doped nanocrystals," *Science*, vol. 319, no. 5871, pp. 1776–1779, 2008.

[29] P. Villars, L. Calvert, and W. Pearson, *Pearson's handbook of crystallographic data for intermetallic phases*. Metals Park, Oh: American Society for Metals, 1985.

[30] S. Prescott and P. Mulvaney, "Gold nanorod extinction spectra (vol 99, art no 1235047, 2006)," *J Appl Phys*, vol. 103, no. 11, pp. —, 2008.

[31] W. Köster and R. Stahl, "Über den einfluß von legierungsbildung, verformung und rekristallisation sowi von nah- und fernordnung auf optische konstanten der edelmetalle und ihrer legierungen," *Zeitschrift für Metallkunde*, vol. 58, pp. 768–, 1967.

[32] J. Becker, O. Schubert, and C. Sönnichsen, "Gold nanoparticle growth monitored in situ using a novel fast optical single-particle spectroscopy method," *Nano Lett*, vol. 7, no. 6, pp. 1664–1669, 2007.

[33] C. Sönnichsen, T. Franzl, T. Wilk, G. von Plessen, J. Feldmann, O. Wilson, and P. Mulvaney, "Drastic reduction of plasmon damping in gold nanorods," *Phys Rev Lett*, vol. 88, no. 7, pp. 077402–, 2002.

[34] C. Linde, "Röntgenographische uns elektrische untersuchungen des cuau-systems," *Annalen Der Physik*, vol. 25, no. 1, pp. 1–48, 1936.

[35] J. Banhart and G. Czycholl, "Electrical conductivity of long-range-ordered alloys," *Europhys. Lett.*, vol. 58, no. 2, pp. 264–270, 2002.

[36] B. Nikoobakht and M. El-Sayed, "Preparation and growth mechanism of gold nanorods (nrs) using seed-mediated growth method," *Chem Mater*, vol. 15, no. 10, pp. 1957–1962, 2003.

[37] C. Orendorff and C. Murphy, "Quantitation of metal content in the silver-assisted growth of gold nanorods," *J Phys Chem B*, vol. 110, no. 9, pp. 3990–3994, 2006.

[38] C. Novo, A. Funston, and P. Mulvaney, "Direct observation of chemical reactions on single gold nanocrystals using surface plasmon spectroscopy," *Nat Nano*, vol. 3, no. 10, pp. 598–602, 2008.

[39] A. Plech, V. Kotaidis, A. Siems, and M. Sztucki, "Kinetics of the x-ray induced gold nanoparticle synthesis," *Phys Chem Chem Phys*, vol. 10, no. 26, pp. 3888–3894, 2008.

[40] B. Abecassis, F. Testard, O. Spalla, and P. Barboux, "Probing in situ the nucleation and growth of gold nanoparticles by small-angle x-ray scattering," *Nano Lett Nano Lett*, vol. 7, no. 6, pp. 1723–1727, 2007.

[41] A. Henkel, A. Jakab, G. Brunklaus, and C. Sönnichsen, "Tuning plasmonic properties by alloying copper into gold nanorods," *J Phys Chem C*, vol. 113, no. 6, pp. 2200–2204, 2009.

[42] A. Brioude, X. Jiang, and M. Pileni, "Optical properties of gold nanorods: Dda simulations supported by experiments," *J Phys Chem B*, vol. 109, no. 27, pp. 13138–13142, 2005.

[43] A. Bergmann, G. Fritz, and O. Glatter, "Solving the generalized indirect fourier transformation (gift) by boltzmann simplex simulated annealing (bssa)," *J Appl Crystallogr*, vol. 33, pp. 1212–1216, 2000.

[44] H. Kaya, "Scattering from cylinders with globular end-caps," *J Appl Crystallogr*, vol. 37, pp. 223–230, 2004.

[45] O. Glatter and O. Kratky, *Small Angle X-ray Scattering*. Academic Press, 1982.

[46] J. Boleininger, A. Kurz, V. Reuss, and C. Sönnichsen, "Microfluidic continuous flow synthesis of rod-shaped gold and silver nanocrystals," *Phys Chem Chem Phys*, vol. 8, no. 33, pp. 3824–3827, 2006.

[47] C. Burda, X. Chen, R. Narayanan, and M. El-Sayed, "Chemistry and properties of nanocrystals of different shapes," *Chem Rev*, vol. 105, no. 4, pp. 1025–1102, 2005.

[48] X. Peng, "Mechanisms for the shape-control and shape-evolution of colloidal semiconductor nanocrystals," *Adv Mater*, vol. 15, no. 5, pp. 459–463, 2003.

[49] X. Xu, F. Liu, K. Yu, W. Huang, B. Peng, and W. Wei, "A kinetic model for nanocrystal morphology evolution," *Chemphyschem*, vol. 8, no. 5, pp. 703–711, 2007.

[50] C. Murphy, T. San, A. Gole, C. Orendorff, J. Gao, L. Gou, S. Hunyadi, and T. Li, "Anisotropic metal nanoparticles: Synthesis, assembly, and optical applications," *J Phys Chem B*, vol. 109, no. 29, pp. 13857–13870, 2005.

[51] C. Johnson, E. Snoeck, M. Ezcurdia, B. Rodriguez-Gonzalez, I. Pastoriza-Santos, L. Liz-Marzan, and M. Hytch, "Effects of elastic anisotropy on strain distributions in decahedral gold nanoparticles," *Nat Mater*, vol. 7, no. 2, pp. 120–124, 2008.

[52] H. Chen, R. Liu, K. Asakura, L. Jang, and J. Lee, "Controlling length of gold nanowires with large-scale: X-ray absorption spectroscopy approaches to the growth process," *J Phys Chem C*, vol. 111, no. 50, pp. 18550–18557, 2007.

[53] F. Kim, S. Connor, H. Song, T. Kuykendall, and P. Yang, "Platonic gold nanocrystals," *Angew Chem Int Edit*, vol. 43, no. 28, pp. 3673–3677, 2004.

[54] B. Wiley, Y. Sun, B. Mayers, and Y. Xia, "Shape-controlled synthesis of metal nanostructures: The case of silver," *Chem-Eur J*, vol. 11, no. 2, pp. 454–463, 2005.

[55] M. Tornblom, U. Henriksson, and M. Ginley, "A field-dependent h-2 nuclear magnetic-relaxation study of the aggregation behavior in micellar solutions of ctab and sds," *J Phys Chem-Us*, vol. 98, no. 28, pp. 7041–7051, 1994.

[56] C. Bullen, P. Zijlstra, E. Bakker, M. Gu, and C. Raston, "Chemical kinetics of gold nanorod growth in aqueous ctab solutions," *Crystal Growth & Design*, vol. 11, no. 8, pp. 3375–3380, 2011.

[57] F. Hubert, F. Testard, A. Thill, Q. Kong, O. Tache, and O. Spalla, "Growth and overgrowth of concentrated gold nanorods: Time resolved saxs and xanes," *Crystal Growth & Design*, vol. 12, no. 3, pp. 1548–1555, 2012.

[58] J. A. Edgar, A. M. McDonagh, and M. B. Cortie, "Formation of gold nanorods by a stochastic „popcorn"mechanism," *ACS Nano*, vol. 6, no. 2, pp. 1116–1125, 2012.

[59] F. Hubert, F. Testard, and O. Spalla, "Cetyltrimethylammonium bromide silver bromide complex as the capping agent of gold nanorods," *Langmuir Langmuir*, vol. 24, no. 17, pp. 9219–9222, 2008.

[60] M. Liu and P. Guyot-Sionnest, "Mechanism of silver(i)-assisted growth of gold nanorods and bipyramids," *J Phys Chem B*, vol. 109, no. 47, pp. 22192–22200, 2005.

[61] M. Grzelczak, J. Perez-Juste, P. Mulvaney, and L. M. Liz-Marzan, "Shape control in gold nanoparticle synthesis," *Chem. Soc. Rev.*, vol. 37, pp. 1783–1791, 2008.

[62] X. S. Kou, S. Z. Zhang, C. K. Tsung, Z. Yang, M. H. Yeung, G. D. Stucky, L. D. Sun, J. F. Wang, and C. H. Yan, "One-step synthesis of large-aspect-ratio single-crystalline gold nanorods by using ctpab and ctbab surfactants," *Chemistry-a European Journal*, vol. 13, no. 10, pp. 2929–2936, 2007. 152VI Times Cited:41 Cited References Count:44.

[63] X. S. Kou, S. Z. Zhang, C. K. Tsung, M. H. Yeung, Q. H. Shi, G. D. Stucky, L. D. Sun, J. F. Wang, and C. H. Yan, "Growth of gold nanorods and bipyramids using cteab surfactant," *Journal of Physical Chemistry B*, vol. 110, no. 33, pp. 16377–16383, 2006. 074NB Times Cited:42 Cited References Count:56.

[64] N. Lewinski, V. Colvin, and R. Drezek, "Cytotoxicity of nanoparticles," *Small*, vol. 4, no. 1, pp. 26–49, 2008. 271GY Times Cited:592 Cited References Count:141.

[65] S. K. Murthy, "Nanoparticles in modern medicine: State of the art and future challenges," *International Journal of Nanomedicine*, vol. 2, no. 2, pp. 129–141, 2007. 247BH Times Cited:28 Cited References Count:76.

[66] Y. T. Lim, Y. W. Noh, J. H. Han, Q. Y. Cai, K. H. Yoon, and B. H. Chung, "Biocompatible polymer-nanoparticle-based bimodal imaging contrast agents for the labeling and tracking of dendritic cells," *Small*, vol. 4, no. 10, pp. 1640–1645, 2008. 362ML Times Cited:27 Cited References Count:49.

[67] J. Kreuter and S. Gelperina, "Use of nanoparticles for cerebral cancer," *Tumori*, vol. 94, no. 2, pp. 271–277, 2008. 305TA Times Cited:25 Cited References Count:43.

[68] M. H. Xu and L. H. V. Wang, "Photoacoustic imaging in biomedicine," *Review of Scientific Instruments*, vol. 77, no. 4, 2006. 037HA Times Cited:346 Cited References Count:126.

[69] C. H. Li and L. H. V. Wang, "Photoacoustic tomography and sensing in biomedicine," *Physics in Medicine and Biology*, vol. 54, no. 19, pp. R59–R97, 2009. 497IE Times Cited:61 Cited References Count:171.

[70] V. Saxena, M. Sadoqi, and J. Shao, "Indocyanine green-loaded biodegradable nanoparticles: preparation, physicochemical characterization and in vitro release," *International Journal of Pharmaceutics*, vol. 278, no. 2, pp. 293–301, 2004. 836DS Times Cited:56 Cited References Count:19.

[71] G. R. Souza, D. R. Christianson, F. I. Staquicini, M. G. Ozawa, E. Y. Snyder, R. L. Sidman, J. H. Miller, W. Arap, and R. Pasqualini, "Networks of gold nanoparticles and bacteriophage as biological sensors and cell-targeting agents," *Proceedings of the National Academy of Sciences of the United States of America*, vol. 103, no. 5, pp. 1215–1220, 2006. 009EO Times Cited:109 Cited References Count:43.

[72] F. Y. Cheng, S. P. H. Wang, C. H. Su, T. L. Tsai, P. C. Wu, D. B. Shieh, J. H. Chen, P. C. H. Hsieh, and C. S. Yeh, "Stabilizer-free poly(lactide-co-glycolide) nanoparticles for multimodal biomedical probes," *Biomaterials*, vol. 29, no. 13, pp. 2104–2112, 2008. 315BO Times Cited:30 Cited References Count:30.

[73] W. Bost and R. Lemor, "Photoacoustic microscopy of high resolution imaging," *The Journal of the Acoustical Society of America*, vol. 123, no. 5, p. 3370, 2008.

[74] W. Bost, F. Stracke, E. C. Weiss, S. Narasimhan, M. C. Kolios, and R. Lemor, "High frequency optoacoustic microscopy," *Conf Proc IEEE Eng Med Biol Soc*, vol. 2009, pp. 5883–6, 2009. Bost, Wolfgang Stracke, Frank Weiss, Eike C Narasimhan, Sankar Kolios, Michael C Lemor, Robert IOP-80026/Canadian Institutes of Health Research/Canada Conf Proc IEEE Eng Med Biol Soc. 2009;2009:5883-6.

[75] E. C. Weiss, P. Anastasiadis, G. Pilarczyk, R. M. Lemor, and P. V. Zinin, "Mechanical properties of single cells by high-frequency time-resolved acoustic microscopy," *Ieee Transactions on Ultrasonics Ferroelectrics and Frequency Control*, vol. 54, no. 11, pp. 2257–2271, 2007. 229FV Times Cited:13 Cited References Count:53.

[76] R. G. Rayavarapu, C. Ungureanu, P. Krystek, T. G. van Leeuwen, and S. Manohar, "Iodide impurities in hexadecyltrimethyl ammonium bromide (ctab) products: Lot-lot variations and influence on gold nanorod synthesis," *Langmuir*, vol. 26, no. 7, pp. 5050–5055, 2010. 574MY Times Cited:11 Cited References Count:25.

[77] D. K. Smith and B. A. Korgel, "The importance of the ctab surfactant on the colloidal seed-mediated synthesis of gold nanorods," *Langmuir*, vol. 24, no. 3, pp. 644–649, 2008. PMID: 18184021.

[78] D. K. Smith, N. R. Miller, and B. A. Korgel, "Iodide in CTAB Prevents Gold Nanorod Formation," *LANGMUIR*, vol. 25, pp. 9518–9524, AUG 18 2009.

[79] O. L. Muskens, P. Billaud, M. Broyer, N. Fatti, and F. Vallee, "Optical extinction spectrum of a single metal nanoparticle: Quantitative characterization of a particle and of its local environment," *Physical Review B*, vol. 78, no. 20, 2008. 376XD Times Cited:23 Cited References Count:45.

[80]

[81] T.-Y. Tseng, P.-J. Lai, and K.-B. Sung, "High-throughput detection of immobilized plasmonic nanoparticles by a hyperspectral imaging system based on fourier transform spectrometry," *Opt. Express*, vol. 19, pp. 1291–1300, Jan 2011.

[82] M. Robbins and B. Hadwen, "The noise performance of electron multiplying charge-coupled devices," *IEEE TRANSACTIONS ON ELECTRON DEVICES*, vol. 50, pp. 1227–1232, MAY 2003.

[83] S. Barbosa, A. Agrawal, L. Rodriguez-Lorenzo, I. Pastoriza-Santos, R. A. Alvarez-Puebla, A. Kornowski, H. Weller, and L. M.

Liz-Marzan, "Tuning size and sensing properties in colloidal gold nanostars," *Langmuir*, vol. 26, no. 18, pp. 14943–14950, 2010. 648JV Times Cited:32 Cited References Count:46.

[84] L. J. Sherry, R. C. Jin, C. A. Mirkin, G. C. Schatz, and R. P. Van Duyne, "Localized surface plasmon resonance spectroscopy of single silver triangular nanoprisms," *Nano Letters*, vol. 6, no. 9, pp. 2060–2065, 2006. 083NT Times Cited:256 Cited References Count:49.

[85] Y. Khalavka, J. Becker, and C. Sönnichsen, "Synthesis of rod-shaped gold nanorattles with improved plasmon sensitivity and catalytic activity," *Journal of the American Chemical Society*, vol. 131, no. 5, pp. 1871–1875, 2009.

[86] I. Ament, J. Prasad, A. Henkel, S. Schmachtel, and C. Sönnichsen, "Single unlabeled protein detection on individual plasmonic nanoparticles," *Nano Letters*, vol. 12, no. 2, pp. 1092–1095, 2012. 887XW Times Cited:3 Cited References Count:34.

[87] P. Zijlstra, P. M. R. Paulo, and M. Orrit, "Optical detection of single non-absorbing molecules using the surface plasmon resonance of a gold nanorod," *Nature Nanotechnology*, vol. 7, no. 6, pp. 379–382, 2012. 955HO Times Cited:1 Cited References Count:32.

[88] N. Del Fatti, D. Christofilos, and F. Vallee, "Optical response of a single gold nanoparticle," *Gold Bull*, vol. 41, no. 2, pp. 147–158, 2008.

[89] A. Lombardi, M. Loumaigne, A. Crut, P. Maioli, N. Del Fatti, F. Vallee, M. Spuch-Calvar, J. Burgin, J. Majimel, and M. Treguer-Delapierre, "Surface plasmon resonance properties of single elongated nano-objects: Gold nanobipyramids and nanorods," *Langmuir*, vol. 28, no. 24, pp. 9027–33, 2012.

[90] P. J. Schuck, D. P. Fromm, A. Sundaramurthy, G. S. Kino, and W. E. Moerner, "Improving the mismatch between light and nanoscale objects with gold bowtie nanoantennas," *Phys. Rev. Lett.*, vol. 94, p. 017402, Jan 2005.

[91]

[92] E. Altewischer, M. P. van Exter, and J. P. Woerdman, "Plasmon-assisted transmission of entangled photons," *Nature*, vol. 418, no. 6895, pp. 304–306, 2002. 10.1038/nature00869.

[93] C. Hagglund, M. Zach, G. Petersson, and B. Kasemo, "Electromagnetic coupling of light into a silicon solar cell by nanodisk plasmons," *Appl Phys Lett*, vol. 92, FEB 4 2008.

[94] K. Henzler-Wildman, "Dynamic personalities of proteins," *Nature*, vol. 450, pp. 964–972, 2007.

[95] S. Weiss, "Fluorescence spectroscopy of single biomolecules," *Science*, vol. 283, no. 5408, pp. 1676–1683, 1999.

[96] A. Yanik, A. Cetin, M. Huang, A. Artar, S. Mousavi, A. Khanikaev, J. Connor, G. Shvets, and H. Altug, "Seeing protein monolayers with naked eye through plasmonic fano resonances," *Proceedings of the National Academy of Sciences of the United States of America*, vol. 108, no. 29, pp. 11784–11789, 2011.

[97] A. Armani, R. Kulkarni, S. Fraser, R. Flagan, and K. Vahala, "Label-free, single-molecule detection with optical microcavities," *Science*, vol. 317, no. 5839, pp. 783–787, 2007.

[98] L. He, S. Oezdemir, J. Zhu, W. Kim, and L. Yang, "Detecting single viruses and nanoparticles using whispering gallery microlasers," *Nature Nanotechnology*, vol. 6, no. 7, pp. 428–432, 2011.

[99] S. Nie and S. Emery, "Probing single molecules and single nanoparticles by surface-enhanced raman scattering," *Science*, vol. 275, no. 5303, pp. 1102–1106, 1997.

[100] S. Sorgenfrei, C. Chiu, R. Gonzalez, Y. Yu, P. Kim, C. Nuckolls, and K. Shepard, "Label-free single-molecule detection of dna-hybridization kinetics with a carbon nanotube field-effect transistor," *Nature Nanotechnology*, vol. 6, no. 2, pp. 125–131, 2011.

[101] Y. Cui, Q. Wei, H. Park, and C. Lieber, "Nanowire nanosensors for highly sensitive and selective detection of biological and chemical species," *Science*, vol. 293, no. 5533, pp. 1289–1292, 2001.

[102] J. Anker, W. Hall, O. Lyandres, N. Shah, J. Zhao, and R. Van Duyne, "Biosensing with plasmonic nanosensors," *Nat Mater*, vol. 7, no. 6, pp. 442–453, 2008.

[103] E. Larsson, C. Langhammer, I. Zoric, and B. Kasemo, "Nanoplasmonic probes of catalytic reactions," *Science*, vol. 326, no. 5956, pp. 1091–1094, 2009.

[104] A. McFarland and R. Van Duyne, "Single silver nanoparticles as real-time optical sensors with zeptomole sensitivity," *Nano Letters*, vol. 3, no. 8, pp. 1057–1062, 2003.

[105] K. Vahala, "Optical microcavities," *Nature*, vol. 424, no. 6950, pp. 839–846, 2003.

[106] P. Jain, X. Huang, I. El-Sayed, and M. El-Sayed, "Noble metals on the nanoscale: Optical and photothermal properties and some applications in imaging, sensing, biology, and medicine," *Accounts of Chemical Research*, vol. 41, no. 12, pp. 1578–1586, 2008.

[107] E. Betzig, G. Patterson, R. Sougrat, O. Lindwasser, S. Olenych, J. Bonifacino, M. Davidson, J. Lippincott-Schwartz, and H. Hess, "Imaging intracellular fluorescent proteins at nanometer resolution," *Science*, vol. 313, no. 5793, pp. 1642–1645, 2006.

[108] M. Rust, M. Bates, and X. Zhuang, "Sub-diffraction-limit imaging by stochastic optical reconstruction microscopy (storm)," *Nature Methods*, vol. 3, no. 10, pp. 793–795, 2006.

[109] K. Mayer, F. Hao, S. Lee, P. Nordlander, and J. Hafner, "A single molecule immunoassay by localized surface plasmon resonance," *Nanotechnology*, vol. 21, no. 25, p. 255503, 2010.

[110] P. Mulvaney, J. Perez-Juste, M. Giersig, L. Liz-Marzan, and C. Pecharroman, "Drastic surface plasmon mode shifts in gold nanorods due to electron charging," *Plasmonics*, vol. 1, no. 1, pp. 61–66, 2006.

[111] G. Anand, S. Sharma, A. Dutta, S. Kumar, and G. Belfort, "Conformational transitions of adsorbed proteins on surfaces of varying polarity," *Langmuir*, vol. 26, no. 13, pp. 10803–10811, 2010.

[112] E. Lüthgens and A. Janshoff, "Equilibrium coverage fluctuations: A new approach to quantify reversible adsorption of proteins," *Chemphyschem*, vol. 6, no. 3, pp. 444–448, 2005.

[113] R. Kubo, "Fluctuation-dissipation theorem," *Reports on Progress in Physics*, vol. 29, pp. 255–&, 1966.

[114] C. Jarzynski, "Nonequilibrium equality for free energy differences," *Physical Review Letters*, vol. 78, no. 14, pp. 2690–2693, 1997.

[115] U. Hohenester and J. Krenn, "Surface plasmon resonances of single and coupled metallic nanoparticles: A boundary integral method approach," *Physical Review B*, vol. 72, no. 19, p. 195429, 2005.

[116] A. Kabashin, P. Evans, S. Pastkovsky, W. Hendren, G. Wurtz, R. Atkinson, R. Pollard, V. Podolskiy, and A. Zayats, "Plasmonic nanorod metamaterials for biosensing," *Nature Materials*, vol. 8, no. 11, pp. 867–871, 2009.

[117] N. Liu, H. Guo, L. Fu, S. Kaiser, H. Schweizer, and H. Giessen, "Three-dimensional photonic metamaterials at optical frequencies," *Nature Materials*, vol. 7, no. 1, pp. 31–37, 2008.

[118] N. Liu, H. Liu, S. Zhu, and H. Giessen, "Stereometamaterials," *Nature Photonics*, vol. 3, no. 3, pp. 157–162, 2009.

[119] S. Acimovic, M. Kreuzer, M. Gonzalez, and R. Quidant, "Plasmon near-field coupling in metal dimers as a step toward single-molecule sensing," *Acs Nano*, vol. 3, no. 5, pp. 1231–1237, 2009.

[120] N. Liu, M. Hentschel, T. Weiss, A. Alivisatos, and H. Giessen, "Three-dimensional plasmon rulers 10.1126/science.1199958," *Science*, vol. 332, no. 6036, pp. 1407–1410, 2011.

[121] N. Liu, M. Tang, M. Hentschel, H. Giessen, and A. Alivisatos, "Nanoantenna-enhanced gas sensing in a single tailored nanofocus," *Nat Mater*, vol. 10, no. 8TY - JOUR 10.1038/nmat3029, pp. 631–636, 2011.

Eine wirklich gute Idee erkennt man daran,
dass ihre Verwirklichung von vorne herein ausgeschlossen erscheint.
— Albert Einstein

ACKNOWLEDGMENTS

I want to thank all those who helped me completing my dissertation.
[Aus datenschutzrechtlichen Gründen entfernt]

Finally, I want to thank all the rest of the nanobiotechnology group for their support.

SCIENTIFIC PUBLICATIONS

[1] "*Microfluidic continuous flow synthesis of rod-shaped gold and silver nanocrystals*"
Boleiniger, J.; **Kurz, A.**; Reuss, V.; Sönnichsen, C.
Physical Chemistry Chemical Physics 2006, 8, 3824
doi:10.1039/B604666E

[2] "*En-Face differential absorption optical coherence tomography with gold nanorods as the contrast agent*"
Leitner, M.; **Henkel, A.**; Sönnichsen, C.; Rosa, C.C.; Podoleanu, A.G.
Proc. SPIE 7139
doi:10.1117/12.814624

[3] "*Tuning Plasmonic Properties by Alloying Copper into Gold Nanorods*"
Henkel, A.; Jakab, A.; Brunklaus, G.; Sönnichsen, C.
J.Phys.Chem.C 2009, 113, 6, 2200
doi:10.1021/jp810433e

[4] "*Growth Kinetic of a Rod-Shaped Metal Nanocrystal*"
Henkel, A.; Schubert, O.; Plech, A.; Sönnichsen, C.
J.Phys.Chem.C 2009, 113, 24, 10390
doi:10.1021/jp810979r

[5] "*Evaluation of Nanoparticles as Contrast Agent for Photoacoustic Imaging in Living Cells*"
Kohl, Y.; Thielecke, H.; Bost, W.; Lemor, R.; Stracke, F.; Kaiser, C.; Schroeter, M.; Kratz, K.; **Henkel, A.**; Sönnichsen, C.
Nanostructured Materials and Nanotechnology IV 2010
doi:10.1002/9780470944042.ch1

[6] "*Single Unlabeled Protein Detection on Individual Plasmonic Nanoparticles*"
Ament, I.; Prasad, J.; **Henkel, A.**; Schmachtel, S.; Sönnichsen, C.
Nano Letters 2012, 12, 2, 1092
doi:10.1021/nl204496g

[7] "*A New Approach to Assess Gold Nanoparticle Uptake by Mammalian Cells: Combining Optical Dark-Field and Transmission Electron Microscopy*"
Rosman, C.; Pierrat, S.; **Henkel, A.**; Tarantola, M.; Schneider, D.; Sunnick, E. ; Janshoff, A.; Sönnichsen, C.
Small 2012
doi:10.1002/smll.201200853

[8] "*Multiplexed plasmon sensor for rapid label-free analyte detection*"
Rosman, C.; Prasad, J.; Neiser, A.; **Henkel, A.**; Sönnichsen, C.
Nano Lett., 13(7), 3243
doi:10.1021/nl401354f

[9] "*Size Variation Accounts for One Third of Interparticle Variation in Plasmonic Sensitivity of Gold Nanorods*"
Henkel, A.; Khalavka, Y.; Neiser, A.; Rosman, C.; Schmachtel, S.; Sön-

nichsen, C.
In preparation — manuscript finished

University and Highschool Education

1/2013–	Postdoc in the nanobiotechnology group of Prof. Sönnichsen at the Institute of Physical Chemistry, Johannes Gutenberg University Mainz
02/2008–12/2012	Doctoral studies in the nanobiotechnology group of Prof. Sönnichsen at the Institute of Physical Chemistry, Johannes Gutenberg University Mainz
10/2002–01/2008	Diploma in chemistry (2.1), Johannes Gutenberg University Mainz, thesis entitled „Synthesis and characterization of gold-copper-nanorods. “
10/2000–08/2004	Diploma in piano pedagogy (1.5), Johannes Gutenberg University Mainz, thesis entitled „Robert Schumanns Davidsbündlertänze und seine literarischen Vorbilder. “
07/1999	„Abitur “(2.3), Oraniengymnasium Wiesbaden, major courses chemistry and german

National Service

09/1999–07/2000	German mandatory national service (11 months) working for the hospital Frankfurt am Main Höchst